.64-13

WADD-TR-60-646
PART III, VOLUME II

CARBONIZATION OF PLASTICS AND REFRACTORY MATERIAL RESEARCH

VOLUME II. REFRACTORY MATERIALS

TECHNICAL REPORT No. WADD-TR-60-646, PART III, VOLUME II

MARCH 1964

AF MATERIALS LABORATORY
RESEARCH AND TECHNOLOGY DIVISION
AIR FORCE SYSTEMS COMMAND
WRIGHT-PATTERSON AIR FORCE BASE, OHIO

Project No. 4776, ARPA Order No. 24-61, Task 6

(Prepared under Contract No. AF 33(616)-6841 by the
General Electric Company, Evendale, Ohio;
G. M. Kibler, T. F. Lyon, M. J. Linevsky,
V. J. DeSantis, authors)

NOTICES

Qualified requesters may obtain copies of this report from the Defense Documentation Center (DDC), (formerly ASTIA), Cameron Station, Bldg. 5, 5010 Duke Street, Alexandria 4, Virginia

This report has been released to the Office of Technical Services, U.S. Department of Commerce, Washington 25, D.C., in stock quantities for sale to the general public.

Copies of this report should not be returned to the Aeronautical Systems Division unless return is required by security considerations, contractual obligations, or notice on a specific document.

600 - April 1964 - 162-36-714

FOREWORD

This report, prepared by the Flight Propulsion Laboratory Department, General Electric Company, summarizes the results of investigations performed under the auspices of the Department of Defense, through the Advanced Research Projects Agency, Order No. 24-61, Task 6, Project No. 4776, "Materials Thermal Properties," and in accordance with contract No. AF33(616)-6841. The contract was administered by the Directorate of Materials and Processes, Deputy for Technology, Aeronautical Systems Division, Mr. P.W. Dimiduk, and Lt. W.C. Jones, project engineers.

The work reported herein was performed during the period 1 July 1961 to 30 June 1962, inclusive. Reference is generally made to WADD Technical Report 60-646, Parts I and II in which work accomplished earlier was reported. This report is published in two volumes; Volume 1 reports the results of studies concerned with the "Carbonization of Plastics." Volume 2 concerns the "Refractory Materials Research" portion of the contractual effort.

The overall program during the period was under the direction of Dr. G. M. Kibler, Flight Propulsion Laboratory Department. The individual tasks were conducted as follows:

1. Carbonization of Plastics - Directed by J. A. Coffman; work by W. S. Horton, E. E. Stone, G. P. Brown, E. G. McGowan, G. P. Schacher, A. Goldman, and H. Friedman.

2. Vapor Pressure of Refractory Materials - Directed by Dr. G. M. Kibler; investigations performed by Drs. T. F. Lyon and M. J. Linevsky.

3. Spectral Emissivity of Refractory Materials - Directed and performed by Mr. V. J. DeSantis under consultation by Drs. Earl Feinbold and P. Gorsuch.

ABSTRACT

Results of continued investigations of the vapor pressures of pressures of selected refractory materials and the spectral emissivities of similar classes of compounds are presented in this report: Volume 2 of WADD Technical Report 60-646, Part III.

Vapor pressure studies have been conducted through the application of Langmuir evaporation, Knudsen effusion, matrix isolation and resonance line absorption techniques. The vaporization of hafnium and zirconium nitrides was studied by the Knudsen effusion method; the Langmuir evaporation method was applied to pure hafnium metal. Matrix isolation of vapor over thoria proved successful and structural assignments have been made to various bands in the infrared absorption spectra of the matrix isolated species. Resonance line absorption photometry studies of TiB_2 have been completed.

Normal spectral emissivity data from 0.4 to 5.0 microns and from 1500 to 2500°K, supported by systematic methods of material characterization, have been obtained (through studies reported here) for the compounds niobium diboride, zirconium diboride, titanium diboride, tantalum nitride, hafnium nitride, and zirconium nitride.

This technical report has been reviewed and is approved.

Jules I. Wittebort

JULES I. WITTEBORT
Chief, Thermal and Solid State Branch
Materials Physics Division
Air Force Materials Laboratory

TABLE OF CONTENTS

Page

LIST OF ILLUSTRATIONS

LIST OF ILLUSTRATIONS (CONT'D.)

LIST OF ILLUSTRATIONS (CONT'D.)

LIST OF ILLUSTRATIONS (CONT'D.)

LIST OF ILLUSTRATIONS (CONT'D.)

LIST OF TABLES

I. INTRODUCTION

Investigations proposed to provide physical, chemical and thermodynamic property data for selected refractories of possible application to uncooled rocket nozzles were undertaken in November, 1959. Through the provision of the data sought, it was anticipated that design information and selection criteria would become available. In addition, results obtained would add to the understanding of the processes occurring under the conditions and environments in which nozzle materials must exist. Since the inception of this program, research studies have continued in three distinct areas: 1) the process of plastics degradation, including rates and nature and identity of products, has been studied; 2) vapor pressures, rates of vaporization, identity of vapor species, and accessible thermodynamic functions obtainable from such measurements have been investigated at very high temperatures by diverse methods appropriate to the materials selected for study; and 3) normal spectral emissivity measurements, again at very high temperatures, have been made on selected refractories to provide radiative heat transfer information under the conditions investigated.

Details of the effort and the results obtained during the period July 1961 through June 1962 are presented and discussed in the body of this report. Vaporization and emissivity results are discussed in separate sections. No effort has been made to summarize the results obtained earlier and reported in Parts I and II of WADD Technical Report 60-646; however, in certain instances, illustrations describing apparatus have been repeated herein for clarity.

Manuscript released by authors August, 1962 for publication as a WADD Technical Report.

II. VAPOR PRESSURE OF REFRACTORY MATERIALS

A. Background

In November 1959, a study of vapor pressures of a number of refractory materials was undertaken with the objective of determining evaporation (decomposition) rates of these refractories in order to predict their ability to withstand rocket nozzle conditions. Of perhaps even greater importance was the objective of obtaining high temperature thermodynamic property data useful in predicting mechanisms and energetics of high temperature processes entered into by the materials studied.

By the end of June 1961, Langmuir evaporation studies had been completed on TaC, ZrC, HfC, TiC, and WC. Some data had also been obtained on ThO_2 by this method, though the Langmuir method was clearly inappropriate to this material. From chemical and X-ray analyses of the original specimens, the residual materials, and the condensed sublimates, the phenomenological mechanisms of the processes occurring had been determined. Resonance line absorption photometry applied to ZrC and TiC had determined that these materials evaporated entirely as individual atom species and the free energies and heats of formation of these two materials had been obtained from these measurements. These values were in excellent agreement with similar thermodynamic property values computed from the Langmuir evaporation data. At that time (1961), although the equipment had become operable for matrix isolation studies of the vapor species from ThO_2, severe experimental difficulties had prevented success in this study.

In the past year, work has continued along similar lines in further vapor pressure studies. The Knudsen effusion method, rather than Langmuir evaporation, was applied to the study of vapor pressures of refractory nitrides, specifically ZrN and HfN. Resonance line absorption photometry was applied to the study of borides with TiB_2, the material of initial interest. Success was finally attained in the matrix isolation of vapors from ThO_2 and structural assignments have been made for the infrared bands in the absorption spectra of these vapors.

Details of the effort follow.

B. Refractory Nitride Vaporization

1. Experimental

a. Apparatus

The apparatus diagrammed in Figure 1 measures the rate of effusion of permanent gases from an inductively heated Knudsen cell. The vacuum system is made of Pyrex except for the furnace chamber which is fused quartz joined to a Vycor standard taper joint. The effusion cell is heated inductively by a three-turn coil 2-1/4 inches inside diameter. The cooling water jacket slips into a Lucite overflow cup and is sealed by means of an O-ring. This design allows the work coil to fit closely around the cooling jacket, yet permits the furnace chamber to be removed without disconnecting the coil.

Temperatures are measured with a micro-optical pyrometer by sighting on the effusion orifice through the window and prism. A magnetically operated shutter protects the window from fogging due to condensible vapors from the effusion cell. The pyrometer is periodically calibrated against a tungsten ribbon filament lamp supplied by the Pyrometer Instrument Co., Inc. This lamp had been calibrated against an NBS certified pyrometer. Appropriate corrections were made for the transmission of the window and prism.

It should be clear from Figure 1 that the permanent gases effusing from the cell pass through the liquid nitrogen trap and the main diffusion pump and, with stopcock "C" closed and "B" open, are eliminated from the system by the fore diffusion pump. With stopcocks "B" and "D" closed and "C" open, any gases passing through the main diffusion pump are forced into the McLeod gauge system by the automatic Toepler pump. The Toepler pump (Delmar Scientific #DS-7030-50) has a 500 cc piston stroke and operates on a 35 second cycle. Inlet and outlet seals are provided by mercury float valves.

Since the gas collected occupies the McLeod volume plus the volume of the connecting lines between stopcock "D" and the outlet valve on the Toepler pump, the system was calibrated after assembly so that the true mass of gas collected could be related to the gauge reading. This calibration was accomplished by admitting pure nitrogen into the gauge plus connecting lines, trapping a portion in the gauge and then evacuating the connecting lines. The true mass of gas trapped in the gauge could be computed since the McLeod volumes are known. This gas was then shared with the connecting lines and a second McLeod reading taken. A series of such measurements gave the required calibration curve.

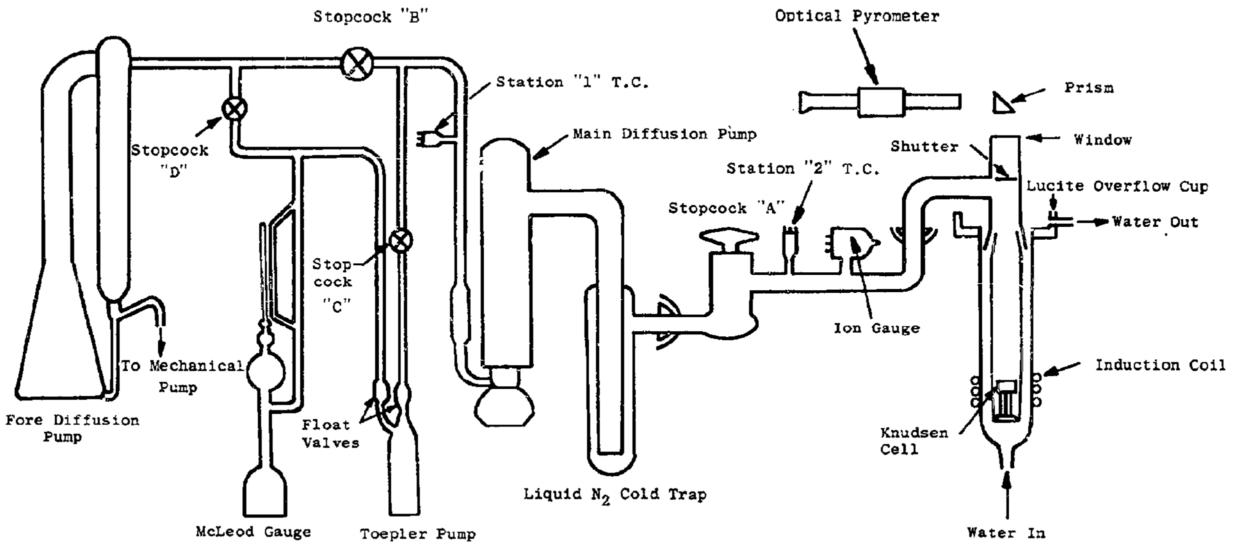

Figure 1. Knudsen Effusion Apparatus - Measurement of Permanent Gas Evolution

The following procedure has been adopted for making the effusion rate measurements. The McLeod gauge and Toepler pump are thorouthly evacuated and isolated by closing stopcocks "C" and "D". The effusion cell is then brought to the desired temperature and some time allowed for steady conditions to be reached, this condition being denoted by the constant or slowly decreasing reading on the ionization gauge and the constant cell temperature. During this time, the effusing gas is expelled through stopcock "B". When steady conditions have been reached, stopcock "B" is closed and the increasing reading of the thermocouple gauge at Station 1 is observed. When this reading reaches a value higher than that which is obtained when the Toepler pump is connected, a timer is started and the thermocouple gauge reading is carefully noted. Stopcock "C" is then opened and the effusing gas is pumped into the McLeod volume. During the time the gas is being collected, several readings of the cell temperature are made. After a convenient length of time, stopcock "C" is closed and the thermocouple gauge reading at Station 1 again is observed as it increases. When it reaches exactly the same value as at the "start" time, the timer is stopped. A few cycles of the Toepler pump clears it of residual gas and a reading of the McLeod gauge gives the mass of gas collected in the time interval.

This procedure gives sharp start and stop times and thus the time interval may be measured very accurately. In addition, the system is in exactly the same conditions at the beginning and end of each run with the only disturbance being the opening and closing of stopcock "C".

Several other features should be noted. First, the system is quite sensitive. Apparently reliable effusion measurements have been made at rates less than three micrograms per hour. At lower rates, the start and stop times are no longer sharp and so the total effusion time must be long to maintain the required accuracy in the time measurement. A more sensitive system could probably be had by eliminating the Toepler pump and connecting the McLeod gauge directly at Station 1 for measurements at the lowest effusion rates. At higher rates, however, this simplified system might not be practical since the fore-pressure on the main diffusion pump would increase rapidly during the course of the measurement and affect the pumping speed. The upper limit on the effusion rate is determined chiefly by the necessity to maintain Knudsen flow conditions in the cell in order that meaningful cell pressures may be computed. With the present system, effusion rates as high as 4500 micrograms per hour have been measured.

Another advantage of this system is that numerous measurements may be taken at various temperatures with no need to break the vacuum until the cell contents are depleted. Furthermore, the effusion rate of only permanent gas is measured. This would be an advantage over a system in which, for example, only the total weight loss of the cell is obtained.

An obvious disadvantage is that the system must be thoroughly outgassed and free of leakage so that the gas collected arises only from effusion from the Knudsen cell.

The effusion cells, constructed of tungsten, and the supporting assembly are shown in Figure 2. The cells were made in two pieces which fit snugly together and, except for the cell with largest orifice area, were sealed at the joint by electron beam welding. Outside diameter and height were 3/4" while corresponding cavity dimensions were 3/8". The 45° taper on the cell lid forms essentially a knife edge orifice. The orifice so constructed was assumed to be ideal.

Each empty cell was heated under high vacuum at temperatures in excess of 2200°C for five hours in order to outgas the piece thoroughly before effusion measurements were made. The cell was then loaded with ZrN through the orifice and mounted in the vacuum system. After overnight pumping, accessible tubing in the system was flamed to remove adsorbed gases. The cell was then heated slowly to about 1000°C over a period of eight hours to eliminate adsorbed gas in the powder. This point was taken to be the initial time for calculation of total nitrogen loss (cf. equation 2 and later discussion).

b. Preparation and Chemical Analysis of Zirconium Nitride

Samples of commercial zirconium nitride were obtained from several different suppliers. All material so obtained was found to be deficient in nitrogen and to contain excessive amounts of oxygen. Efforts were then made to prepare the pure materials here.

Reactor grade zirconium hydride (Metal Hydrides, Inc.) was heated under either high purity nitrogen or ammonia. A typical analysis of the hydride is given in Table 1. For temperatures up to 1000°C, the hydride was contained in a zirconium boat in a resistively heated tube furnace. For higher temperatures, the material was contained in an inductively heated molybdenum crucible. Commercial high purity nitrogen was further purified by bubbling the gas through three solutions and then through a liquid nitrogen cooled cold trap. The three bubblers contained in order, sodium anthraquinone sulfonate and sodium dithionite in alkaline solution, saturated lead acetate and sulfuric acid solution.. Spectrochemical analysis after nitridation showed that no molybdenum pick-up occurred when a molybdenum crucible was used.

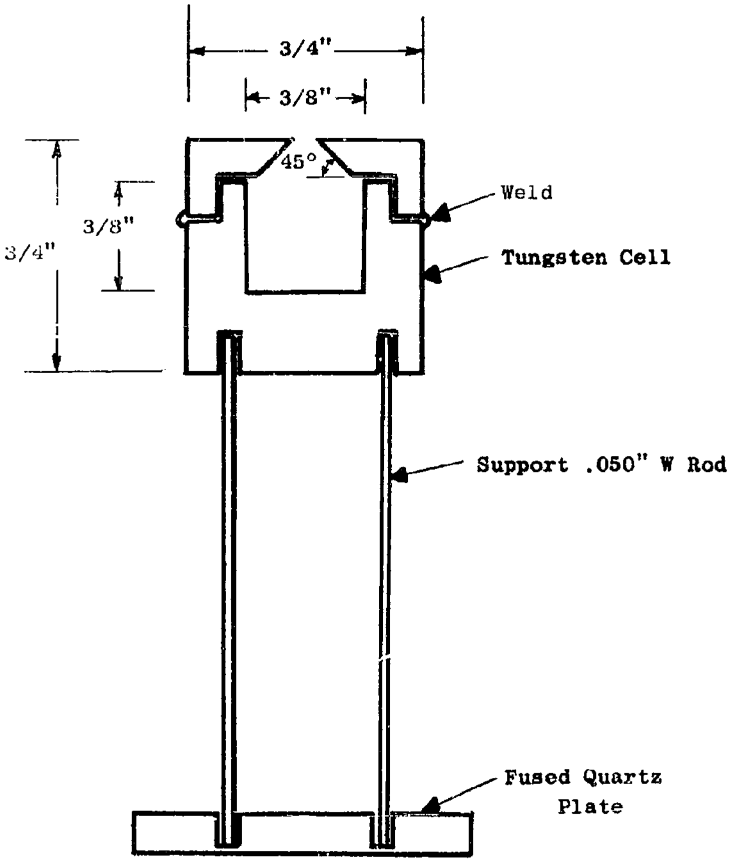

Figure 2. Tungsten Effusion Cell and Supports

Table 1

TYPICAL ANALYSIS OF REACTOR GRADE ZIRCONIUM HYDRIDE

(METAL HYDRIDES, INC.)

Component	wt%	Component	wt%
Zr	97.8	Mg	.01
Hf	.005	Fe	.06
H	1.95	Cr	.0075
O	.12	Ni	.002
N	.01	Mn	.0025
C	<.01	Ti	.0015
Cl(Water Soluble)	<.003	Al	.002
B	<.00005	Ca	.001
Li	.003		
Other metals each	.001		
Particle size:	-325 mesh		

Two batches of nitride were prepared containing 13.01 wt% nitrogen compared to the stoichiometric value, 13.31. The first batch was prepared from the hydride by heating 45 hours at 1000°C and five hours at 1350°C. The second batch was prepared in five hours at 1500°C. Purified nitrogen at atmospheric pressure was used as the nitriding agent in both cases.

Several other nitrides were prepared having lower nitrogen content. Conclusions to be drawn from these nitriding experiments are that ammonia is not particularly more effective than nitrogen for obtaining nitride of high nitrogen content and that temperatures near 1500°C are necessary to reach a nitrogen content of 13 wt% N in a reasonable period of time. These conclusions of course apply only to the -325 mesh zirconium hydride used here. It is expected that coarser material would be more difficult to nitride.

Initially, analyses of ZrN for nitrogen were made by the Dumas method essentially as described in Ref. 1.[*] This method was found to be quite tedious and time consuming and to have some tendency toward low values for nitrogen, presumably due to incomplete oxidation of the samples. The Kjeldahl method, described in Ref. 2, was found to be more rapid and to give more reproducible results. All nitrogen analyses given in this report are those obtained by the latter method.

---

[*] Page 65

c. Preparation and Chemical Analysis of Hafnium Nitride

After the difficulties encountered in obtaining commercially pure zirconium nitride, it was decided to prepare hafnium nitride from the hydride. Two samples of commercial hafnium hydride were obtained. The first contained about 4% Zr, about 1% O and Nb and numerous minor metallic impurities. The second commercial sample contained about 4% Zr, .15% O and a number of trace metallic impurities. Both of these samples were considered to be too contaminated for further study.

Finally, a sample of hafnium hydride which had been prepared from USAEC reactor grade hafnium crystal bar was obtained. This material was heated under purified nitrogen for 6-1/2 hours at 1500°C. Chemical analysis of the resulting nitride is shown in Table 2. This nitride is quite pure except for the 1.05% Zr.

Table 2

ANALYSIS OF HAFNIUM NITRIDE

Component	wt%	Method
O	.031	Vacuum fusion
H	.0024	Vacuum fusion
N	7.37	Kjeldahl
Zr	1.05	(Analysis performed by Ledoux & Co., Inc.)
Fe	trace	Spectrographic
Mg	trace	Spectrographic
Ti	trace	Spectrographic
Hf	(91.55)	Balance

It should be noted that if one defines "stoichiometric" in this case as meaning one metal (Hf or Zr) atom for each N atom, then for the nitride of Hf containing 1.05 wt% Zr, one calculates 7.35 to be the "stoichiometric" nitrogen weight percent. The material prepared here is, then, "stoichiometric" within the accuracy of the nitrogen analysis. Pure HfN has a stoichiometric composition of 7.27 wt% N.

d. Determination of Nitride Composition

Zirconium nitride and hafnium nitride are phases of variable composition; that is, the nitride phase may exist at nitrogen contents considerably less than stoichiometric. Since the equilibrium pressure of nitrogen over the nitride is much higher than that of the metal, as vaporization proceeds, the composition of the solid shifts to lower nitrogen content with a corresponding decrease in nitrogen pressure. It is,therefore, important that, in addition to the effusion rate and temperature, an accurate determination of the composition be made for each measurement.

It has been found that the nitrogen effusion rate as measured with the gas collection system is a linear function of the pressure indicated on the ionization gauge (Fig. 1) over a rather wide range of pressures. A typical plot of effusion rate vs. ionization gauge pressure is shown in Fig. 3 for a particular series of measurements. Actually, similar plots were made for each series of measurements and for each pressure gauge range over which measurements were taken. Effusion rates between 1 and 15 μ gm per hour gave indicated ionization gauge pressures on the 10^{-7} torr scale; between 20 and 150 μ gm per hour, on the 10^{-6} torr scale; between 150 and 1400, on the 10^{-5} torr scale and above 1400, on the 10^{-4} torr scale.

Such a relationship affords a convenient method of determining the composition of the evaporating material once the initial composition has been determined. The rate of evaporation of nitrogen may be expressed as:

$$\frac{dw}{dt} = a_1 + a_2 p_2 \tag{1}$$

where w is the total mass of nitrogen in the sample, t the time, p_2 the ionization gauge pressure and a_1 and a_2 are constants determined from the slope and intercept of plots such as Fig. 3. From integration of eq. 1 there is obtained

$$\Delta w = a_1 \Delta t + a_2 \int_{t_1}^{t_2} p_2 dt \tag{2}$$

where Δw is the loss of nitrogen from the cell contents in a time interval $\Delta t = t_2 - t_1$. The ionization gauge pressure was continuously indicated on a strip chart recorder from which chart the integral in eq. 2 was determined by measuring the area under the curve with a polar planimeter and applying appropriate scale factors. The initial total mass of nitrogen in the sample w^o is determined from the initial total mass of the sample W^o, and the chemical analysis. The nitrogen weight fraction in the sample at any time can then be determined from

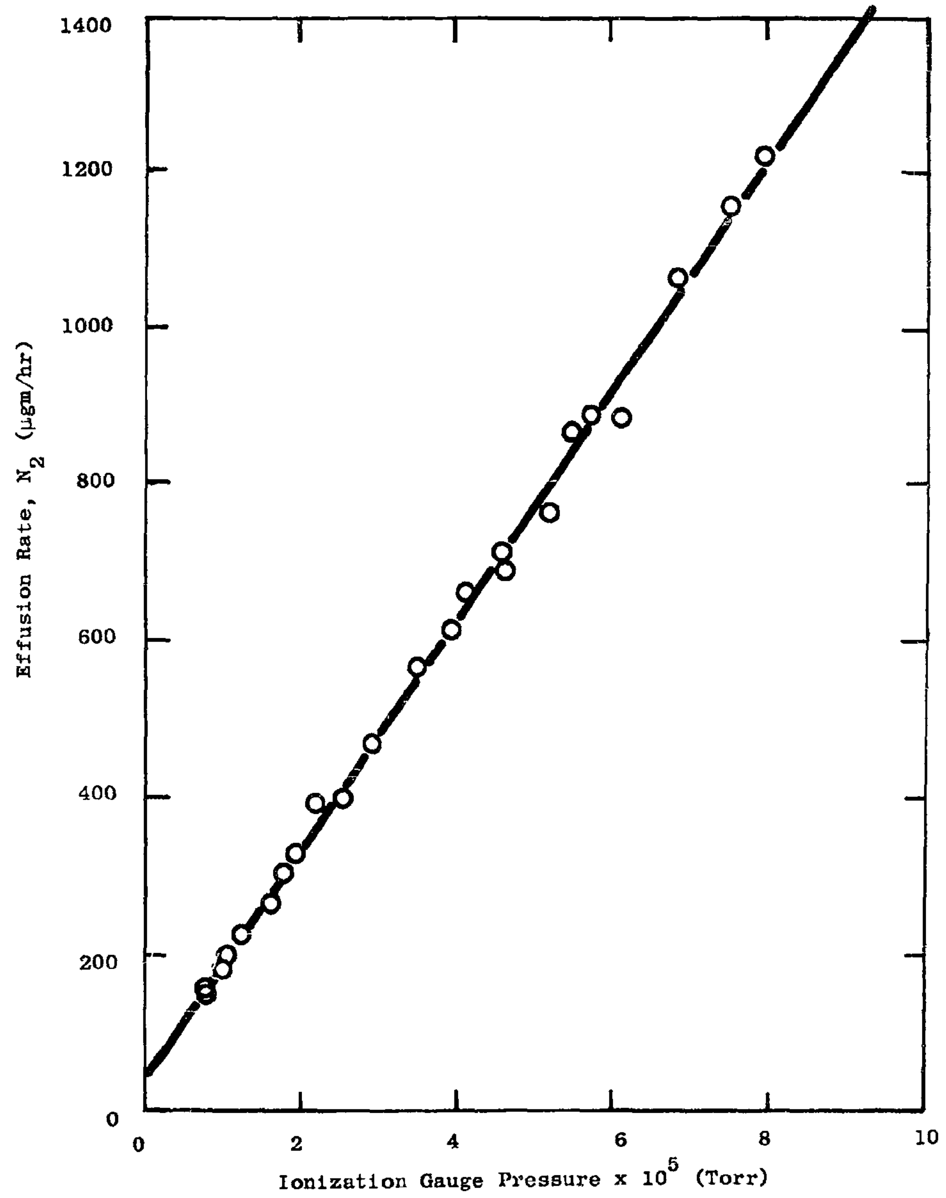

Figure 3. Typical Ionization Gauge Pressure Vs. Effusion Rate

$$\text{wt. fraction N} = \frac{w^{o} - \Sigma\Delta w}{W^{o} - \Sigma\Delta w} \qquad (3)$$

where $\Sigma\Delta w$ is the total loss of nitrogen from the beginning of the series of measurements to the time at which the composition is computed.

2. Results and Discussion

a. Zirconium Nitride Effusion Measurements

Reliable effusion measurements have been obtained in three separate series of runs each with a different cell with different orifice areas. Table 3 gives a summary of the composition data and a comparison of the different related values. The chemical analysis results are followed by the standard deviation from the mean of the several analyses made on each sample. By consideration of the standard deviations and sources of consistent errors in the procedure, it is estimated that the analytical data in Table 3 are accurate to ± 0.1 wt. % N. For the series VI measurements, the analytical data are inconsistent and it is thought that the initial wt. % N value is in error due to inhomogeneities in the sample.

Other experimental values given in Table 3 are essentially consistent in that the total wt. loss, which includes loss of nitrogen, zirconium and any impurities which may evaporate, should be greater than the nitrogen loss calculated by either method and the two calculated N losses should agree within the combined accuracy of all measurements involved.

We have chosen to facilitate calculation of the composition for each effusion measurement by assuming an initial weight of ZrN such that the nitrogen loss calculated by the two different methods are brought into exact agreement with the assumption that only nitrogen is lost. Actually, these assumptions introduce little, if any, additional inaccuracies. The resulting values which are used for further data reduction are also given in Table 3. For the series VI measurements, the composition was taken to be constant. With these values, the composition for each effusion measurement was computed from eq. 3, where $\Sigma\Delta w$ is calculated to the center of the time interval of the reading.

Table 3

COMPOSITION DATA FOR ZrN

	Chemical Analysis: wt % N				Calculated N loss (mgm)	
	Initial	Final	Initial wt. ZrN (mgm)	Total wt. loss (mgm)	From Recorder Chart	From Chemical Analysis
Experimental values:						
Series I	13.01 ± .11	9.74 ± .13	484.58	20.56	15.726	17.84
Series III	13.01 ± .02	11.07 ± .02	585.59	14.17	12.277	12.73
Series VI	8.20 ± .02	8.31 ± .01	451.22	1.22	0.580	-
Values used for data reduction						
Series I	13.01	9.74	434.07	15.726	15.726	15.726
Series III	13.01	11.07	562.78	12.277	12.277	12.277
Series VI	8.31	8.31	-	-	-	-

Effusing nitrogen was collected for a period of time which varied from four minutes to one hour depending on the effusion rate. The quantity of nitrogen collected was usually in the range from 3 to 100 micrograms. The nitrogen pressure within the cell was calculated from the usual Knudsen equation which, for nitrogen, reduces to

$$P_{N_2} = 4.262 \times 10^{-3} \; m/T \tag{4}$$

where P_{N_2} is the nitrogen pressure in atmospheres, m the rate of effusion (gm per cm^2 per sec) and T the absolute temperature (°K).

All data were adjusted to a series of temperatures so that the variation of P_{N_2} with nitrogen concentration at constant temperature could be obtained. This conversion was necessary because a given temperature could only be reproduced within about ± 10°K due to power fluctuations and lack of fine control on the power input. This adjustment was made by estimating the change of log P_{N_2} with reciprocal temperatures.

The data thus obtained for the three reliable series of measurements are given in Table 4 where the composition for each measurement is expressed as atom fraction nitrogen. For the Series I and Series III measurements, the adjusted temperatures are given. For the Series VI measurements, the actual measured temperatures are given.

In Fig. 4 the various pressure-composition isotherms are plotted as log P_{N_2} vs n_N, where n_N is the atom fraction of nitrogen. In Fig. 5 constant composition plots of log P_{N_2} vs. $1/T$ are given. The Series I and Series III measurements were first plotted on Fig. 4 and cross plotted at constant composition to obtain points on Fig. 5, while the Series VI values were first plotted as log P_{N_2} vs $1/T$ (Fig. 5) and cross plotted at constant temperature to obtain points on Fig. 4.

When pressures are measured dynamically, as is done here, departures from equilibrium behavior may occur as a result of slow rates of certain solid-vapor or solid-solid transformation. Some examples of such behavior have been given by Veleckis et al(3). Particularly applicable to the present study is the effect which occurs when evaporation from the surface of a solid takes place more rapidly than diffusion within the solid. If such is the case, then the surface of the solid is depleted in the more volatile constituent and the measured pressure is lower than that corresponding to the overall composition of the solid. Actually, this effect must always be present to some extent since diffusion through the solid particles will not occur unless there is some concentration gradient. The effect, however, is minimized by using a large evaporating-surface-to-effusing-area ratio.

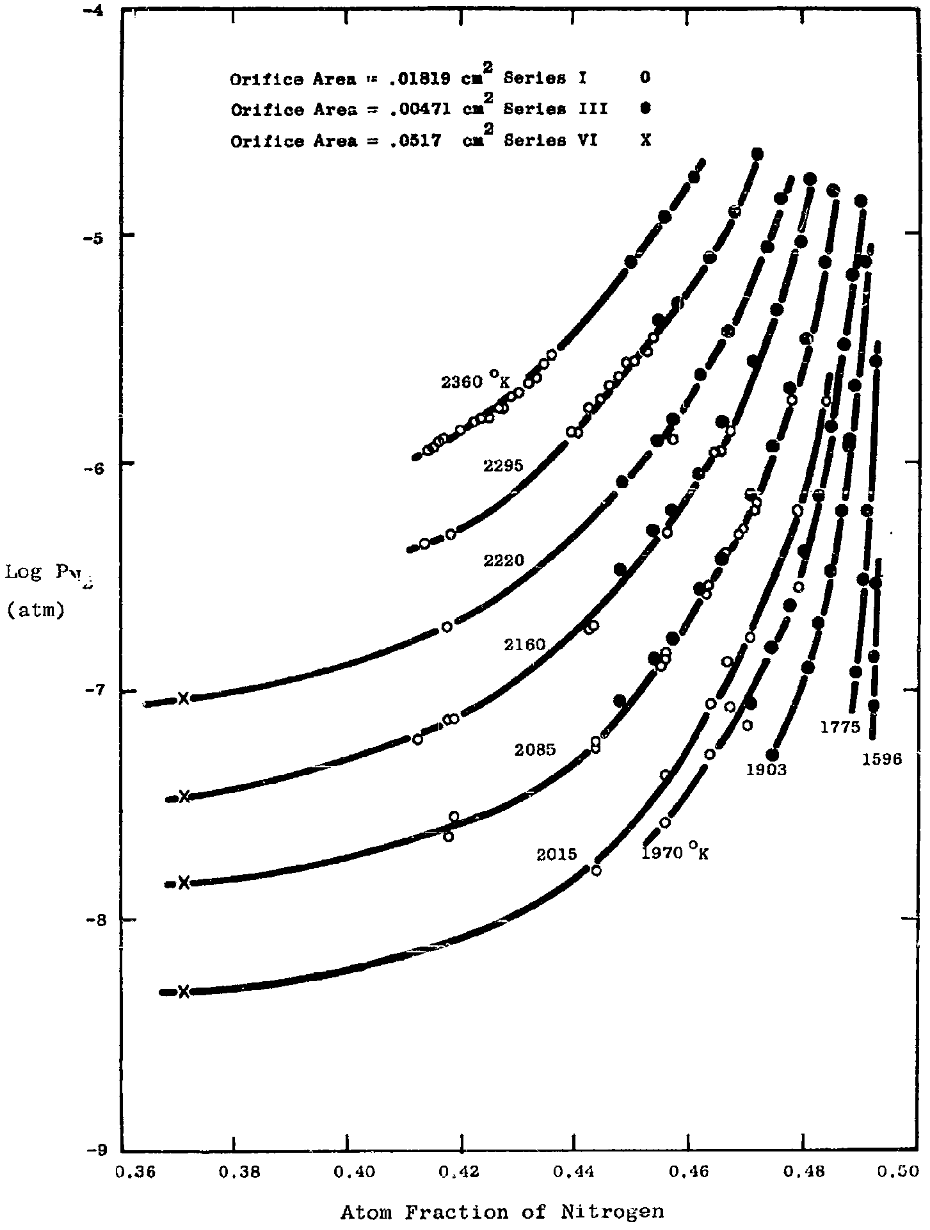

Figure 4. Pressure - Composition Isotherms for ZrN

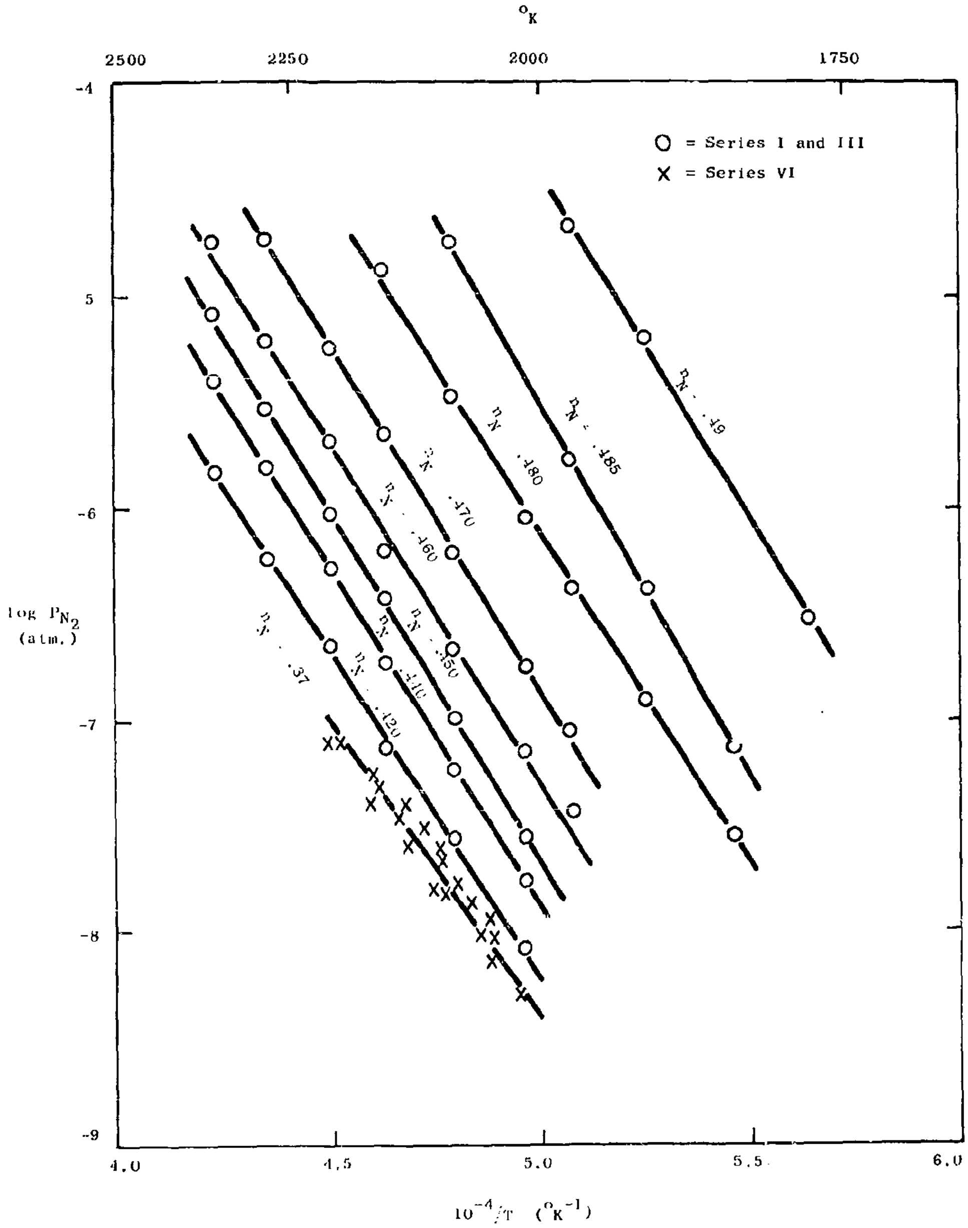

Figure 5. Nitrogen Pressure Vs Reciprocal Temperature At Various Compositions Of The ZrN Phase

Table 4

NITROGEN PRESSURE OVER ZrN

P_{N_2} = nitrogen pressure in atmospheres

n_N = atom fraction of nitrogen in ZrN

Series I measurements: orifice area = 0.01819 cm^2

T (°K)	log P_{N_2}	n_N	T(°K)	log P_{N_2}	n_N	T(°K)	log P_{N_2}	n_N
1970	-6.55	.4789	2085	-7.21	.4433	2295	-5.54	.4487
1970	-7.13	.4698	2085	-7.23	.4432	2295	-5.62	.4471
1970	-7.05	.4663	2085	-7.54	.4185	2295	-5.66	.4458
1970	-7.27	.4636	2085	-7.62	.4174	2295	-5.72	.4420
1970	-7.56	.4554				2295	-5.78	.4417
			2160	-5.54	.4726	2295	-5.87	.4404
2015	-5.72	.4834	2160	-5.85	.4666	2295	-5.86	.4390
2015	-6.20	.4785	2160	-5.94	.4651	2295	-6.29	.4179
2015	-6.75	.4705	2160	-5.94	.4641	2295	-6.34	.4131
2015	-6.86	.4661	2160	-6.06	.4615			
2015	-7.04	.4634	2160	-6.28	.4558	2360	-5.52	.4357
2015	-7.35	.4553	2160	-6.32	.4543	2360	-5.57	.4347
2015	-7.77	.4434	2160	-6.69	.4429	2360	-5.63	.4300
			2160	-6.71	.4424	2360	-5.64	.4314
2085	-5.72	.4774	2160	-7.11	.4184	2360	-5.68	.4299
2085	-6.17	.4712	2160	-7.11	.4182	2360	-5.70	.4285
2085	-6.19	.4707	2160	-7.23	.4177	2360	-5.74	.4271
2085	-6.27	.4693	2160	-7.19	.4128	2360	-5.75	.4261
2035	-6.29	.4684				2360	-5.79	.4247
2085	-6.37	.4659	2220	-5.88	.4565	2360	-5.79	.4231
2085	-6.41	.4655	2220	-6.70	.4170	2360	-5.81	.4222
2085	-6.52	.4632				2360	-5.85	.4193
2085	-6.56	.4627	2295	-5.30	.4577	2360	-5.88	.4163
2085	-6.83	.4556	2295	-5.44	.4531	2360	-5.90	.4157

Table 4 (Continued)

T(°K)	log P_{N_2}	n_N	T(°K)	log P_{N_2}	n_N	T(°K)	log P_{N_2}	n_N
2085	-6.85	.4551	2295	-5.50	.4521	2360	-5.92	.4148
2085	-6.88	.4549	2295	-5.54	.4505	2360	-5.94	.4140
SERIES III measurements: orifice area = .00471 cm^2								
1596	-6.52	.4923	1970	-5.83	.4846	2160	-5.55	.4709
1596	-6.82	.4920	1970	-6.12	.4822	2160	-5.82	.4656
1596	-7.04	.4920	1970	-6.36	.4799	2160	-6.04	.4615
			1970	-6.61	.4772	2160	-6.20	.4567
1775	-5.55	.4921	1970	-6.80	.4743	2160	-6.29	.4539
1775	-6.21	.4909	1970	-7.03	.4706	2160	-6.45	.4478
1775	-6.51	.4901						
1775	-6.91	.4887	2085	-4.80	.4848	2220	-4.83	.4759
			2085	-5.12	.4831	2220	-5.04	.4736
1903	-5.12	.4904	2085	-5.45	.4800	2220	-5.42	.4663
1903	-5.65	.4888	2085	-5.67	.4774	2220	-5.61	.4618
1903	-5.88	.4878	2085	-5.92	.4744	2220	-5.80	.4569
1903	-5.93	.4873	2085	-6.13	.4707	2220	-5.89	.4541
1903	-6.19	.4862	2085	-6.42	.4655	2220	-6.08	.4479
1903	-6.46	.4845	2085	-6.54	.4614			
1903	-6.69	.4821	2085	-6.77	.4567	2295	-4.64	.4718
1903	-6.88	.4805	2085	-6.85	.4538	2295	-4.88	.4677
1903	-7.27	.4743	2085	-7.03	.4477	2295	-5.08	.4632
						2295	-5.29	.4575
1970	-4.85	.4894	2160	-4.75	.4809	2295	-5.37	.4545
1970	-5.17	.4881	2160	-5.02	.4790	2295	-5.55	.4484
1970	-5.47	.4867	2160	-5.32	.4750			
SERIES VI measurements: orifice area = 0.0517 cm^2								
2046	-8.05	.371	2069	-7.87	.371	2142	-7.46	.371
2049	-7.94	.371	2084	-7.77	.371	2167	-7.31	.371
2047	-8.14	.371	2059	-8.02	.371	2135	-7.60	.371
2022	-8.23	.371	2096	-7.82	.371	2175	-7.39	.371
2102	-7.62	.371	2110	-7.80	.371	2210	-7.11	.371
2098	-7.66	.371	2139	-7.40	.371	2224	-7.10	.371
2120	-7.52	.371	2174	-7.25	.371	-	-	-

Good evidence that true equilibrium pressure was established, at least at the high nitrogen contents, is the excellent agreement between the Series I and III measurements as shown in Fig. 4. If the above mentioned effect were appreciable, the measurements made with the smaller orifice area should be higher than those obtained with the larger orifice area. However, the scatter in the Series VI measurements is believed to be caused by this non-equilibrium effect; the material tended to sinter together, thus presenting a smaller evaporating surface. Even though these measurements were restricted to the lower temperatures to minimize the sintering, a definite decrease in pressure with time at temperature was noted. Thus measurements at the lowest concentrations are not as accurate as those at the higher nitrogen concentrations.

Three attempts were made to measure the nitrogen pressure over the two phase solid, α Zr plus ZrN. In each of these attempts, the material solidly sintered together and low nitrogen pressures were obtained.

Some X-ray diffraction patterns have been obtained which roughly locate the low nitrogen limit of the ZrN phase. A summary of the results is given in Table 5 which shows the phases present and the lattice parameter of the ZrN phase. These results indicate that the low nitrogen limit of the ZrN phase lies between 8.3 and 7.0 wt. % N. This is in agreement with Smagina et al(4a) who prepared single phase ZrN with as little as 7.9 wt. % N. The best estimate, then, seems to be that the low nitrogen limit of the ZrN phase lies somewhere between 7.0 and 7.9 wt. % N. This is, however, in disagreement with the published (5) phase diagram of the Zr-N system, which shows the boundary extending only to about 11.5 wt. %N. Lattice parameters of the ZrN phase have been measured by Smagina et al.(4a) who found a value of 4.5866 ± 0.001 Å to apply over the range of 7.9 to 13.3 wt. % N. In a later article, the same authors (4b) reported values between 4.577 and 4.584 for compositions in the range 9.7 to 12.8 wt. % N. The data in Table 5 are in essential agreement with these latter values. Equilibrium nitrogen pressures in the latter report (4b) are considerably higher than those found here, however.

In a study of the vaporization of ZrN by Hoch, et al,(6) a nitrogen pressure of about 5×10^{-6} atm. at 2330°K was reported. It was concluded that this value was essentially consistent with the accepted heat of formation of ZrN. However the authors did not consider the wide range of homogeneity of the ZrN phase, but rather assumed equilibrium between stoichiometric ZrN and solid Zr. It seems likely, from the data of Figure 4, that the material they studied was the ZrN phase of approximately $n_N = 0.45$ composition.

Table 5

X-RAY INVESTIGATION OF VARIOUS ZIRCONIUM-NITROGEN COMPOSITIONS

Material	wt. % N	Phases Found	Lattice parameter of ZrN (Å)
Series I; Final Analysis	9.74	ZrN	4.580
Series VI; Final Analysis	8.31	ZrN	4.583
	6.95	ZrN + α Zr	4.585
	6.60	ZrN + α Zr	-

Brewer (7) also assumed that no range of homogeneity of the ZrN phase exists and, from the thermodynamic data available, estimated an equilibrium pressure over the stoichiometric ZrN of 10^{-5} atm. at 2500°K. It is apparent from Fig. 4 that this estimate is too low by a factor of at least 10^4.

b. Thermodynamic Calculations: Zirconium Nitride

Following Searcy (8), the standard state of nitrogen is taken to be N_2 gas at one atmosphere pressure. Considering nitrogen a perfect gas, the activity of nitrogen atoms, a_N, is the square root of the N_2 pressure in atmospheres. The partial molal free energy of nitrogen atoms in the zirconium nitride phase, $\bar{F}_N$, is then

$$\bar{F}_N = RT \ln a_N = \frac{RT}{2} \ln P_{N_2} \qquad (5)$$

where R is the gas constant. $\bar{F}_N$ at various temperatures and compositions is readily obtained from the data in Table 4.

The partial molal enthalpy of nitrogen atoms in the zirconium nitride phase, $\bar{H}_N$, may be obtained from the relation

$$\frac{d \ln a_N}{d\left(\frac{1}{T}\right)} = \frac{\bar{H}_N}{R} \qquad (6)$$

$\bar{H}_N$ may thus be calculated from the slope of the lines shown in Fig. 5.

These partial molal quantities for the ZrN phase are shown in Fig. 6 where F_N is given only for the temperature 2085°K. $\bar{H}_N$ is essentially constant over the temperature range. The scatter in the values for H_N demonstrates the inaccuracy in the determination of this quantity.

In principle, if the activity of zirconium in the ZrN phase were known at any concentration in the range over which nitrogen pressures have been determined, then partial molal quantities for Zr could be calculated by making use of the Gibbs-Duhem equation in integral form (8). Once the partial molar quantities for Zr had been determined, enthalpy and free energies of the compound could be calculated for the various compositions. However, the activity of Zr has not been measured at any point in the ZrN phase composition range and it seems that no useful purpose could be served by estimating a value and thereby introducing additional uncertainties into the results. These calculations may be performed if and when Zr activities are obtained, possibly by a technique such as resonance line absorption.

c. Hafnium Nitride Effusion Measurements

The evaporation of HfN under high temperature, high vacuum conditions is very similar to that of ZrN and so the same experimental and calculation procedure previously described for ZrN has been used for HfN.

Three series of effusion measurements have been made on HfN; the reliability of all three series is somewhat questionable, as will be shown later. Table 6 gives a summary of the composition data and a comparison of the different related values. The chemical analysis results are followed by the standard deviation from the mean of the several analyses made on each sample. The accuracy is estimated to be about ± 0.07 wt. % for each analysis. The data of Table 6 are all internally consistent in that calculated N losses by the two methods are in agreement within the combined accuracy of the two methods, and all calculated N losses are less than the measured total weight loss. As with the ZrN, the values used for data reduction have been obtained in such a way as to bring all values into exact agreement with the assumption that only nitrogen is lost in the effusion measurements. The composition for each measurement is then calculated from eq. 3.

The HfN was initially prepared as a rather coarse powder so that difficulties involved in sintering of the material, as was encountered in the ZrN measurements, could be minimized. As it turned out, this was a rather unfortunate decision in that apparently saturation pressure in the cell with the coarse powder was not obtained. The first series of measurements on HfN were made with 0.985 gm. of the coarse powder in a cell with orifice area 0.03035 cm^2. The second

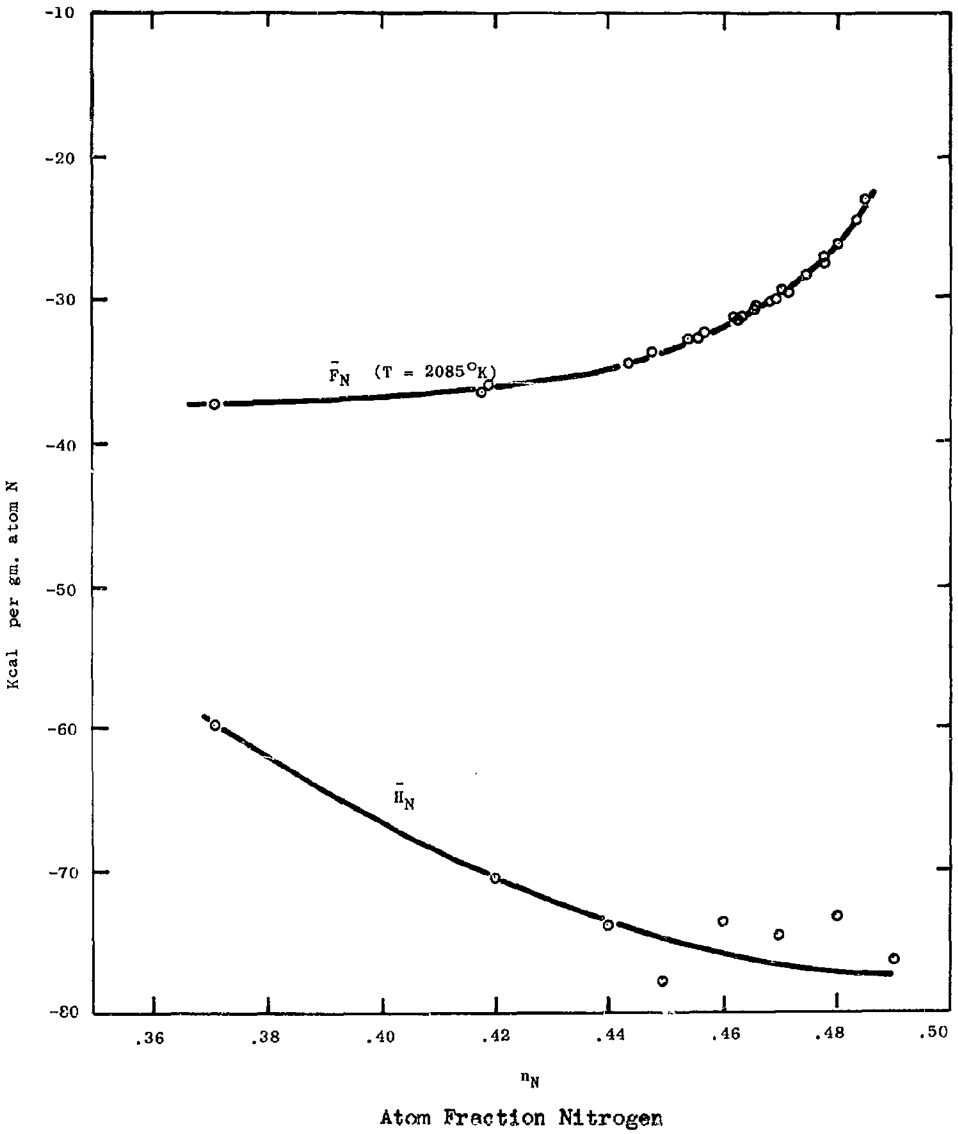

Figure 6. $\bar{F}_N$ at 2085°K And $\bar{H}_N$ For ZrN Phase

Table 6

COMPOSITION DATA FOR HfN

	Chemical Analysis: wt. % N				Calculated N loss (mgm)	
	Initial	Final	Initial wt. HfN (mgm)	Total wt. loss (mgm)	From Recorder Chart	From Chemical Analysis
Experimental values						
Series I	7.37 ± .02	5.91 ± .02	985.20	17.94	13.888	15.33
Series II	7.37 ± .02	5.19 ± .04	598.93	20.13	13.730	14.10
Series III	7.37 ± .02	6.16 ± .02	1532.69	24.23	19.646	20.04
Values used for data reduction						
Series I	7.37	5.91	890.89	13.888	13.888	13.888
Series II	7.37	5.19	597.13	13.730	13.730	13.730
Series III	7.37	6.16	1523.62	19.646	19.646	19.646

Table 7

NITROGEN PRESSURE OVER HfN

P_{N_2} = nitrogen pressure in atmospheres

n_N = atom fraction nitrogen in HfN

Series III: orifice area = .00629 cm^2: -200 mesh powder

T(°K)	log P_{N_2}	n_N	T(°K)	log P_{N_2}	n_N	T(°K)	log P_{N_2}	n_N
1490	-6.71	.5007	1823	-6.81	.4948	2031	-7.19	.4534
1490	-6.49	.5002	1823	-7.07	.4939	2031	-7.18	.4530
1490	-6.85	.4992	1823	-7.36	.4918			
1490	-7.50	.4983				2133	-4.98	.4911
			1931	-5.08	.4969	2133	-5.28	.4883
1601	-5.66	.5006	1931	-5.27	.4964	2133	-5.53	.4852
1601	-5.77	.4998	1931	-5.43	.4960	2133	-5.76	.4813
1601	-6.12	.4990	1931	-5.57	.4955	2133	-6.02	.4753
1601	-6.63	.4983	1931	-5.89	.4946	2133	-6.31	.4641
1601	-6.96	.4976	1931	-6.11	.4938	2133	-6.47	.4569
1601	-7.63	.4968	1931	-6.44	.4917	2133	-6.54	.4533
			1931	-6.55	.4909			
1715	-5.29	.4993	1931	-6.84	.4881	2238	-4.76	.4859
1715	-5.89	.4981	1931	-7.07	.4857	2238	-4.87	.4843
1715	-6.21	.4976	1931	-7.31	.4815	2238	-5.02	.4806
1715	-6.87	.4968				2238	-5.25	.4746
1715	-7.22	.4963	2031	-5.02	.4949	2238	-5.63	.4639
1715	-7.13	.4963	2031	-5.23	.4940	2238	-5.79	.4566
1715	-7.43	.4959	2031	-5.59	.4919	2238	-5.88	.4530
			2031	-5.73	.4907			
1823	-5.16	.4984	2031	-6.07	.4880	2356	-4.32	.4820
1823	-5.45	.4978	2031	-6.25	.4856	2356	-4.51	.4759
1823	-5.92	.4967	2031	-6.51	.4815	2356	-4.76	.4704
1823	-6.17	.4962	2031	-6.76	.4754	2356	-4.92	.4645
1823	-6.38	.4959	2031	-7.04	.4642	2356	-5.10	.4572
1823	-6.61	.4954	2031	-7.14	.4570	2356	-5.12	.4536

series of measurements was made with a cell with larger orifice area (0.05148 cm^2) and less material (0.599 gm) in order that measurements could be extended both to lower pressures and lower nitrogen content. The results of this series gave nitrogen pressures considerably lower than the Series I measurements, which definitely indicated lack of saturation in the cell, probably due to the diffusion rate of nitrogen being slow compared to the overall evaporation rate.

In an attempt to overcome this lack of saturation, the Series III measurements were undertaken after first grinding and sieving the material to -200 mesh powder. In addition to the finer powder, a smaller orifice (0.00629 cm^2) and larger amount of nitride (1.533 gm) were used. Nitrogen pressures generally higher than both Series I and Series II were obtained. Thus while the Series III measurements are certainly closer to the true equilibrium nitrogen pressure for the HfN phase, there is no evidence that saturation has actually been reached for this series.

In Figs. 7, 8 and 9, isotherms for the three series of measurements are compared for selected temperatures. As may be seen in Fig. 7, the three series of measurements are in reasonably close agreement for high values of n_N while at n_N less than about .49 the nitrogen pressure increases with decreasing effusion orifice area. This same behavior is further illustrated in Fig. 8 and 9 at higher temperatures.

It should be noted that the behavior just described is also typical of a system with a low evaporation coefficient. In fact, there is apparently no method to distinguish between the two effects. However, since the measurements are in reasonable agreement for n_N near .50 and since no such effect was found for ZrN, which is a similar system in other respects, the slow nitrogen diffusion rather than the low evaporation coefficient seems to be indicated.

Table 8

X-RAY INVESTIGATION OF VARIOUS HAFNIUM-NITROGEN COMPOSITIONS

Material	wt.% N	Phases found	Lattice parameter of HfN (Å)
Series I, II, III - Initial	7.37	HfN	4.514
Series I - Final	5.91	HfN	4.521
Series II - Final	5.19	HfN + α Hf	4.525
Series III - Final	6.16	HfN	4.522

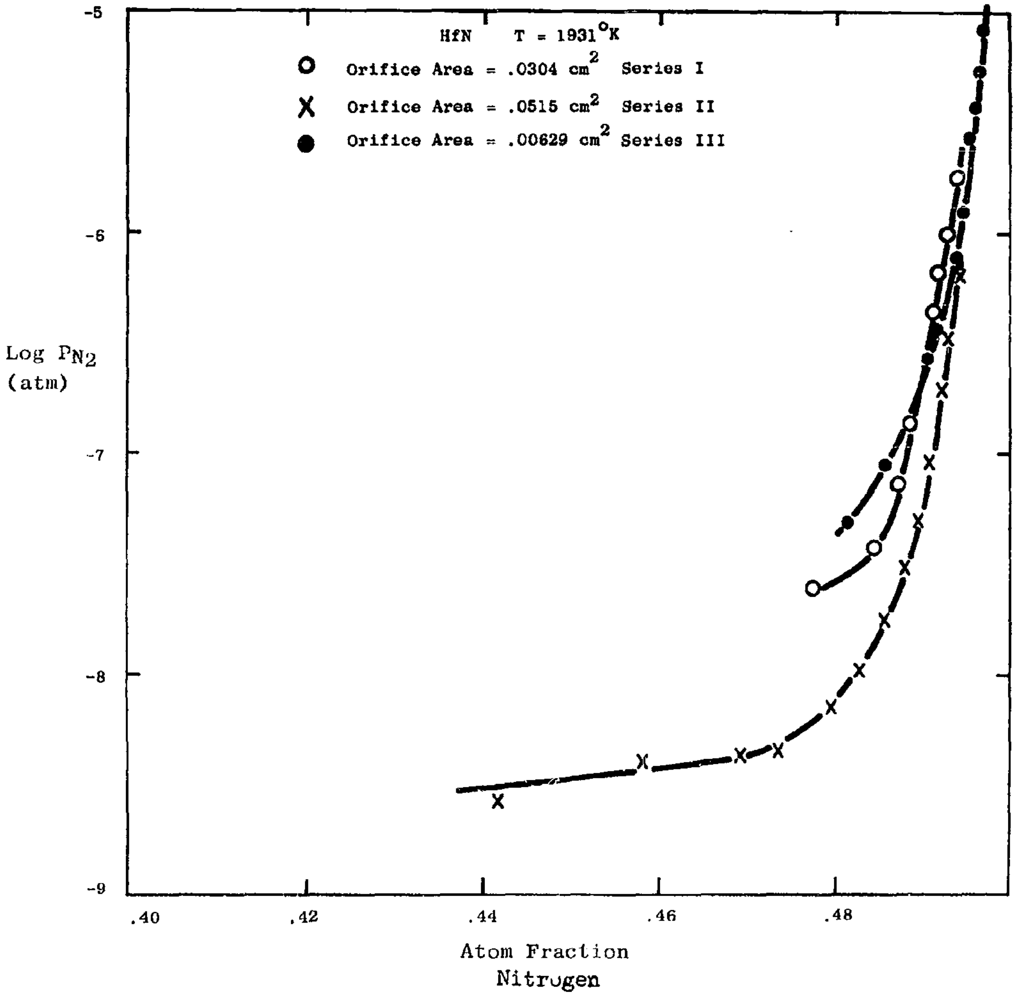

Figure 7. Nitrogen Pressure Vs Composition For HfN at 1931°K For Various Orifice Areas

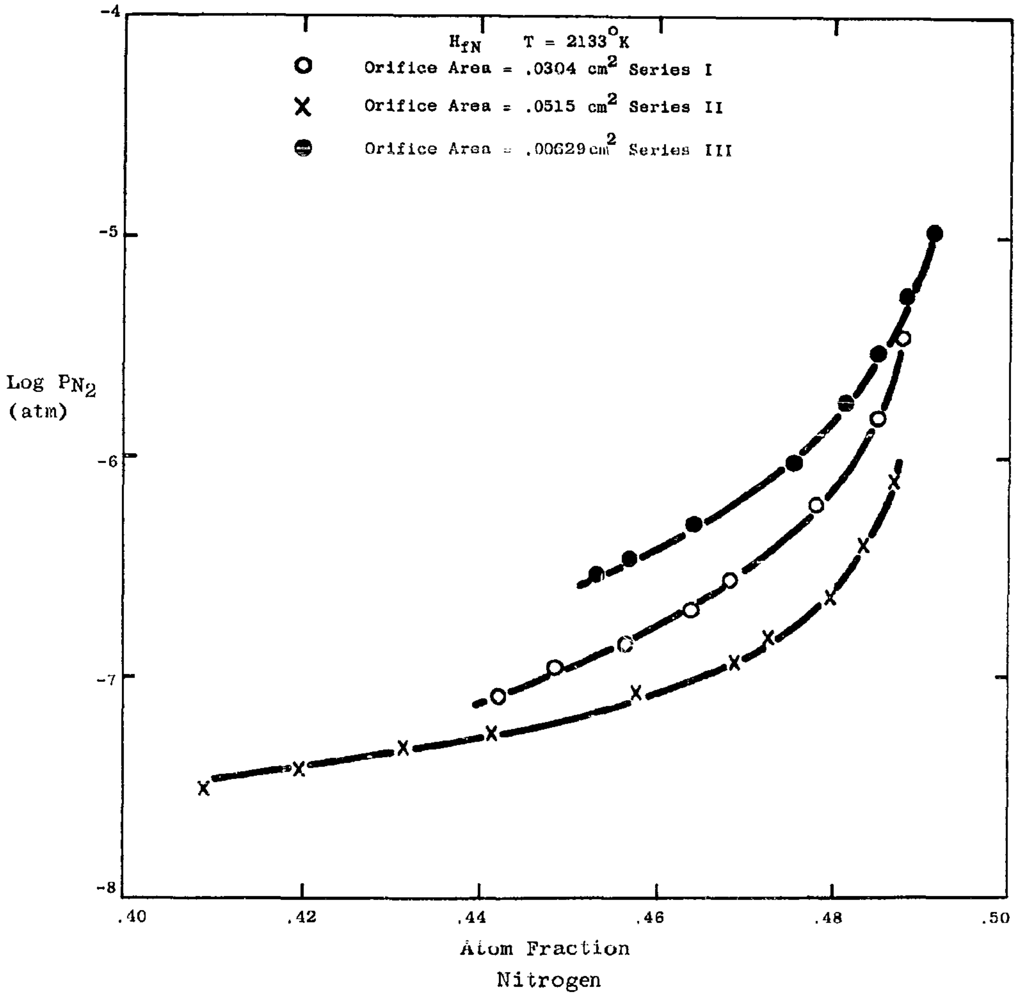

Figure 8. Nitrogen Pressure Vs. Composition For HfN at 2133°K For Various Orifice Areas

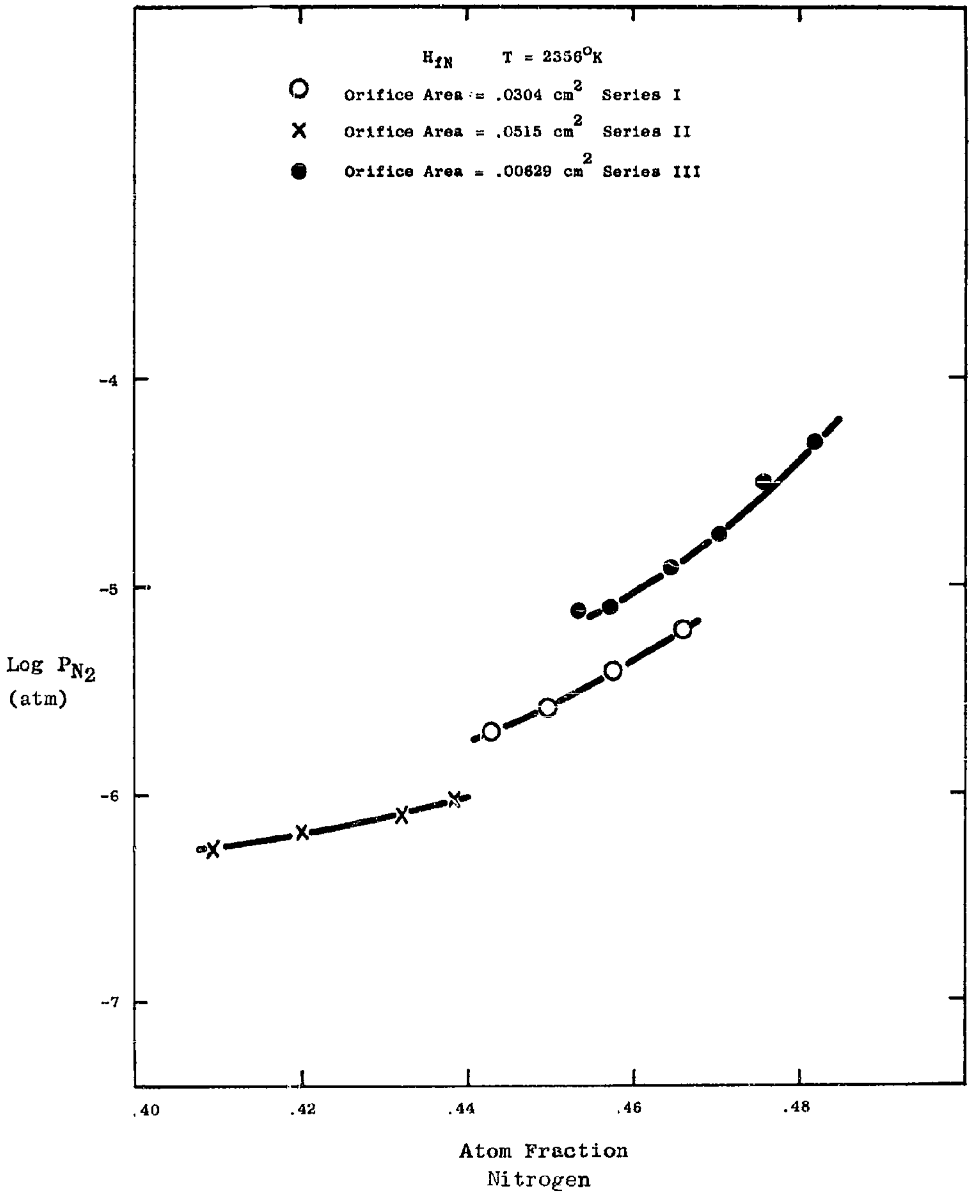

Figure 9. Nitrogen Pressure Vs. Composition For HfN At 2356°K For Various Orifice Areas

In view of the discrepancies in the three series of measurements described above, the complete results of only the Series III measurements will be presented here. Again, it should be noted that these data are approximate and that the true equilibrium pressure over the HfN phase may be higher than the values obtained. The results of the Series III measurements are given in Table 7 and the pressure - composition isotherms are plotted in Figure 10. Comparison with the ZrN measurements (see Fig. 4) will show that the nitrogen pressure over HfN is generally lower than that over ZrN at a given temperature and composition. For example, at 2360°K and n_N = .46 the nitrogen pressure over ZrN is higher by a factor of about 1.8.

Some X-ray diffraction patterns of various hafnium-nitrogen compositions have been obtained. A summary of these results is given in Table 8. The lattice parameter of HfN varies little over the range of homogeneity and has the value 4.521 Å. Although α Hf was found in the final product from the Series II measurements, this does not necessarily indicate that the overall composition is below the phase boundary, since as was pointed out above, the slow diffusion of nitrogen is thought to have caused inhomogeneity in this material.

3. Conclusions

The modified Knudsen method described here is applicable to the measurement of the pressure of a permanent gas in equilibrium with a solid phase. The application of this technique to the ZrN and HfN systems, however, is complicated by a number of factors. The first of these is the very rapid increase of nitrogen pressure with increasing nitrogen content near stoichiometric which necessitates an accurate determination of the nitrogen concentration in the solid. Secondly, the wide homogeneity range of these systems, which in the case of the ZrN phase was shown to extend to about $ZrN_{0.55}$, necessitates a large number of measurements to cover the homogeneity range. Third, the tendency of the ZrN to sinter together at low nitrogen contents prevented accurate measurements at nitrogen concentrations near the two-phase boundary. Finally, for the HfN phase, a dependence of nitrogen pressure on orifice size has been noted which is thought to be due to the fact that evaporation from the solid surface takes place more rapidly than diffusion within the solid, and hence prevents equilibrium pressure from being established within the cell. For this reason, the data presented here for HfN may be lower than the true equilibrium pressure.

The measurements of nitrogen pressure over the ZrN phase reported here indicate that the pressure over the stoichiometric nitride is several orders of magnitude greater than previous measurements (6) and estimates (7). The origin of this discrepancy is that these other investigators did not factor into their calculations the wide homogeneity ranges of the ZrN phase.

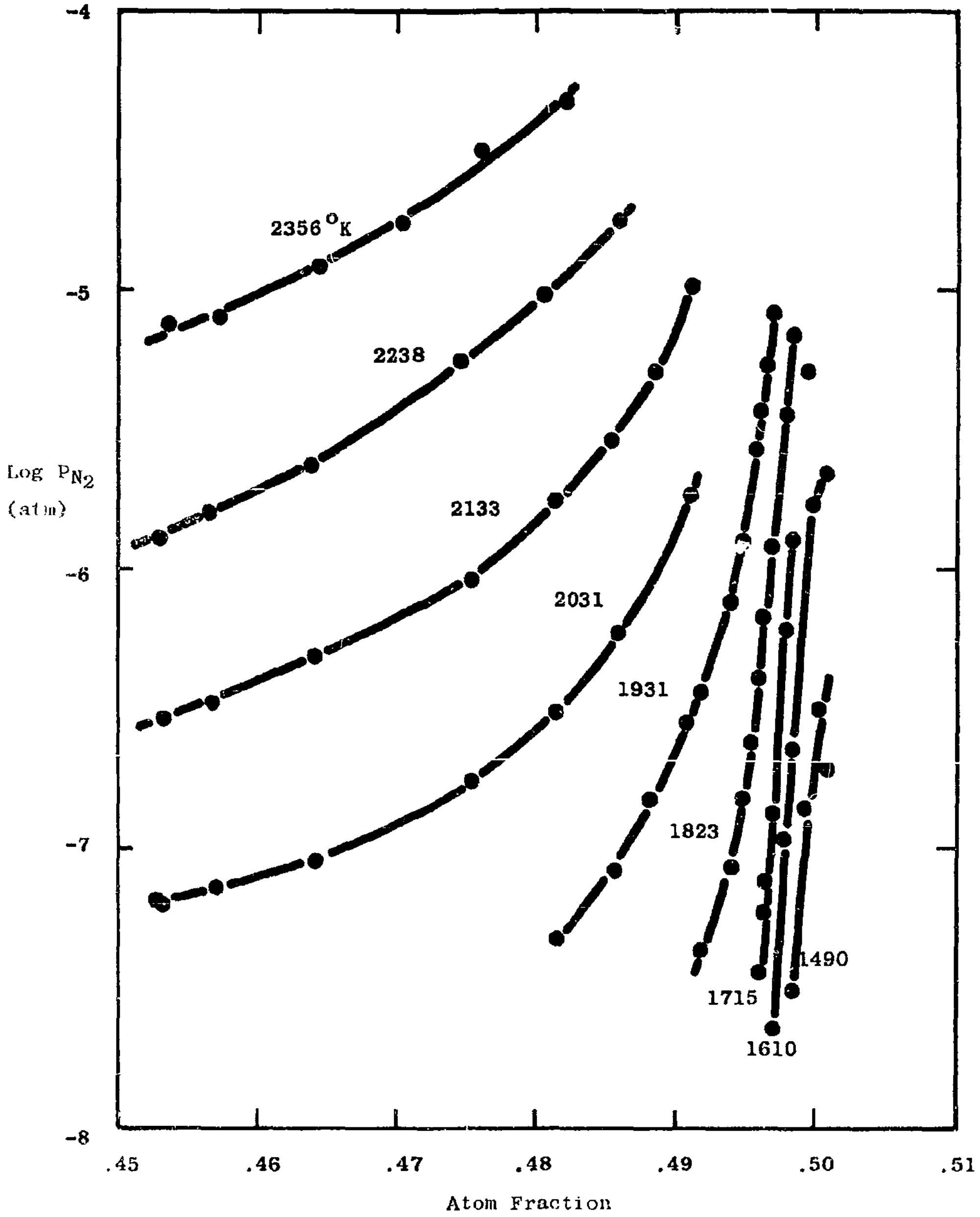

Figure 10. Pressure Composition Isotherms for HfN. Series III Measurements.

C. Vapor Pressure of Hafnium

1. Experimental

The vapor pressure of hafnium has been measured by the Langmuir method using a ring-shaped specimen. The apparatus used was the same as for the nitride vaporization (Fig. 1) except that the specimen was supported on tungsten rods as described in a previous (9) report.

The sample was prepared from the hydrided crystal bar hafnium which had been used to prepare hafnium nitride. This material was first heated to about 900°C under vacuum to remove the hydrogen. Chunks of the resulting metal were then consolidated into a button about 3/4" in diameter by electron beam melting in a copper mold. This button was then machined to the form of an annular ring, 5/8" OD, 3/8" ID and 1/8" thick. Four black body holes .016" diameter and .090" deep were drilled into the upper surface of the ring. These holes were equally spaced on a 1/2" diameter circle.

Vacuum fusion analysis of the dehydrided material (before melting) showed 69 ppm O, 81 ppm N, and 3 ppm H. A zirconium content of 1.13 wt. % is calculated from the Zr analysis of the nitride which had been obtained from the same material. As was stated previously, this material showed also traces of Fe, Mg, and Ti by spectrographic analysis.

High vacuum was always maintained in the system to prevent oxidation of the sample. Before each run, after the sample was sealed into the system and the system evacuated, the furnace chamber was flamed to remove adsorbed gas. Pumping on the cooled system then continued for about 16 hours after which time the pressure in the system was about 8×10^{-8} torr. The specimen was then heated to about 1600°C at a rate slow enough to keep the pressure below 5×10^{-7} torr. A temperature of 1600°C was then maintained until the system pressure fell below 1×10^{-7} torr which usually required about 15 minutes. The sample was then rapidly heated to the test temperature and the measurement begun. A pressure surge occurred on this rapid heating but again quickly fell below 10^{-7} torr and then more slowly to about 3×10^{-8} which is the ultimate vacuum of the system. Thus the heated specimen was never exposed to pressures above 5×10^{-7}.

During the first several measurements, the specimen temperature was found to decrease slowly but steadily. It was also noticed that small indentations occurred where the sample rested on the tungsten supports and that the sample tended to adhere slightly to the support. To overcome these difficulties, three small tabs of .005" tantalum sheet were spot welded to the hafnium in such a position that only the tantalum contacted the tungsten. Subsequent measurements showed that this step eliminated these effects and thereafter standard deviations from the mean temperature in a given run were never more than ± 8°K. It was later found, however, that the temperature decrease and sticking of the sample to the supports did not appreciably affect the measured rate of weight loss and so all measurements are reported below.

Effective temperatures for each run were calculated as described in a previous report (10). The correction was less than 1°K for runs without the tantalum tabs and only a small fraction of a degree for the later runs.

The mean coefficient of linear thermal expansion was estimated to be 5.7×10^{-6} per °K from the data of ref. 11. In calculating the area of the specimen, the linear dimension increase is thus approximately 1.08% of the room temperature dimension. The effective area of the inner curved surface of ring was calculated from the equation (12).

$$\text{Eff area} = \pi \ b \ (\sqrt{a^2 + b^2} - b) \tag{7}$$

where a is the inside diameter and b the thickness. This equation accounts for the fact that some atoms evaporating from the inner surface condense on the opposite side. The geometrical area was also corrected for the area covered by the tantalum tabs for those runs on which the tabs were used. No correction is necessary for the evaporation of tantalum since the vapor pressure of tantalum is lower than that of hafnium by a factor of about 10^4 in the temperature range of these measurements.

2. Results

a. Vaporization of Hafnium

The vapor pressure of hafnium was calculated from the rate of weight loss measurements with the assumptions that evaporation occurs to the monatomic vapor only and that the evaporation coefficient is unity. With these assumptions the Langmuir equation may be written

$$\log P = -2.773 + \log m + 1/2 \log T \tag{8}$$

where m is the rate of weight loss in gm per cm^2 per sec and P is the pressure in atmospheres. The atomic weight of hafnium is 178.6. The experimental data and the vapor pressure calculated from equation 8 are given in Table 9 and log P is plotted against reciprocal temperature in Fig. 11.

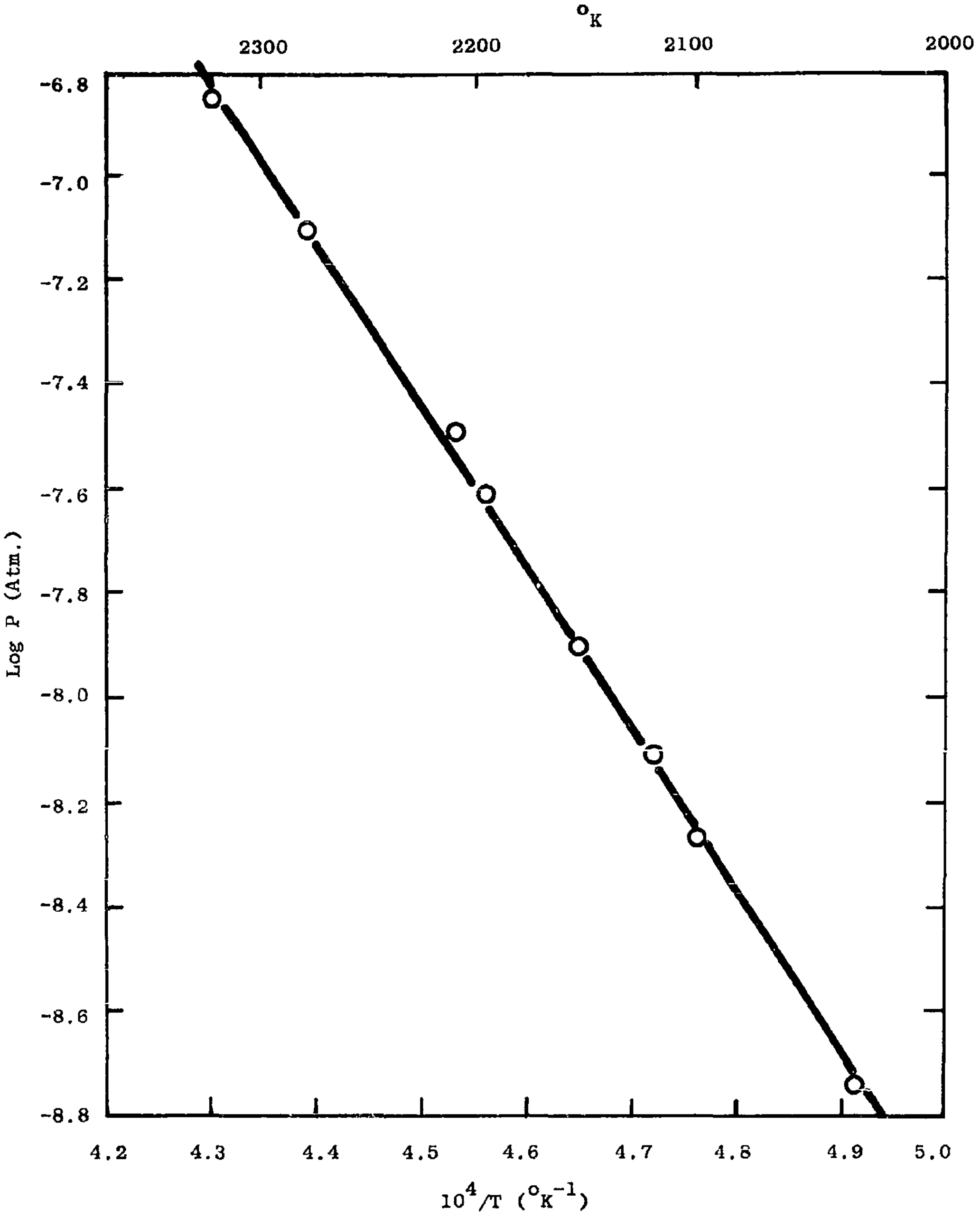

Figure 11. Vapor Pressure of Hafnium (Log Scale) Vs. Reciprocal Temperature

Table 9

EXPERIMENTAL DATA AND CALCULATED VAPOR PRESSURE OF HAFNIUM

T (°K)	wt. loss (mgm)	effective area (cm^2)	time (sec)	m (gm/cm^2sec)	log P (atm)
2035	1.50	4.403	14340	2.38×10^{-8}	-8.741
2100	2.53	5.011	7200	7.01×10^{-8}	-8.266
2119	3.25	4.403	7260	1.016×10^{-7}	-8.103
2151	5.92	5.011	7380	1.600×10^{-7}	-7.902
2192	6.36	4.403	4680	3.09×10^{-7}	-7.615
2206	13.04	4.403	7260	4.08×10^{-7}	-7.490
2277	10.39	4.403	2400	9.83×10^{-7}	-7.106
2325	7.99	5.011	900	1.772×10^{-6}	-6.851

Comparison with estimated pressures (13) shows the estimate to be less than the values measured here by a factor of about 100.

The standard heat of formation of atomic hafnium vapor (the heat of vaporization) may be calculated from the vapor pressure measurements with a knowledge of the free energy functions of both the solid and vapor. Available values (13) for the free energy function of the solid are based on inaccurate transition and melting temperatures and estimated high temperature specific heats. Since recent determinations of all these parameters have been made, a complete recalculation of the thermodynamic properties of condensed phase hafnium seems warranted.

The recently reported (14) high temperature enthalpy measurements (530 to 1880°K) were corrected for the 1% Zr content of the sample and corrected to a reference temperature of 298.15°K. Taking the specific heat at 298.15°K to be 6.10 cal per °K per gm atom(13), these data were fit to an analytical enthalpy expression by the method of Shomate (15). The enthalpy and corresponding specific heat expressions thus found were

$$H_T^o - H_{298}^o = 5.39T + 1.19 \times 10^{-3}T^2 - 1713 \qquad (9)$$

and

$$C_p^o = 5.39 + 2.38 \times 10^{-3}T \quad (10)$$

where $H_T^o - H_{298}^o$ is the enthalpy change between the temperature T(°K) and 298.15°K and C_p^o is the specific heat (cal per °K per gm atom) obtained by differentiation of the enthalpy expression. These values were used to the transition temperature, taken to be 2048 ± 11°K (16) which is in agreement with 2033 ± 35°K (17). Specific heat above the transition temperature was estimated. The entropy change at the transition temperature was taken to be 0.87 cal per °K per gm atom. This value was estimated from the corresponding values for Ti and Zr (13). From the entropy change at the transition temperature, a heat of transition of 1780 cal per gm atom is obtained. The melting point was taken as 2495± 30°K (18) and, following ref. 13, the entropy of melting is estimated to be 1.9 cal per °K per gm atom which is the average value for body centered cubic elements. The heat of melting is then 4740 cal per gm atom. The entropy at 298.15°K was taken as 10.91 cal per °K per gm atom (13).

Thermodynamic properties of condensed phase hafnium to 3000°K thus calculated are given in Table 10. In this table, S_T^o is the standard entropy and $-(F_T^o - H_{298}^o)/T$ is the free energy function, F_T^o being the standard free energy at temperature T°K.

The free energy function from Table 10 along with the free energy functions for the vapor (13) have been used to calculate ΔH_{298}^o, the standard heat of formation of hafnium vapor at 298.15°K from the equation

$$\Delta H_{298}^o = T\left[-\left(\frac{F_T^o - H_{298}^o}{T}\right)_{vapor} + \left(\frac{F_T^o - H_{298}^o}{T}\right)_{solid} - R \ln P\right] \quad (11)$$

The experimental and tabular values used along with the calculated heat of formation are given in Table 11.

The resulting average value of the heat of vaporization of hafnium is 146.59 k cal per gm atom with a standard deviation from the mean of ± .24. This rather small standard deviation indicates good internal consistency of the data as does the fact that no appreciable trend with temperature is noted. The heat of formation of hafnium vapor in the temperature range of the measurements may be obtained also by the so-called "second law" method. The slope of the line in Fig. 11 calculated by the method of least squares yields 142.1 k cal per gm atom for the heat of formation at temperatures of about 2200°K. Using the tabulated enthalpy changes to 298°K for the solid and vapor, this "second law" method gives $\Delta H_{298}^o = 147.4$. This good agreement between

Table 10

THERMODYNAMIC PROPERTIES OF HAFNIUM (CONDENSED PHASES) TO 3000°K

Phase	T (°K)	C_p^o (cal/°K gm at)	$H_T^o - H_{298}^o$ (cal/gm at)	S_T^o (cal/°K gm at)	$-(F_T^o - H_{298}^o)/T$ (cal/°K gm at)
solid	298.15	6.10	0	10.91	10.91
↑	300	6.10	11	10.95	10.91
	400	6.34	633	12.74	11.15
	500	6.58	1280	14.18	11.62
	600	6.82	1950	15.40	12.15
	700	7.06	2640	16.46	12.69
	800	7.29	3360	17.42	13.22
	900	7.53	4100	18.30	13.74
	1000	7.77	4870	19.10	14.24
	1100	8.01	5660	19.86	14.71
	1200	8.25	6470	20.56	15.17
	1300	8.48	7310	21.23	15.61
	1400	8.72	8170	21.87	16.04
	1500	8.96	9050	22.48	16.45
	1600	9.20	9960	23.06	16.84
	1700	9.44	10890	23.63	17.22
	1800	9.67	11850	24.18	17.60
	1900	9.91	12820	24.70	17.96
↓	2000	10.15	13830	25.22	18.31
solid	2048	10.26	14320	25.46	18.47
solid	2048	9.00	16100	26.33	18.47
↑	2100	9.00	16570	26.56	18.67
	2200	9.00	17470	26.98	19.04
	2300	9.00	18370	27.38	19.39
↓	2400	9.00	19270	27.76	19.73
solid	2495	9.00	20120	28.11	20.04
liquid	2495	9.00	24860	30.01	20.04
↑	2500	9.00	24910	30.03	20.06
	2600	9.00	25810	30.38	20.45
	2700	9.00	26710	30.72	20.83
	2800	9.00	27610	31.05	21.19
	2900	9.00	28510	31.36	21.53
	3000	9.00	29410	31.67	21.87

the "second law" and "third law" (equation 11) methods is further evidence of the consistency of the data. The "third law" result is of course the preferred value. The heat of formation found here is some 21 kcal less than the best literature estimate (13). It is interesting to note, however, that Krikorian (19) has estimated ΔH^{o}_{298} for hafnium as 145 kcal per gm atom, in excellent agreement with the value found here. This estimate was made by noting the variation of heat of formation of the various elements across the 6th period of the periodic table.

Table 11

THERMODYNAMIC FUNCTIONS OF HAFNIUM VAPOR

T	log P	R ln P	$-(F^{o}_{T}-H^{o}_{298})_{g}/T$	$-(F^{o}_{T}-H^{o}_{298})_{s}/T$	ΔH^{o}_{298}
(°K)	(atm)	(cal/°K gm at)	(cal/°K gm at)	(cal/°K gm at)	(Kcal/gm at)
2035	-8.741	-40.00	50.57	18.43	146.80
2100	-8.266	-37.82	50.74	18.67	146.77
2119	-8.103	-37.08	50.79	18.74	146.49
2151	-7.902	-36.16	50.87	18.86	146.63
2192	-7.615	-34.84	50.98	19.01	146.45
2206	-7.490	-34.27	51.01	19.06	146.08
2277	-7.106	-32.52	51.19	19.32	146.62
2325	-6.841	-31.35	51.30	19.48	146.87
				Avg.	146.59 ± 0.24

Since the vapor pressure and heat of formation of hafnium measured here are approximately the same as the corresponding values for zirconium (13), one might reasonably inquire as to whether the zirconium (1.13 wt % or 2.21 atom %) in the sample has interferred with the measurement. If one assumes an ideal solution of zirconium in hafnium, it may be shown that the correction due to the evaporation of zirconium amounts to a decrease of about 1% in the calculated hafnium pressure and a corresponding increase of .02 in ΔH^{o}_{298}. This correction is well within the experimental accuracy and has been neglected. Further evidence of the negligible effect of the zirconium content is that no trend in the calculated ΔH^0_{298} was observed even though a total of 1.3% of the initial sample weight was evaporated.

b. Thermodynamic Properties of Hafnium Carbide

In a previous report (10), the vaporization of hafnium carbide was studied and a value $(\Delta H^o_{298})_{HfC} = 361.3$ k cal per mole for vaporization to the monatomic elements was obtained by the second law method. Using the presently determined value for the heat of formation of Hf vapor, 146.59 k cal per gm atom and the well known (13) heat of formation of monatomic carbon, 170.9 k cal per gm atom, one obtains − 43.8 k cal per mole for the standard heat of formation of hafnium carbide. This is in excellent agreement with the estimate (11) of −44.7 k cal per mole, especially in view of the inaccuracy involved in the second law method. This second law heat of vaporization, however, implies that $(S^o_{298})_{HfC} = 16.5$ cal per mole per °K which is considerably larger than the estimate (11), 10.91. The latter value is apparently obtained by assuming that the entropy of HfC is the same as the metal.

3. Conclusions

Vapor pressures of hafnium have been measured in the temperature range 2035 to 2325°K by the Langmuir method. Thermodynamic properties of the solid have been calculated from recent literature data. The computed value for the heat of formation of hafnium vapor at 298.15°K is 146.59 k cal per gm atom.

Using this value, the previously reported (10) heat of vaporization of hafnium carbide yields a heat of formation of hafnium carbide at 298.15°K of −43.8 k cal per mole and a standard entropy at 298.15°K of 16.5 cal per mole per °K.

D. Matrix Isolation of Vapor Species from Thoria

In the preceding annual report (10) on this project, the apparatus used in these studies was described in detail. The method had also been used in other investigations and is described in the literature(20). The previous annual report, as mentioned above, gives details of the apparatus and the modifications made which allow temperatures as high as 3000°K to be reached. Temperatures as high as 2500°C were necessary in the present investigation of thoria.

1. Experimental

During the course of investigation on thoria, it was found necessary to make several more modifications in the existing equipment. These modifications were made primarily on the effusion cell containing the thoria. Previously, this cell consisted of a tungsten susceptor lined with a 2 mil iridium liner and an iridium lid having an orifice of 1/8". In addition, the sample consisted of a 3/8" x 1/8" rod of thoria. It was noted in several experiments that the temperature of the tungsten susceptor as read on the black body hole with an optical pyrometer was two to three hundred degrees hotter than the temperature of the sample as read directly through the orifice opening. Also, it appeared that the lid of the cell was much colder than the rest of the cell and condensation of the thoria took place on the under side of the lid. In addition, it was found necessary, in some cases, to work at temperatures higher than the melting point of iridium. For these reasons, a more conventional tungsten Knudsen cell was substituted. This cell is shown in Figure 12. As can be seen, it consisted of two pieces, the main body of the cell and a heavy tungsten lid. It should also be noted that the orifice opening was considerably reduced and the sample used consisted of finely powdered thoria. With these modifications, there appeared to be good temperature distribution throughout the cell. The removal of the iridium liner did not affect the resulting spectra. Figure 13 shows this cell mounted as part of the vapor source. Further modifications in the system were made to extend the spectral range into the visible and near ultraviolet regions. A 2-meter Bausch and Lamb spectrograph, having a linear dispersion of approximately 8Å /mm in the first order, was used for this purpose. By utilizing a hydrogen Beckman lamp and a tungsten filament lamp, measurements of the absorption spectrum could be made from 2000 Å to 10,000Å .

Matrix isolation of thoria was carried out from the tungsten Knudsen cell having an orifice diameter of approximately 2 mm at temperatures of 2100°C to 2700°C. The thoria used was obtained from the Linsey Chemical Division of the American Potash Company and was better than 99% pure; however, about 2%-3% water is absorbed by thoria under ambient conditions. Prior to matrix isolation, the sample was degassed in situ at temperatures higher than at which isolation was effected. In order to effect matrix isolation, the cell with its contents, located in the source unit as shown in Fig. 13 and carefully aligned with the liquid helium cooled window, was heated to the selected temperature. The effusing molecular beam strikes and freezes upon the cold window together with the matrix gas, argon in this case, a jet of which is directed upon the window from a separate source. Following isolation in the matrix, the absorption spectra were observed by passing the selected continuum through the deposit to the spectrograph. Details of procedure will not be described here further, having been adequately discussed elsewhere (20).

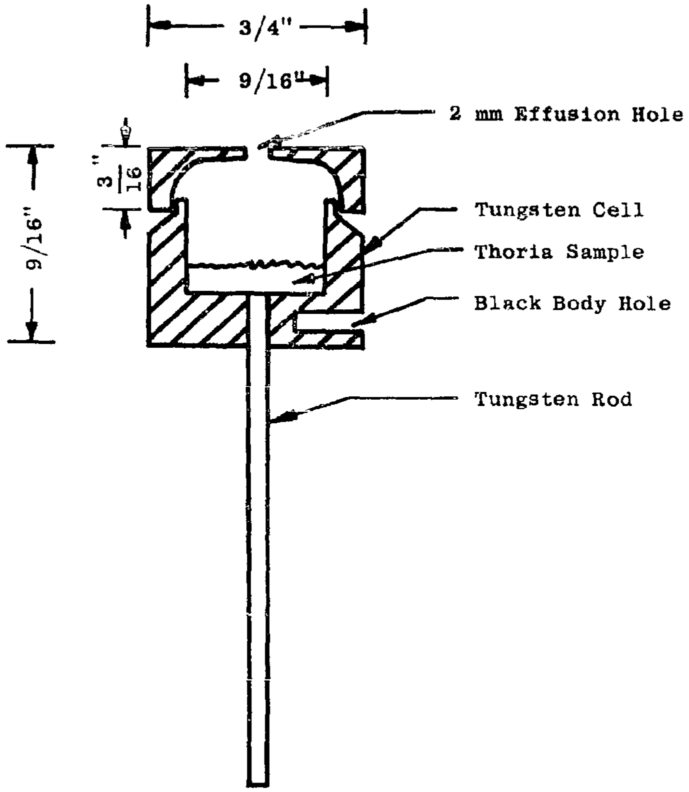

Figure 12. Tungsten Cell With Thoria Sample

A	Tantalum Radiation Shields	H	Tungsten Supports
B	Quartz Envelope	J	Quartz Sleeve
C	Quartz Window	K	Brass Header
D	Induction Coil	L	Water Inlet and Outlet
E	Orifice	M	Tungsten Rod
F	Knudsen Cell	N and P	Teflon Insulator and Plug
G	Black Body Hole	O	Water Jacket

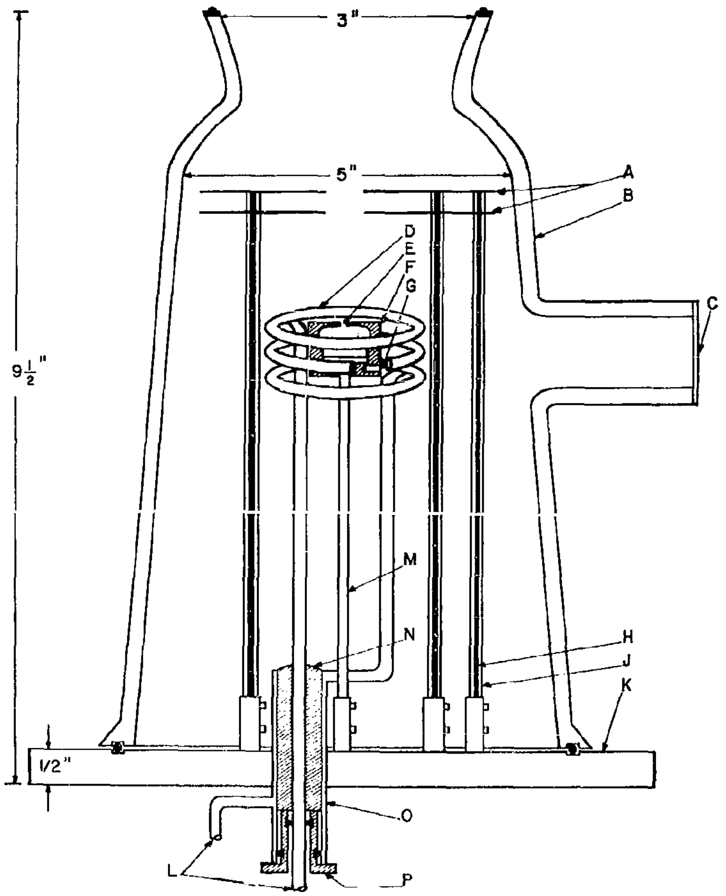

Figure 13. High Temperature Vapor Source For Matrix Isolation

It should be emphasized that, depending upon the ratio of vapor molecules to argon, significant variations in the spectra are observed. For this reason, isolation of ThO_2 was carried out at various dilutions ranging from approximately 100:1 to approximately 1000:1 argon to ThO_2. At high concentrations of ThO_2, additional bands appear which may be due to polymer formation, weak overtones and combinations. It has proved extremely helpful in the interpretation of the spectra to distinguish between spectra of "dilute" and "concentrated" matrices. Indeed, at the very high temperatures (2600°C - 2700°C) where the matrix is quite "concentrated", the resulting spectra are extremely complex and show little resemblance to the spectra of the more dilute matrices. For this reason, meaningful "concentrated" spectra were taken at a maximum temperature of 2400°C. Typical infrared spectra of "concentrated" and "dilute" matrices of ThO_2 in argon are given in Figure 14. In some cases, where the samples were not thoroughly degassed, bands around 1600 cm^{-1} were observed. These are due to matrix isolated water and indeed, after thorough degassing, they do not appear. The bands at 2138 cm^{-1} and 2342 cm^{-1} are difficult to ascribe to a thorium containing molecule and, indeed, they agree exactly with the fundamental for CO and the asymmetric stretching fundamental for CO_2 respectively. It might be mentioned that these same bands have been observed in other oxide systems (e.g. aluminum oxide). An analysis of a typical tungsten cell gave approximately 320 ppm carbon on the surface and 70 ppm on an interior sample. No doubt this carbon, introduced perhaps by machining processes, forms CO and CO_2 in the cell in the presence of an oxidizing atmosphere. This then becomes matrix isolated along with the thoria and accounts for the observation of these bands.

In order to determine which features of the spectrum given in Figure 14 are due to the species ThO_2 and ThO, a mixture of thoria and thorium metal were vaporized from the cell and trapped in an argon matrix. Under these conditions, the principal vapor species is ThO. A typical infrared spectrum is given in Figure 15. It is evident from this spectrum that the two bands at 877 cm^{-1} and 881 cm^{-1} are due to ThO and indeed these same two bands are observed in the spectrum of the vapor species over pure thoria (Figure 14). In order to determine the effect of tungsten on the spectrum of the vapor species over thoria, several experiments were carried out using a mixture of thoria and powdered tungsten metal. (No changes in the spectrum were evident.)

2. Results and Discussion

Table 12 lists the infrared frequencies which are believed associated with ThO and ThO_2 respectively.

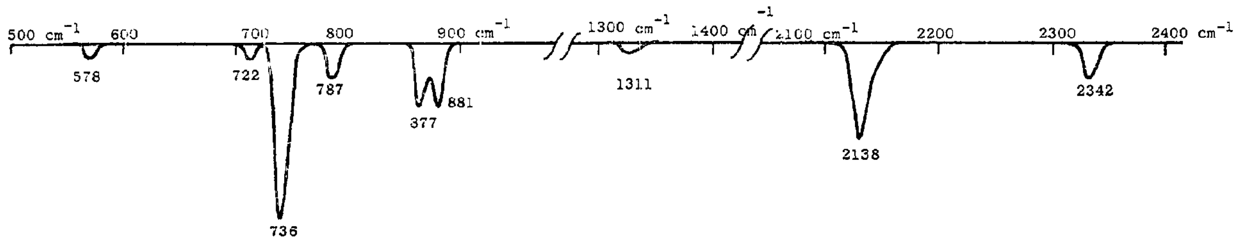

Concentrated Spectrum At 2400°C With 45 Min. Deposition

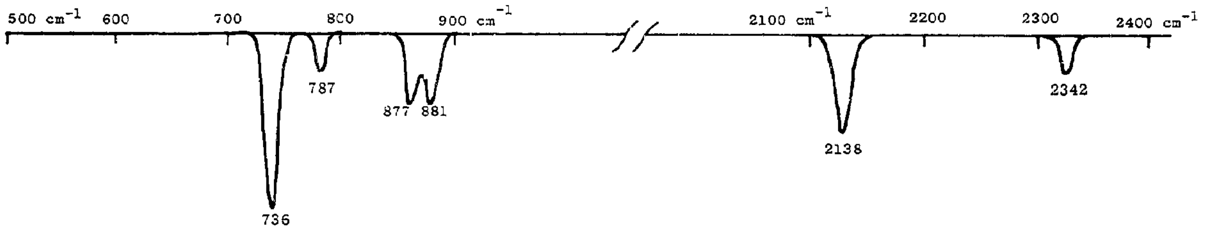

Dilute Spectrum At 2100°C With 3 Hr. Deposition

Figure 14. Observed Infra-Red Spectrum Of Vapor Species From Thoria In Argon Matrix

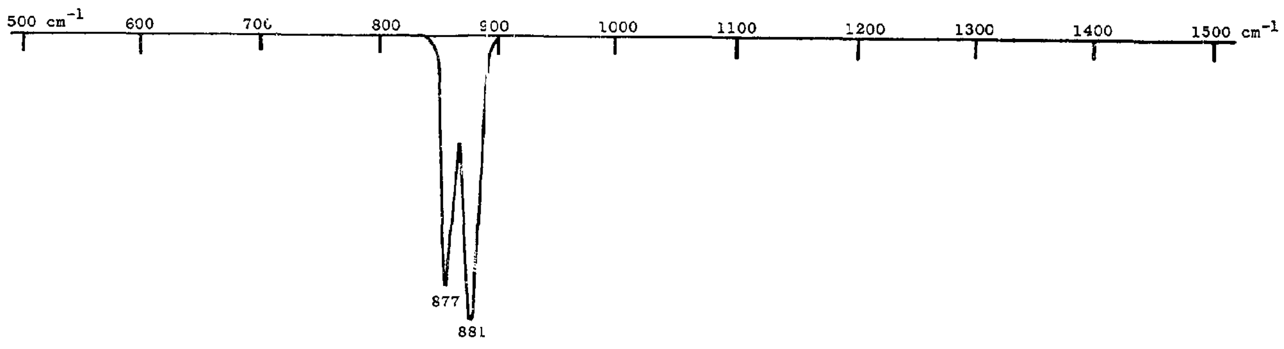

Figure 15. Observed Infra-Red Spectrum Of Vapor Species From Thoria-Thorium Mixtures In Argon Matrix At 2160°C With 45 Min. Deposition

Table 12

INFRARED FREQUENCIES FOR ThO AND ThO_2

Species	Frequency cm^{-1}	Remarks
ThO	877(w)	From Th and ThO_2
	881(w)	
		From ThO_2
	1311(v.w.)	concentrated spectra
	787(w.)	dilute and concentrated spectra
ThO_2	736(s.)	dilute and concentrated spectra
	722(w.)	concentrated spectra
	578(w.)	concentrated spectra

With regard to the visible and near ultraviolet absorption spectra observed for the vapor species from thoria, a mixture of thoria and thorium metal,and pure thorium metal, the spectra appear to be identical in all three cases. A typical spectrum is given in Table 13. It is clear that the only contributing species to the visible and near ultraviolet spectrum is due to thorium. Indeed, comparison (aside from a small matrix shift) of this spectrum with the literature spectrum for thorium confirms this point. Since the atomic spectrum of thorium has not been completely analyzed, this spectrum could prove quite useful in the analysis since it should represent transitions only from the ground state. This has not been done here.

It can be seen in Table 12 that the two bands at 877 cm^{-1} and 881 cm^{-1} are due to the ThO molecule. There is little doubt that these bands represent the fundamental vibrational frequency for this molecule with the splitting being due to either a matrix effect or to P and R branch rotational structure. Indeed, this splitting (4 cm^{-1}) leads to a B value ($\sim$ 0.6) for ThO (see Herzberg Spectra of Diatomic Molecules P 127) which is reasonable for this molecule. However, this should be taken tentatively because of the approximate nature of the calculation. From the value of the vibrational fundamental, taken as 779 cm^{-1}, a force constant for the ThO band can be calculated. The value for this force constant turns out to be:

$$K = 5.3 \times 10^5 \text{ dynes/cm}$$

This value seems to be entirely reasonable.

Table 13

VISIBLE AND ULTRAVIOLET SPECTRUM DUE TO THORIUM
(IN ARGON)

Wave Length Å	Intensity	Appearance	Remarks
2810	v.w.	b.	2400°C 50 min.
2827	v.s.	b.	deposition from
2895	m.s.	b.	Thoria
3021	w.	b.	2150°C from
3071	w.	b.	Th ThO_2
3094	w.	b.	
3101	w.	sh.	
3142	v.s.	m.b.	1800°C from
3173	w.	m.b.	Thoria
3190	w.	m.b.	
3218	w.	v.b.	
3264	s.	m.b.	
3382	w.	m.b.	
3487	w.	m.b.	
3508	w.	v.b.	
3587	v.s.	b.	
3603	v.s.	b.	
3794	v.w.	sh.	
3832	m.s.	v.b.	
3916	m.s.	sh.	
3918	m.s.	sh.	
3931	v.v.s.	v.v.b.	
4038	m.s.	v.v.b.	
4159	v.s.	m.b.	
4284	w.	m.b.	
4317	w.	m.b.	
4441	m.	m.b.	
4492	m.	m.b.	
4842	v.w.	m.b.	
4990	w.	v.b.	
5057	v.s.	v.b.	
6218	s.	v.b.	
6288	s.	v.b.	
6931	m.s.	v.b.	
7041	w.	v.v.b.	

The frequencies 1311 cm^{-1}, 787 cm^{-1}, 736 cm^{-1}, 722 cm^{-1} and 578 cm^{-1} have been shown to be due to the ThO_2 molecule. The bands 787 cm^{-1} and 736 cm^{-1} are present even in the dilute spectra with the 736 cm^{-1} band being much more intense. The other bands are present only in the concentrated spectra. If the configuration of ThO_2 is that of a linear symmetric molecule (i.e. $D_{\infty h}$), two infrared active fundamental frequencies are to be expected. These are the asymmetric stretch, ν_3 (Σ^+_μ), and the bend, ν_2 (π_μ), whereas the symmetric stretch, ν_1 (Σ^+_g) is inactive. If the configuration is non linear (i.e. C_{2v}), all three fundamentals should be infrared active. Furthermore, for a linear configuration, all odd overtones and combinations of infrared active fundamentals should be forbidden, whereas in the case of the nonlinear configuration, all overtones and combinations are allowed. Based upon the foregoing considerations, it is felt that the observed infrared spectrum of ThO_2 can best be explained using a near linear $D_{\infty h}$ configuration. There is little doubt that the very strong band at 736 cm^{-1} represents the asymmetric stretching frequency, ν_3. This is true for either the linear or nonlinear model. If the configuration is near linear, it is possible for the ν_1, symmetric stretching frequency to be active but quite weak. The frequency at 578 cm^{-1} is indeed weak, being present only in the concentrated matrix spectrum, and has been chosen for the ν_1 frequency. The bending frequency, ν_2, is most likely out of the spectral range of our equipment (< 300 cm^{-1}), however, the second overtone ($3\nu_2$) of this fundamental should be active and indeed 722 cm^{-1} has been assigned to this overtone. The vibrational frequency assignment is therefore, 736 cm^{-1} (ν_3), 578 cm^{-1} (ν_1) and 240 cm^{-1} (ν_2). This assignment is further corroborated by the explanation of the 787 cm^{-1} and the 1311 cm^{-1} bands as the combinations, $\nu_1 + \nu_2$, and $\nu_1 + \nu_3$ respectively. It should be noted that the observed overtone, $3\nu_2$, and the above combinations obey the linear model selection rules and that other overtones and combinations (e.g. $\nu_2 + \nu_3$ or $2\nu_2$) are missing from the spectra indicating further the reality of a near linear configuration for ThO_2. The final assignment for ThO_2 is given in Table 14.

Table 14

INFRARED ASSIGNMENT FOR ThO_2

Frequency	Assignment	Species
1311(v.w.)	$\nu_1 + \nu_3$	Σ^+_μ or B_1
787(w.)	$\nu_1 + \nu_2$	π_μ or A_1
736(v.s.)	ν_3	Σ^+_μ or b_1
722(w.)	$3\nu_2$	π_μ or A_1
578(w.)	ν_1	Σ^+_g or a_1
(240)*	ν_2	π_μ or a_1

* not directly observed

The species types are given for the linear ($D_{\infty h}$) and non linear (C_{2v}) models. This assignment leads to the following force constants for ThO_2:

$$K_1 = 3.8 \times 10^5 \text{ dynes/cm}$$

$$K_{12} = -0.67 \times 10^5 \text{ dynes/cm}$$

$$\frac{K_\delta}{l^2} = 0.24 \times 10^5 \text{ dynes/cm}$$

These appear to be reasonable.

3. Conclusions

The use of matrix isolation has been shown to be an effective method for obtaining the infrared spectrum of high temperature vapors. In the case of ThO_2, the observed spectrum leads to a reasonable assignment based on a near linear model. However, the assignment is tentative since it is based only on the observation of the infrared spectrum and no methods exist for the observation of the Raman Spectra of high temperature vapors. The fundamental stretching frequency has been observed for ThO and leads to a reasonable force constant for this molecule. It should be re-emphasized that great care be taken in this method to adequately isolate the molecule of interest in an inert matrix. Indeed with poor isolation all sorts of spurious effects are possible.

E. Resonance Line Absorption Photometry-Refractory Borides

The techniques of resonance line absorption have been used in the past to determine the free energies of formation of such materials as TiC, ZrC, and SiC. The apparatus, techniques and methods of calculation have been thoroughly described in previous annual reports (9, 10) and in several publications (21, 22, 23). It was the purpose of this investigation to adapt these methods to the investigation of the free energies of formation of refractory borides such as TiB_2 and ZrB_2. The material initially chosen for this investigation was TiB_2.

The vaporization of the diborides can be expressed as:

$$MB_2 \text{ (s)} = M \text{ (g)} + 2B \text{ (g)} \qquad (12)$$

and

$$\Delta F^o_{vap.} = - RT \ln P_M P_B^2 \qquad (13)$$

when this is combined with the expressions for the vaporization of the elements:

$$M(s, l) = M \text{ (g)} \qquad (14)$$

$$2B(s,l) = 2B(g) \qquad (15)$$

the free energy of formation is given as:

$$\Delta F^{o}_{formation} = RT \ln \left(\frac{P_M}{P'_M}\right) \left(\frac{P_B}{P'_B}\right)^2 \qquad (16)$$

where P' refers to the pressure of the element.

Therefore, in order to determine the free energy of formation of a diboride, it is only necessary to measure two pressure ratios: (1) the ratio of the pressure of the metal atom over the diboride to that of the pure metal and (2) the ratio of the pressure of boron over the diboride to that of pure boron. Indeed, if the vapor pressure of the pure elements are known sufficiently well (which is generally the case), the free energy of vaporization may also be determined. The technique of resonance line absorption is used to determine these relative pressures. Actually, in the case of TiB_2, it was necessary to create an invariant system by the addition of a condensed boron phase (this will be discussed in detail later on); and, therefore, only the relative titanium pressures were needed to obtain the free energies. As mentioned earlier, the apparatus, techniques and methods of calculation have been thoroughly discussed before and, therefore, only where changes have been made will specific details be given.

1. Experimental

a. Boron Resonance Line Absorption

Since no prior attempts had been made to use the resonance line absorption techniques in the case of boron, a program was initially undertaken for this purpose. It must be mentioned at the outset that, although measurements on the absorption of boron atoms were obtained, the data definitely indicated that the present technique led to erroneous results. However, it is felt that something is to be gained by a brief description of this phase of the work in helping to avoid similar difficulties in future applications.

As mentioned earlier, in the case of diborides, it is necessary to measure the relative absorption of boron over the boride and over pure boron metal. The boron resonance line at 2497.73 Å was chosen for measuring the absorption due to boron atoms and represents the transition $^2P_{3/2} - {}^2S_{1/2}$. This line was generated in our standard hollow cathode source by the addition of a small amount of powdered boron into the cathode cavity. It was found necessary to operate the cathode at at least 80 ma. to obtain sufficient intensity for good signal to noise. Several modifications of the cathode configuration were attempted and the necessary current was reduced to about 60 ma. In no case was it possible to obtain intensities similar to those used with other atoms (e.g. Ti, Si). It was felt that, since boron is relatively non-volatile, the low concentration of boron atoms in the cathode led to this rather low intensity. Furthermore, it was found necessary to run the cathode at ice temperatures instead of at the conventional liquid nitrogen temperatures to obtain sufficient intensity.

Probably the severest problem encountered in this investigation was in obtaining a suitable container for the boron metal. Typical absorption cells were fabricated from a variety of materials and powdered boron (Cooper Metallurgical's purest grade) was loaded into the cells. The materials initially tried were B_4C, SiC, graphite and Ta. In all cases, the boron metal reacted extensively with these materials when heated in the carbon resistance furnace. Boron nitride was tried and found to be a suitable container. A cylinder of boron nitride 6" long by 1" o.d. having 1/8" wall and fitted with boron nitride end pieces containing 1/4" orifices was used as the absorption cell for boron metal.

It was necessary to thoroughly degass the cell since it contained several percent of boron oxide as a binder. This was done by heating the cell under vacuum to a temperature of approximately 1900°C for several hours. The removal of the oxide was considered necessary since it could react with the boron metal. I/I_o measurements were taken on the absorption of the 2497.73 Å boron resonance line at various temperatures in the conventional manner. It was immediately obvious that, although the measurements were reproducible, they did not change with temperature as predicted from the known heat of vaporization of boron. That is, since $^{(21)}$

$$AP' = -T^{3/2} \ln I/I_o \qquad (17)$$

where A is a constant, P' the pressure of boron, T the absolute temperature, a quantity (AP) proportional to the vapor pressure can be obtained as a function of temperature. From a plot of the logarithm of this quantity against 1/T, the heat of vaporization could be determined. The heat determined in this fashion was some 60 kcal/mole lower than the known heat. It could, therefore, be concluded that the existing techniques could not be applied to the vaporization of boron.

In order to determine whether the difficulty was due to poor equilibrium between the boron vapor and the condensed phase or whether the spectroscopy was at fault, a Beckman hydrogen lamp was substituted for the hollow cathode and continuum absorption measurements on the boron resonance lines were carried out. By using the techniques of the curve of growth method, the heat of vaporization obtained from these continuum measurements was found to be in excellent agreement with the literature value. These results and methods are described in Appendix A.

It, therefore, was concluded that good equilibrium was obtained in the BN cell and that something was at fault with the hollow cathode spectroscopy. Indeed, it is quite conceivable that the assumption that the boron line generated in the hollow cathode was much narrower than the absorption line of the hot atoms in the furnace could be erroneous. If this assumption were not true, the apparent heat of vaporization would be lowered since the absorption would change much less rapidly with boron atom concentration. The possibility that the hollow cathode resonance line is indeed rather broad is further borne out by the unusual operating conditions that were necessary to achieve sufficient line intensity, namely, the need to run the cathode at high currents and at ice temperatures. Both these conditions would have a tendency to broaden the line.

As mentioned earlier, it is not necessary to measure the absorption of the boron atoms over a diboride in order to determine the free energy of formation if a boron containing condensed phase of known thermodynamic properties is added to diboride. In this case, the system is univariant and it is only necessary to measure the vaporization of the metal atoms (e.g. Ti over TiB_2). This is what was actually done in the present investigation of TiB_2 and is described in the following section. However, it is certainly possible to use the continuum method to obtain the relative pressures of the boron atoms (with no excess boron phase present) in conjunction with the resonance line method for the metal atoms. This has not been done as yet but it is anticipated that such measurements will be carried out in the forthcoming year to allow a cross check on our present results.

b. TiB_2 Measurements

As mentioned above, to determine the free energy of formation of TiB_2, a boron containing condensed phase of known thermodynamic properties was added to the TiB_2 system to obviate the boron measurements. Since the measurements were always performed in the carbon resistance furnace and, therefore, in a carbon environment, B_4C was chosen as the additional phase. The compatibility of both B_4C and carbon with TiB_2 has previously been demonstrated by Williams (24). In addition, the thermodynamic properties of B_4C are fairly well known and, in any case make only a small contribution to the calculation of the free energy of TiB_2. The vaporization of $TiB_2(s)$ in the presence of $B_4C(s)$ can be written as follows:

$$TiB_{2\,(s)} + 1/2\ C_{(s)} = Ti_{(g)} + 1/2\ B_4C_{(s)} \qquad (18)$$

and ΔF^o for equation (18) is:

$$\Delta F^o\ (18) = -RT \ln P_{Ti} \qquad (19)$$

By using the known free energy of formation of B_4C, i.e., for,

$$4B_{(l)} + C_{(s)} = B_4C_{(s)} \qquad (20)$$

and the free energy of

$$TiB_{2(s)} = Ti_{(g)} + 2B_{(l)} \tag{21}$$

is given by

$$\Delta F^o_{(eq.\ 21)} = \Delta F^o_{(eq.\ 18)} - 1/2\ \Delta F^o_{(eq.\ 20)}$$

From this value and the known free energy of vaporization of Ti(l), the free energy of formation of $TiB_2(s)$ can be obtained. The experimental problem was then to measure the absorption of a titanium resonance line over the system $TiB_2(s)$ and $B_4C(s)$ and to obtain the vapor pressure of titanium over this system by the comparison of this absorption with that obtained over pure titanium metal.

1) Apparatus and Materials

The measurement of the atomic resonance line absorption on titanium has been described in detail before(10,23). The hollow cathode discharge source was identical to the one previously described and was used under identical operating conditions.

Two different kinds of absorption cells were used in this investigation. One, obtained from the National Carbon Company, was fabricated completely out of TiB_2 by hot pressing. It consisted of a TiB_2 cylinder 6" in length and approximately 1" o.d. End pieces were also made of TiB_2 and contained 3/16" openings. Wall thicknesses varied from 1/4" to 1/8". A typical cell shown in place in a carbon heater tube is presented in Figure 16. Boron nitride half rings were used to insulate the cell from the heater tube. At the temperature at which measurements were carried out, these BN rings would disintegrate after several heatings and had to be periodically replaced. Powdered B_4C (approximately 5-10 gms) was placed directly in the cell and the end pieces fitted into place. Actually, carbon end pieces were also used with no apparent differences in the results.

The second type of cell used consisted of a conventional graphite cylinder, 6" long having an o.d. of 1-1/4" and a wall thickness of 1/8". At the two ends of the cell, tight fitting graphite end pieces provided with an outside flange were slipped in and held in position with graphite pins. This cell was used in the measurement of the absorption of both the TiB_2 and the pure titanium metal. In the first case, a powdered sample of the same TiB_2 used in the fabrication of the TiB_2 cell was mixed with an equal amount of B_4C and loaded directly into the graphite cell. When the absorption over pure titanium metal was being studied, a tube of this metal, machined to precisely the same outer diameter as the internal diameter of the graphite cell, was slipped into the cell.

As mentioned above, the TiB_2 was obtained from the National Carbon Company and had the following chemical analysis (Ledoux and Company):

Titanium	66.82%	Manganese	0.001%
Boron	31.11%	Sodium	0.001%
Aluminum	0.08%	Columbium	0.03%
Calcium	0.001%	Nickel	0.01%
Cobalt	0.002%	Lead	<0.001%
Chromium	1.80%	Silicon	0.003%
Copper	0.001%	Vanadium	0.001%
Iron	0.09%	Zirconium	0.007%
Magnesium	<0.001%	Potassium	0.001%

All temperature measurements were made with a Pyro Micro Optical Pyrometer calibrated at the National Bureau of Standards. Temperature readings were made on black body holes located at the points A, B, C and D in Figure 16.

2. Procedure

The resonance line chosen for measuring the absorption due to titanium atoms was the 3371.45 Å line due to an $a\,^3F_4 - Y\,^3G_5$ resonance transition which promotes an electron from the 4s to 4p state. This is the same line that had been previously used in the TiC study and the procedure used here was identical to the procedure used in that investigation.

As mentioned before, absorption measurements on the 3371.45 Å Ti resonance line were performed in a pure TiB_2 cell with added B_4C and in a graphite cell containing powdered TiB_2 and B_4C. In addition, the absorption over pure titanium metal was reinvestigated with special emphasis placed on its pressure dependence. Pressure dependence was also carried out on the TiB_2-B_4C system in the graphite cell.

The method of obtaining the effective cell temperature was the same as was used in the TiC investigation, namely,

$$T_{\text{eff.}} = \frac{A + 2C - D + 2B}{4}$$

Helium was used as the inert gas atmosphere in all measurements.

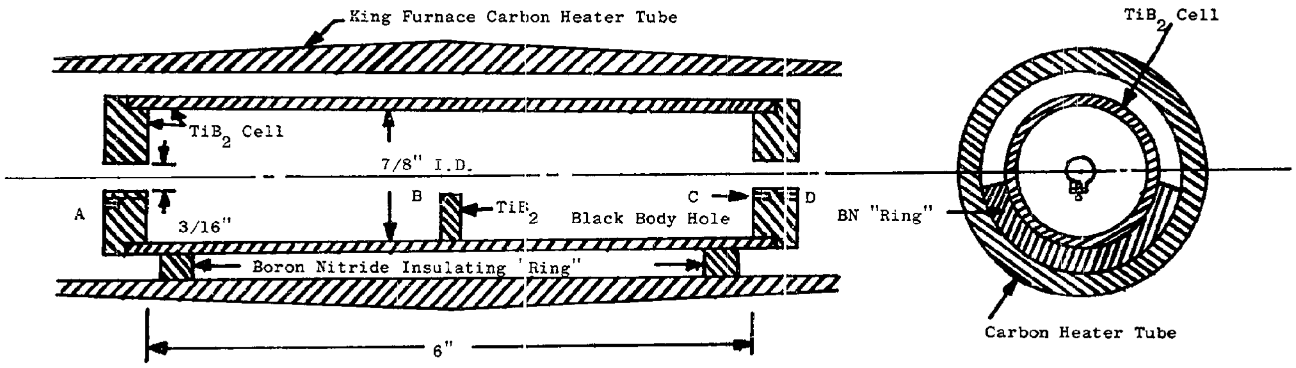

Figure 16. TiB$_2$ Equilibrium Cell

3. Results and Discussion

a) Experimental Data and Data Reduction

The results obtained on the absorption of 3371.45 Å Ti resonance line by TiB_2-B_4C and Ti metal are given in Tables 15 and 16.

The measured absorption data must be converted to metal atom pressure to produce the desired thermodynamic information. To do this, it is necessary to know the temperature and pressure variations of the absorption coefficient, and the fraction of the metal atoms which absorb the resonance line radiation. This has been thoroughly discussed before (10,23) for the case of titanium and details of the computation will not be given here except where changes have been made.

b) Pressure Dependence

In the previous work on the pressure dependence of the absorption of the titanium resonance line, only a limited pressure region was investigated. Furthermore, the pressure dependence was done over TiC rather than over the pure metal; and, therefore, it was more likely that non-equilibrium effects would be possible. In this investigation, the pressure dependence was carried out over pure titanium and the pressure region was quite extensive. The absorption, I/I_o, over the pure metal (from Table 16) was reduced to a common temperature (T_2 = 1658°K) by making use of the temperature variation of the vapor pressure of Ti and the following relationship

$$AP' = - T^{3/2} \ln I/I_o \qquad (17)$$

(This method has been previously given.) (21, 23)

Table 17 gives the average value of I/I_o at 1658°K as a function of pressure of helium.

These data are presented graphically in Figure 17. It is quite apparent that a substantial pressure dependence exists for the absorption of the Ti 3371.45 Å line. However, for the purpose of calculating the partial pressure of Ti over TiB_2, it is only necessary to compare the absorption of the resonance line at equal values of $p/T^{1/2}$ with the absorption over the pure metal system. It is felt that the pressure dependence measurements over the metal are of sufficient precision to enable one to calculate an optical collision cross section between titanium and helium. This is presently being computed using the method given by Zemansky (25). Several pressure dependence measurements of the absorption over TiB_2 have also been included (these are shown in Table 15). They will be used to estimate the degree of non-equilibrium in the TiB_2 system since the higher the inert gas pressure, the less diffusion and, consequently, the closer the system is to equilibrium.

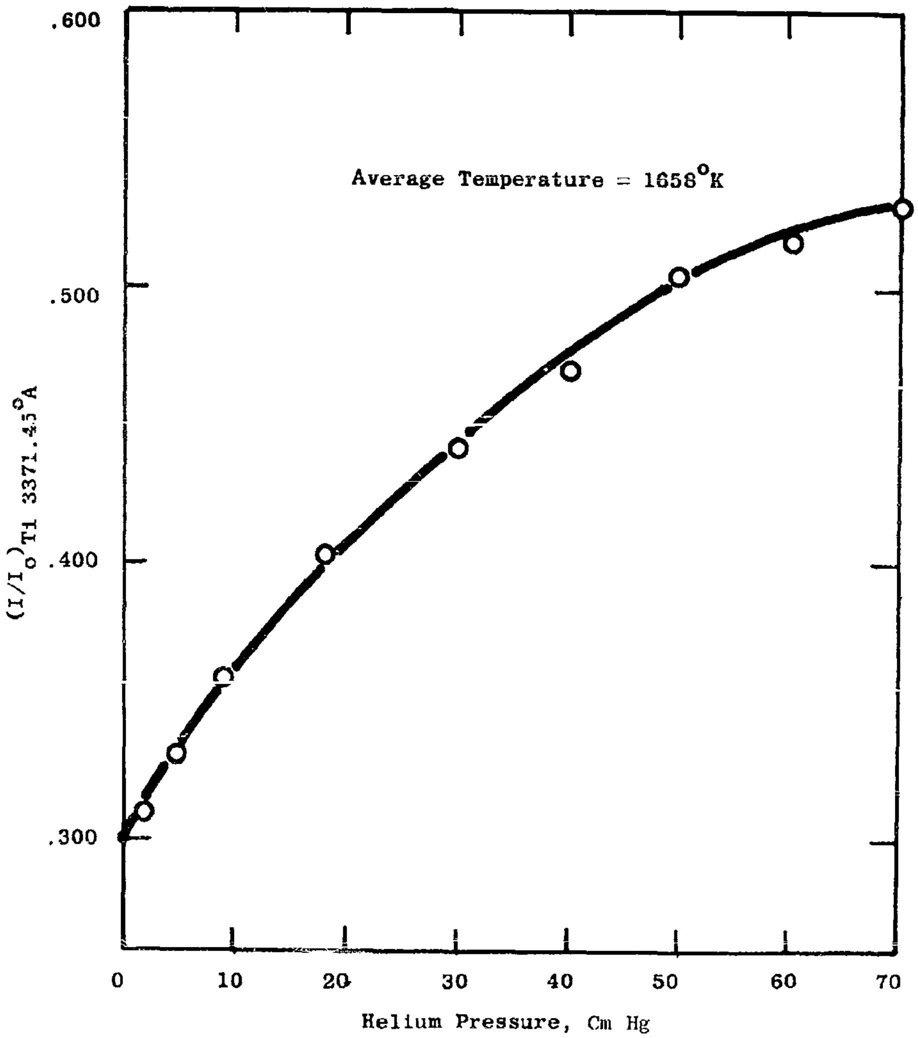

Figure 17. I/I_o Vs. Helium Pressure for Ti 3371.45 Å Line

Table 15

ABSORPTION DATA 3371.45Å Ti RESONANCE LINE BY VAPOR OVER TiB_2 - B_4C

System	Run No.	P_{He} cm.	Temperature °K					I/I_o
			A	B	C	D	$T_{eff.}$	
TiB_2 cell with added B_4C 1/4" wall	1	18.0	2449	2523	2473	2425	2504	0.524
	2	18.0	2441	2521	2471	2447	2496	0.542
	3	18.0	2449	2525	2470	2430	2502	0.517
	4	18.0	2442	2525	2466	2424	2500	0.521
	5	18.0	2444	2525	2472	2445	2498	0.497
TiB_2 cell with B_4C 1/8" wall carbon ends	1	22.0	2468	2526	2499	2473	2511	0.491
	2	22.0	2454	2515	2483	2426	2506	0.504
	3	22.0	2459	2512	2484	2440	2503	0.504
	4	22.0	2462	2510	2477	2433	2501	0.497
graphite cell with TiB_2 and B_4C	1	22.0	2420	2497	2459	2419	2478	0.500
	2	22.0	2411	2496	2459	2413	2477	0.529
	3	22.0	2403	2496	2455	2415	2472	0.533
	4	22.0	2411	2496	2462	2416	2478	0.519
	5	22.0	2413	2496	2457	2417	2476	0.520
	6	22.0	2412	2496	2457	2420	2474	0.530
	7	73.0	2413	2494	2461	2419	2476	0.580
	8	73.0	2410	2495	2460	2420	2475	0.594
	9	73.0	2424	2495	2466	2426	2480	0.562
	10	49.0	2418	2496	2460	2411	2480	0.539
	11	49.0	2415	2494	2460	2417	2476	0.564
	12	49.0	2421	2496	2460	2423	2476	0.553

Table 16

ABSORPTION DATA 3371.45Å Ti RESONANCE LINE
BY VAPOR OVER TITANIUM

System	Run No.	P_{He} cm.	Temperature °K					I/I_o
			A	B	C	D	$T_{eff.}$	
graphite cell with pure titanium metal	1	18.1	1654	1662	1655	1656	1658	.414
	2	18.1	1651	1660	1652	1655	1655	.412
	3	18.1	1649	1660	1652	1650	1656	.413
	4	18.1	1646	1659	1652	1647	1655	.436
	5	18.1	1648	1660	1652	1648	1656	.407
				Pressure Dependence				
	1	18.0	1648	1662	1659	1653	1659	.402
	2	9.0	1633	1656	1650	1642	1650	.395
	3	9.0	1636	1655	1650	1641	1651	.427
	4	70.1	1641	1661	1660	1658	1656	.514
	5	70.1	1652	1662	1660	1658	1659	.525
	6	60.1	1651	1662	1660	1656	1660	.508
	7	60.1	1647	1659	1657	1651	1656	.526
	8	50.1	1647	1659	1656	1653	1656	.509
	9	49.9	1646	1660	1657	1651	1657	.519
	10	40.0	1647	1660	1658	1651	1658	.466
	11	40.0	1648	1661	1658	1655	1658	.439
	12	30.0	1645	1659	1658	1649	1658	.442
	13	30.0	1643	1658	1658	1649	1657	.451
	14	70.0	1650	1661	1659	1656	1658	.529
	15	40.0	1642	1659	1658	1652	1656	.471
	16	17.9	1646	1660	1659	1650	1659	.394
	17	9.0	1641	1661	1656	1648	1657	.354
	18	9.0	1641	1660	1656	1646	1657	.369
	19	5.0	1636	1661	1654	1640	1656	.339
	20	40.0	1645	1658	1657	1648	1657	.511
	21	40.0	1647	1660	1657	1652	1657	.491
	22	5.0	1639	1662	1656	1646	1657	.341
	23	2.0	1631	1662	1653	1641	1655	.306
	24	2.0	1635	1661	1655	1641	1656	.337
	25	2.0	1634	1660	1656	1642	1656	.357

Table 17

PRESSURE DEPENDENCE OF THE ABSORPTION OF Ti 3371.45 Å RESONANCE LINE OVER TITANIUM

P_{He} cm.	I/I_o
2.0	.310
5.0	.330
9.0	.359
18.0	.403
30.0	.442
40.0	.470
50.0	.504
60.0	.517
70.0	.530

c) Data Reduction

As was mentioned earlier, the absorption, I/I_o, can be related to the relative partial pressure of titanium by the following relationship:

$$AP' = -T^{3/2} \ln I/I_o \qquad (17)$$

which is, to a good degree of approximation, independent of inert gas pressure as long as P_{Helium} $T^{-1/2}$ is held constant. The values of AP' obtained in this way are then reduced to a common temperature (in the usual fashion) so that these relative pressures can be averaged and compared. The integrated form of the Clapeyron-Clausius equation is used for this calculation:

$$\log \frac{AP_1'}{AP_2'} = \frac{\Delta H\ (T_1 - T_2)}{2.303\ R\ T_1\ T_2} \qquad (22)$$

The values of Δ H and the common reference temperatures T_2 for the two vaporization reactions are:

	ΔH	T_2
Ti	108.86	1658
TiB_2	161*	2500
		2475 (Graphite Cell)

Two reference temperatures are given for TiB_2 depending on which cell was used. The heat of vaporization of TiB_2

---

*Estimated value

(in the presence of B_4C) was estimated from data in the JANAF tables and from Williams (24). In view of the shortness of the extrapolation, any uncertainty in the value of ΔH does not lead to errors worth mentioning. The average values of AP' reduced to these common temperatures and the rms. deviations are presented in Table 18.

Table 18

RELATIVE TITANIUM PARTIAL PRESSURES - ABSORBER ATOMS

Material	Helium Pressure cm.	AP' ave. x 10^{-4}	T_2 °K	rms. dev. x 10^{-4}	rms. dev. %
TiB_2 cell with B_4C	20.0	3.54	2500	0.16	4.5
graphite	22.0	3.44	2475	0.08	2.3
cell with	49.0	3.08	2475	0.05	1.6
TiB_2 and B_4C	73.0	2.84	2475	0.03	1.8
graphite	18.0	2.66	1658	0.06	2.3
cell with	40.0	2.08	1658	0.14	6.3
Ti metal	60.0	1.93	1658	0.06	3.1

Finally, AP' must be converted to AP where P is the total pressure of titanium rather than the partial pressure of atoms in the particular state capable of absorbing the radiation from the source. This is done in the usual manner by evaluating:

$$N_1\ (T) = \frac{(2J_1 + 1)\ e^{-E_1/KT}}{\sum_i (2J_i + 1)\ e^{-E_i/KT}} = \frac{AP'}{AP} \qquad (23)$$

Lastly, by again using the Clapeyron-Clausius equation for the pure titanium metal, the temperatures at which the metal (at the same $PT^{-1/2}$) has the same AP value as the TiB_2 can be calculated. These results appear in Table 19.

The results in Table 19 are the direct experimental information obtained by these experiments. Stated in another way, it can be concluded that the vapor pressure of Ti(g) in equilibrium with TiB_2 in the presence of B_4C at temperature T_1 is equal to the vapor pressure of Ti(g) over pure titanium metal at temperature T_2.

Table 19

RELATIVE TITANIUM ATOM PRESSURES

System	P_{Helium} cm.	T_1 °K TiB_2	T_2 °K Ti (s) for same AP	AP ave. x 10^{-4}
TiB_2 Cell with B_4C	20.0	2500	1670	9.31
graphite cell with TiB_2 and B_4C	22.0	2475	1669	9.04
	49.0	2475	1673	8.11
	73.0	2475	1676	7.50

From the statement of results (Table 19), and the known vapor pressures of titanium as given by Stull and Sinke (13), the vapor pressure above the TiB_2-B_4C system can be obtained. These are given in Table 20.

Table 20

VAPOR PRESSURE OF Ti(g) OVER TiB_2-B_4C

System	P_{Helium} cm.	Temperature °K	log P_{Ti}	$P_{atm.}$
TiB_2 Cell with B_4C	20.0	2500	-7.262	5.47×10^{-8}
graphite cell with TiB_2 and B_4C	22.0	2475	-7.270	5.37×10^{-8}
	49.0	2475	-7.236	5.81×10^{-8}
	73.0	2475	-7.211	6.15×10^{-8}

It is obvious from Table 20 that the resulting vapor pressures of titanium over TiB_2-B_4C are (1) influenced by the type of absorption cell and (2) apparently a slight function of the inert gas pressure. It is felt that these effects are indeed real and not due to lack of precision of the method. The slight variation of the vapor pressure with inert gas pressure is not surprising since, as was previously pointed out, in a system involving TiB_2, thorough equilibrium in the absorption cell may not be achieved. Indeed, it is expected that, since the rate of diffusion of titanium vapor from the absorption cell should be reduced at higher inert gas pressures, the apparent vapor pressure of titanium should increase with increasing helium pressure. This is what is observed and it is felt that the highest measured pressure is more realistic of equilibrium conditions.

The apparent discrepancy between the results using the TiB_2 cell and the graphite cell can be resolved when it is remembered that the TiB_2 cell was supported in the carbon tube furnace with boron nitride rings. At the temperature of the experiment, these rings decompose to boron and hence the partial pressure of boron in the system is greater than that expected from B_4C. Consequently, if equilibrium is maintained, the corresponding titanium vapor pressure must be lowered or the temperature of the TiB_2 raised so that the observed Ti vapor pressure remains approximately the same. Indeed, it is seen from Table 20 that the temperature of the TiB_2 cell is 25°K higher than that of the graphite cell for approximately the same vapor pressure of titanium. To calculate thermodynamic properties from the TiB_2 cell measurement, it is necessary to estimate this enhancement in boron pressure. Since this is somewhat arbitrary, the results of the graphite absorption cell measurements will be used to calculate these thermodynamic properties. It should be pointed out that, even if this enhancement is not taken into account, the resulting calculated free energy of formation of TiB_2 agrees within 2.5 kcal/mole with results obtained from the graphite cell measurements.

The free energy for the reaction

$$TiB_2(s) + 1/2\ C(s) = Ti(g) + 1/2\ B_4C(s) \qquad (18)$$

is given as:

$$\Delta F^o = -RT \ln P_{Ti} \qquad (19)$$

and, therefore, at 2475°K, using the measured vapor pressures of titanium has the values

$$\Delta F^o_{2475} = 81.67 \text{ kcal/mole at 73 cm He}$$

$$= 81.95 \text{ kcal/mole at 49 cm He}$$

$$= 82.34 \text{ kcal/mole at 22 cm He}$$

Therefore, since the free energy change for

$$1/2\ B_4C(s) = 2B(l) + 1/2\ C(s) \qquad (24)$$

as given by the JANAF tables at 2475°K, is

$$\Delta F^o_{2475} = 2.89 \text{ kcal} \qquad (25)$$

the free energy change for

$$Ti(g) + 2\ B(l) = TiB_2(s) \qquad (26)$$

is

$$\Delta F^o_{2475} = -84.56 \text{ kcal/mole at 73 cm He}$$
$$= -84.84 \text{ kcal/mole at 49 cm He}$$
$$= -85.23 \text{ kcal/mole at 22 cm He}$$

Using the known vapor pressure of Ti(l) at 2475°K as given by reference(13), the free energy of

$$Ti(l) = Ti\ (g) \qquad (27)$$

is

$$\Delta F^o_{2475} = 31.23 \text{ kcal/mole}$$

When this is combined with the above, the free energy of formation of TiB_2 from B(l) and Ti(l) becomes:

$$\Delta F^o_{f\ 2475^o} = -53.34 \text{ kcal/mole at 73 cm He}$$
$$= -53.62 \text{ kcal/mole at 49 cm He}$$
$$= -54.01 \text{ kcal/mole at 22 cm He}$$

As mentioned above, more reliability should be given to the value obtained at 73 cm of helium.

4. Conclusions

Therefore, based on the above results and their evaluation, it is concluded that free energy of formation of $TiB_2(s)$ at 2475° is equal to - 53.34 kcal/mole. It is estimated, as in the previous TiC work, that this value is accurate to ± .5 kcal/mole.

Since no complete heat capacity data exist for TiB_2 at this time, the calculation of the heat of formation must be postponed until such data become available. However, it is expected that the heat of formation of $TiB_2(s)$ should be approximately the same as $\Delta F^o_{formation}$, namely, approximately - 54 kcal/mole.

F. References

1. Kriege, O.H., Los Alamos Scientific Laboratory Report LA-2306 (March 1959).

2. *1960 Book of ASTM Methods for Chemical Analysis of Metals*, Amer. Soc. for Testing Materials, Philadelphia (1961). p. 503.

3. Veleckis, E., Rosen, C.L., and Feder, H.M., *Journal Phys. Chem 65, 2127* (1961).

4a. Smagina, E.I., Kutsev, V.S., and Ormont, B.F., *Doklady Akad. Nauk. SSSR 115*, 354 (1957).

4b. Smagina, E.I., Kutsev, V.S., and Ormont, B.F., *Zhur. Fiz. Khim 34* 2328 (1960).

5. Domagala, R.F., et al., Trans. AIME *206*, 98 (1956).

6. Hoch, M., Dingledy, D.P., and Johnston, H.L., *J. Am. Chem. Soc. 77,* 304 (1955).

7. Brewer, L., et. al., *Chemistry and Metallurgy of Miscellaneous Materials: Thermodynamics*, (L.L. Quill, Ed.) McGraw-Hill New York (1950).

8. Searcy, A. W., *Symposium on High Temperature Technology (Asilomar)*, October 6, 1959.

9. Coffman, J. A., et al., *WADD Technical Report 60-646*, Part 1 (Feb., 1961).

10. Coffman, J.A., et al., *WADD Technical Report 60-646* Part II

11. Thomas,D. E., and Hayes E.T., (Ed), *The Metallurgy of Hafnium,* U.S. Government Printing Office, Washington (1960).

12. Holden, R.B., et. al., *J. Am. Chem. Soc. 70*, 3897 (1948).

13. Stull,D.R., and Sinke G.C., *Thermodynamic Properties of the Elements*, American Chemical Society, Washington D.C. (1956) Advanced in Chemistry Series #18.

14. Fieldhouse, I.B., and Lang, J.I., *WADD Technical Report 60-904* (July 1961).

15. Shomate, C.H., *J. Am. Chem. Soc. 66,* 928 (1944).

16. *USBM-U-863 Quarterly Metallurgical Progress Report #12*, Bur. Mines Albany Met. Res. Center, Oreg., (Sept. 30, 1961).

17. Deardorff, D.K., and Kato, H., USBM-U-426, (April 8, 1958).

18. Deardorff, D.K., and Hayes, E.T., J. Metals 8, 508, (1956).

19. Krikorian, O.H., "High Temperature Studies" UCRL-2888 (April, 1955).

20. Linevsky, M.J., J. Chem. Phys. 34, 587-590 (1961).

21. Vidale, G.L., TIS R60SD333, G.E. Co. (1960).

22. Vidale, G.L., TIS R60SD331, G.E. Co. (1960).

23. Vidale, G.L., TIS R61SD147, G.E. Co. (1961).

24. Williams, S.W., J. Phys. Chem. 65, 2213-16 (1961).

25. Zemansky, M.W., Phys. Rev. 36, 219 (1930).

26. Mitchell and Zemansky, Resonance Radiation and Excited Atoms, Cambridge Press, (1934).

III SPECTRAL EMISSIVITIES OF REFRACTORY MATERIALS

A. Background

1. Previous Work

This section deals with the experimental determination of radiation properties of conducting refractory materials at high temperatures. Earlier annual reports (1, 2) described the development and refinement of techniques for measuring normal spectral emissivity over a sufficiently wide wavelength bandwidth to permit computation of normal total emissivities up to 3500°K. Normal spectral and normal total emissivities of various refractory materials, selected on the basis of their potential application in the design of rocket nozzles were also determined and reported.

For example, the first annual report (1)* described normal spectral emissivity measurements made at selected temperatures on materials listed in Table 21. The values shown are total normal emissivities calculated from spectral data.

TABLE 21

Normal Total Emissivities - Selected Materials

Material	Temperature °K	Normal Total Emissivity
Tungsten	1800	.22
	2000	.24
Tantalum Carbide	1800	.22
	2200	.26
	2600	.30
	3000	.33
Zirconium Carbide	2000	.43
	2400	.45

---

[*] Page 162

In the second annual report, (2) normal spectral emissivity measurements on the following materials over a wavelength range of 0.4 microns to 5 microns were summarized:

1. Molybdenum + ½% titanium with Chromalloy-W-2 coating.
2. Siliconized ATJ Graphite
3. Tantalum
4. Molybdenum
5. Tungsten
6. Tungsten Carbide
7. Zirconium

Given in Table 22 are values of normal total emissivity, at various temperatures, for several of these materials.

TABLE 22

Normal Total Emissivity - Other Selected Materials

Material	Temperature °K	Normal Total Emissivity
Tantalum	1800	.18
	2200	.23
	2600	.28
Molybdenum	1800	.16
	2200	.20
	2600	.25
Tungsten Carbide W_2C	1600	.26
	1800	.31
	2000	.38
	2200	.40
Tungsten Carbide WC	1400	.17
	1600	.21
	1800	.26

The work was continued during the past year and the results are herein summarized.

2. General Considerations

To review briefly, the total power that a unit surface of a black body radiates is expressed by Stefan's law — $J_{bb}(T) = \sigma T^4$ — where σ is the Stefan-Boltzmann constant and T the absolute temperature. For a unit surface of a material that is not a black body the power it radiates is modified by the emittance of that surface and when factored into Stefan's law at temperature T the expression becomes:

$$J(T) = \varepsilon_{(T)}\, \sigma\, (T^4 - T_s^4) \qquad (28)$$

where $\varepsilon_{(T)}$ is total hemispherical emissivity, T is surface temperature, and T_s is the temperature of the surroundings or heat sink into which the material is radiating.

In the direct method of emissivity measurement as applied here, the ratio of the energy radiated from the surface of the material at a known temperature is compared to that radiated from an equal area of a black body at the same temperature. The reference black body used was a cavity drilled directly into the specimen.

From normal spectral emissivity values measured at a given temperature, combined with the black body distribution of radiation at that temperature, normal total emissivities can be computed.

Table 23 tabulates the black body functions required for such calculation. The data were obtained from the General Electric "Radiation Calculator" slide rule (3). It is estimated that the calculation introduces no more than 5% error in the value of total emissivity. To obtain normal total emissivity for a particular substance at a given temperature, one simply reads the spectral emissivity from the measured data and multiplies it by the fraction of energy radiated by a black body corresponding to that wavelength interval and temperature. The total emissivity is simply the sum of the products of "energy fraction" and spectral emissivity and can be expressed as follows:

$$\varepsilon_{nt(T)} = \Sigma\, (\varepsilon_{nd\,\lambda(T)})\ '\ (I_{bb\ d\lambda(T)}) \qquad (29)$$

where $\varepsilon_{nt(T)}$ is normal total emissivity at temperature T, $\varepsilon_{nd\lambda(T)}$ is normal spectral emissivity at temperature T, $I_{bb\ d\lambda\ (T)}$ is the fraction of energy radiated from a black body in the wavelength interval dλ at temperature T.

B. Experimental

1. Apparatus

Figure 18 is a view of the emissometer developed and discussed earlier.(1) Figure 19 is a detailed view of the source unit specimen chamber

Table 23

CONVERSION OF SPECTRAL EMISS VITY TO TOTAL EMISSIVITY

Mean Wavelength[(1)] or Wavelength Interval (in microns)	Fraction of Total nergy at Effective Mean Wavelength								
	1400^{o}	1600^{o}	1800^{o}	200^{o}	2200^{o}	2400^{o}	2600^{o}	2800^{o}	3000^{o}K
0.5$^{(2)}$	-	-	-	-	-	-	.01	.01	.01
0.6$^{(2)}$	-	-	-	-	.006	.01	.01	.02	.03
0.7$^{(2)}$	-	-	-	.01	.014	.02	.025	.03	.04
0.8$^{(2)}$	.001	.004	.01	.01	.02	.03	.035	.05	.06
0.9$^{(2)}$	.002	.006	.01	.02	.03	.04	.05	.06	.07
1.0	.007	.01	.02	.03	.03	.04	.06	.06.	.06
1.1	.02	.04	.06	.07	.09	.11	.11	.13	.13
1.3	.03	.05	.07	.07	.10	.09	.12	.11	.12
1.5	.05	.07	.08	.09	.10	.09	.10	.09	.09
1.7	.06	.07	.08	.09	.08	.09	.08	.08	.07
1.9	.035	.08	.08	.08	.08	.07	.06	.06	.06
2.2	.155	.13	.13	.12	.12	.11	.10	.09	.08
2.6	.11	.10	.10	.1	.08	.07	.07	.06	.05
3.0	.10	.09	.08	.0	.06	.05	.04	.04	.04
3.4	.07	.07	.06	.0	.04	.04	.03	.03	.02
3.8	.06	.05	.04	.0	.04	.03	.02	.04	.02
4.5	.11	.09	.07	.0	.04	.04	.04	.02	.02
Above$_{5.0}$$^{(3)}$	.19	.14	.11	.0	.07	.05	.04	.04	.03
All Wavelengths	1.00	1.00	1.00	1.0	1.00	1.00	1.00	1.00	1.00

NOTE: All data taken from "Radiation Cal ulator".

(1) Mean wavelengths are not spaced equally ut rather are spaced to adequately reflect rate of emissivity variation with wavel ngth for many opaque solid materials.

(2) Shortest wavelength used is a function f temperature and includes all radiation below that wavelength.

(3) Spectral emissivity varies slowly at th long wavelength end of the spectrum where only a small fraction of the energy remains- articularly at the higher temperatures.

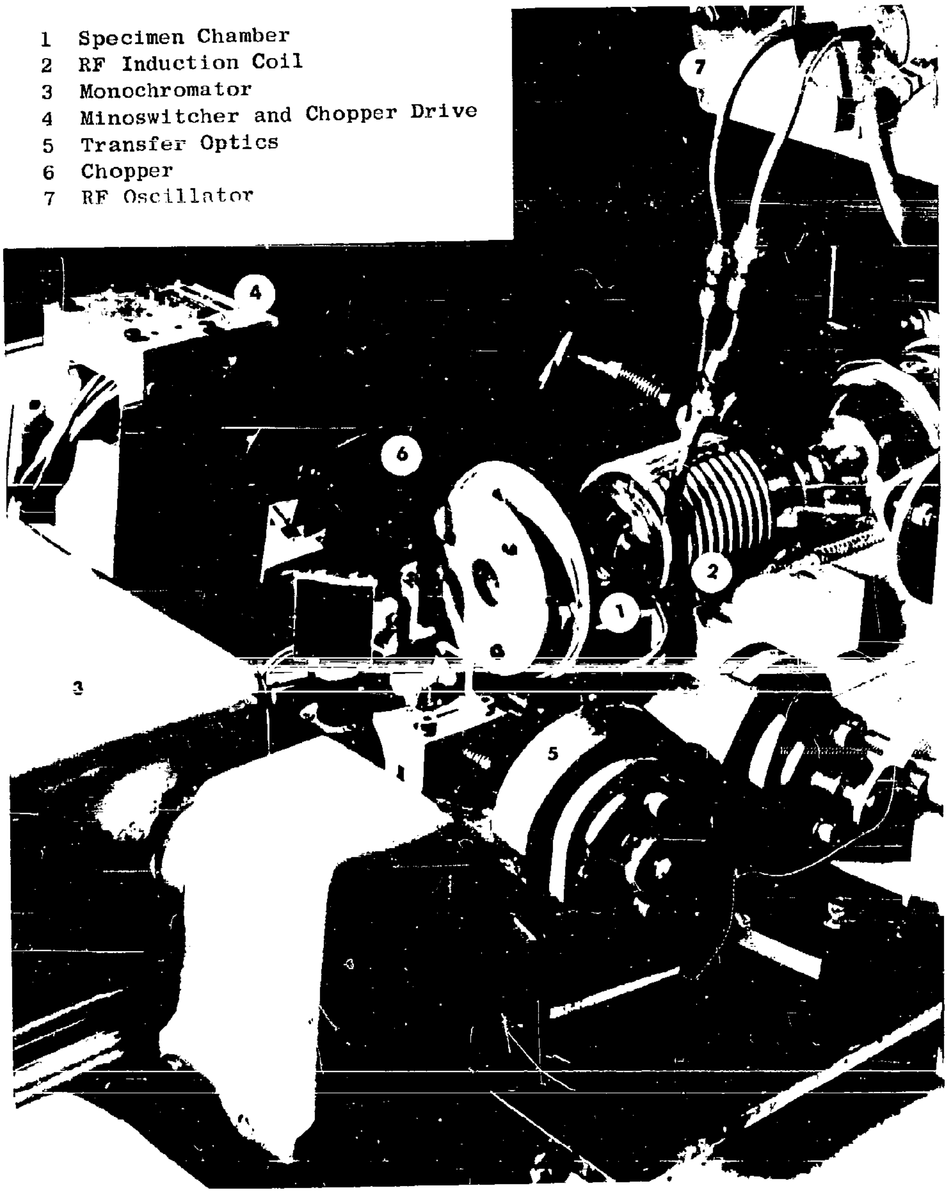

1 Specimen Chamber
2 RF Induction Coil
3 Monochromator
4 Minoswitcher and Chopper Drive
5 Transfer Optics
6 Chopper
7 RF Oscillator

Figure 18. Emissometer

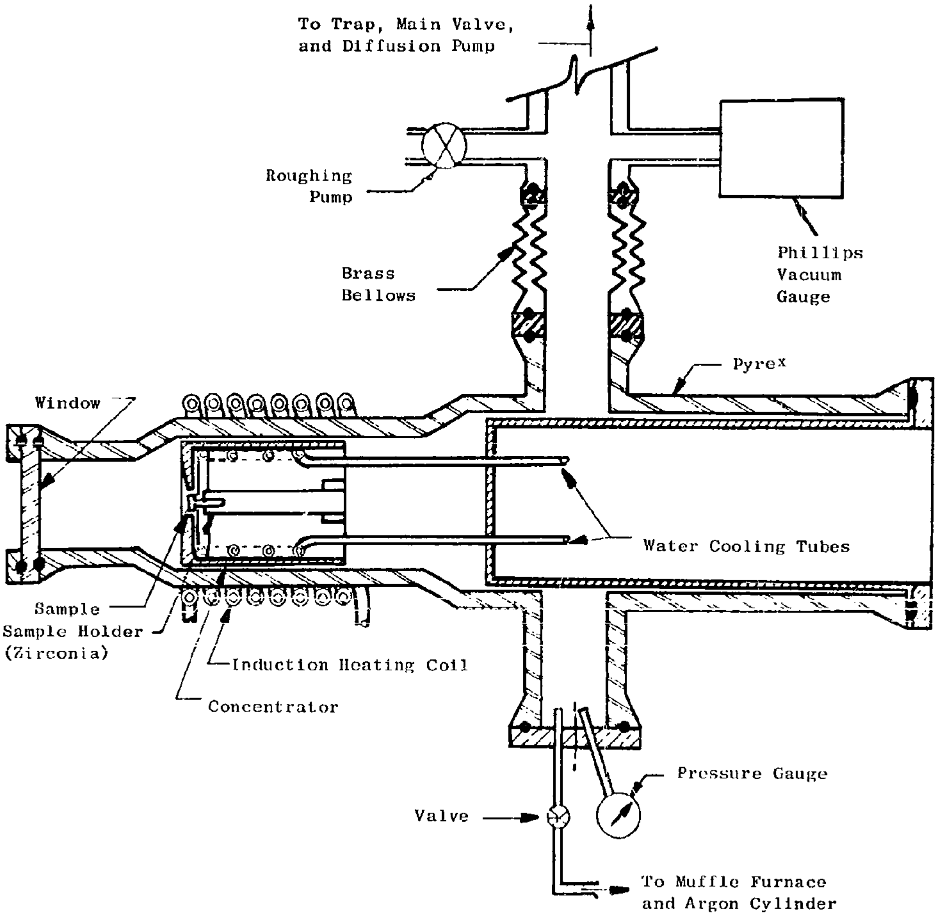

INDUCTION FURNACE EMISSOMETER
- SOURCE UNIT and SPECIMEN CHAMBER

Figure 19. Source Unit - Specimen Chamber

which provides a means of mounting the material sample and heating it in vacuum, or purified inert gas atmosphere. The test sample is heated by means of concentrating RF energy coupled from the induction heating coil into a water cooled tank transformer which in turn concentrates the RF energy at the surface of the specimen to produce a uniform constant high temperature. Energy radiated from the specimen passes through the air cooled calcium fluoride window of the chamber into the transfer optics shown in Figure 20. This optical system produces a sharp black body and surface image on the spectrometer slit and by means of the oscillating mirror alternately images radiated energy from the specimen surface and its black body reference cavity. This mirror oscillates at a frequency of 7 cps and the chopper alternates the radiant signal at 14 cps producing a signal suitable for amplification in a standard Perkin-Elmer amplifier.

2. Specimen Preparation And Design

Specimens of all materials employed in this study were procured from the Carborundum Company. They were prepared from finely divided powders (particle size less than 1 micron) of the appropriate compound, by hot pressing in an oversized graphite mold at temperatures in excess of 2000°C. After sintering,the specimens were ground to size to remove traces of diffused carbon and any carbides that may form on the surface. A hole 0.02 inches in diameter and 0.08 inches deep was ultrasonically bored in the center of one face and serves as the black body reference cavity. The hole diameter is about twice the diameter of the slit in the emissometer. In making emissivity measurements, the radiancy of this reference black body cavity was compared to that of the adjacent surface. Because of the proximity of the surface and black body there is good assurance that both are at the same temperature. Figure 21 shows a drawing of the specimen.

3. Specimen Characterization

It is well known that the value of spectral emissivity is intimately associated with the chemical and physical properties of a given material. Worthing (4) for example, in his definition of emissivity, limits its application to polished surfaces. Because experimental results depend in a large measure on this and other specimen properties at the time its emissivity is being measured, a substantial amount of study was devoted to systematic characterization of the various specimen materials. In application it was found that the characterizing parameters did not, in all cases, admit of rigorous interpretation because of other factors that influenced their validity.

These factors are a direct result of the high temperatures at which measurements were made. In some instances their dynamic nature could be observed when viewing the specimen through the optical pyrometer during measurement of specimen temperature. Slow changes were observed in surface texture from polished to an etched or matt structure. Formation of micropores that gave the appearance of a multiplicity

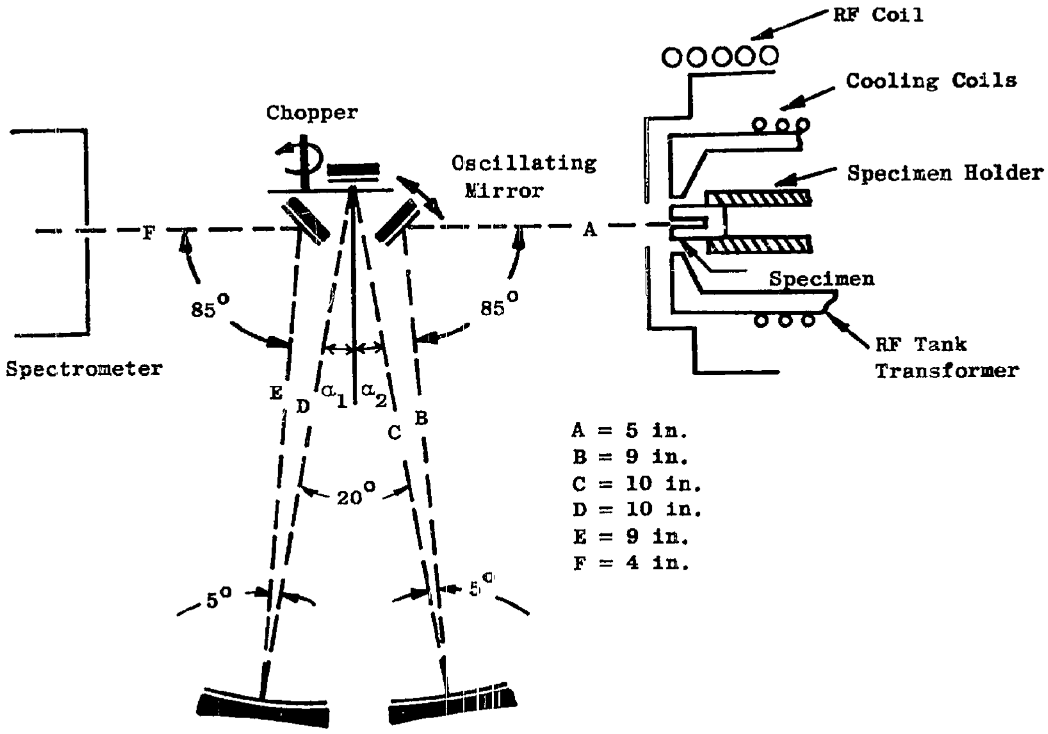

Figure 20. Transfer Optics for Measuring Normal Emittance(Showing Optical Path of Radiation from Specimen to Spectrometer)

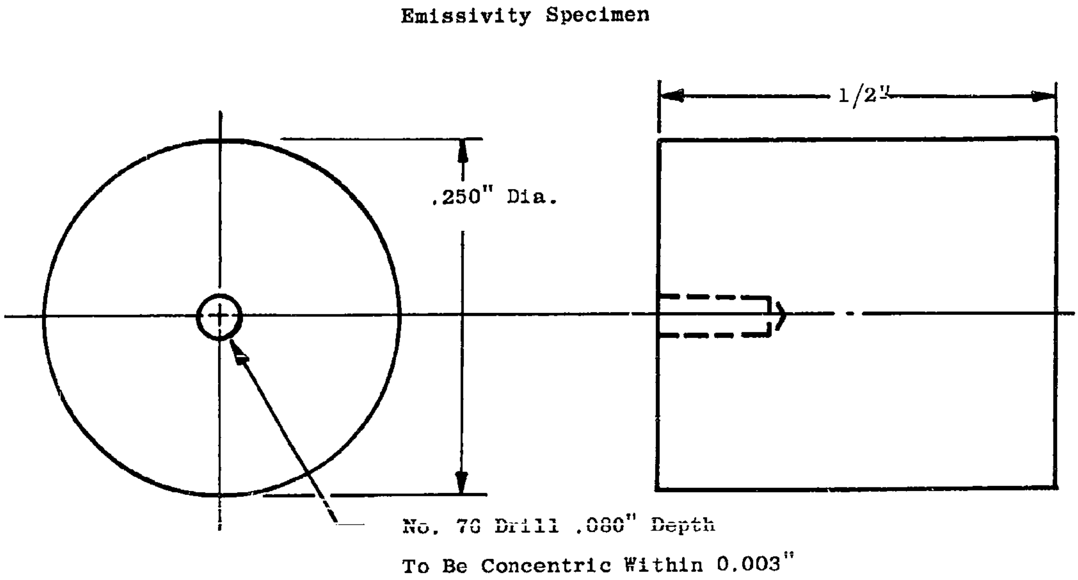

Figure 21. Emissivity Specimen

of microscopic black body cavities, and apparent changes in surface grain size were also observed. Other changes that are believed to occur while the specimen is standing at high temperature are those involving surface composition, bulk densification, evaporation, interaction of the specimen with its holder and reaction with trace contaminents in the specimen chamber.

To differentiate between perturbations in specimen emissivity and its true variation with wavelength and temperature, the following characterizing steps were carried out on each material : (1) Chemical composition was first established by running wet chemical analysis to determine major elemental components and spectro-chemical analysis to determine the trace elements present in the specimen. In addition ,those elements looked for and not found were recorded. (2) Each specimen was then polished, etched, and photomicrographed to determine grain size, boundary distribution, pore distribution and micro inclusion content. Microscope optics were standardized as to objectives, oculars, bellows setting, angle of polarized light, and light intensity. Filters were not used. In addition, an effort was made to maintain standard photographic procedures. (3) Next,the etched specimen surface was replicated and electron micrographs of crystalline structure recorded. (4) The surface was again polished and slow scan x-ray diffraction patterns run. In this step,"d" spacings were measured, line intensities were recorded and related to inclusion concentrations, and Miller indices were measured. These x-ray observations were carried out after polishing to establish whether or not the polishing operation had caused the surface to possess an amorphous structure indicative of multiple layers of free atoms on the surface. It was felt that the presence of such layers would be unstable and would undergo evaporation and crystallization during emissivity measurements. Therefore, when this was observed, the specimens were repolished in a manner that removes the amorphous layer. (5) Specimen weight and density measurements were then made for the purpose of comparing possible changes in these properties during emissivity measurement. In several cases, weight and density changes could not be entirely attributed to evaporation, densification and modifications in composition because there occured an interchange of material due to interaction of the specimen and its ZrO_2 holder. (6) Normal spectral emissivity measurements were then made over a temperature range understood to be compatible with thermal stability of the specimen. As a further measure of relating changes in emissivity induced by thermal and/or environmental conditions,a steady state low temperature was selected at which emissivity determinations were made. These determinations then served as a benchmark against which to measure changes in emissivity as a result of making measurements at higher temperatures. (7) Following emissivity measurements ,the specimens were again weighed, density measurements made, photomicrographs, x-ray diffraction and electron microscope studies run and compared with previous observations.

4. Measurement Of Normal Spectral Emissivity

In comparing the spectral radiation of different materials it is the accepted practice to express this property in terms of spectral emissivity at the desired temperature. Normal spectral emissivity ($\epsilon_{n\lambda}$) can be defined as the ratio of energy radiated perpendicularly from a unit area surface of a material to that radiated perpendicularly from the same area of a black body (a perfect radiator having an emissivity of 1) at the same temperature and wave length interval, and is expressed as follows:

$$\epsilon_{n\lambda(T)} = \frac{I_{\lambda(T)}}{I_{o\lambda(T)}} \tag{30}$$

where $I_{\lambda(T)}$ is the energy radiated from the surface of the specimen at temperature T and $I_{o\lambda(T)}$ is the energy radiated from the black body reference cavity.

In this work, normal spectral emissivity measurements were made over a wavelength bandwidth, starting at 0.4 micron in the visible out to 5 microns in the infrared, for the following compounds:

1. Niobium Diboride - NbB_2
2. Zirconium Diboride - ZrB_2
3. Titanium Diboride - TiB_2
4. Zirconium Nitride - ZrN
5. Hafnium Nitride - HfN
6. Tantalum Nitride - TaN

The various temperatures at which measurements were made ranged from 1500°K to 3000°K.

In making emissivity measurements the following procedures were carried out: The specimen chamber was first pumped to pressures below 5×10^{-5} Torr and by manipulating the appropriate valves the system was checked for leaks. Following this the specimen was heated to about 700°C to outgas it and liberate residual moisture from associated surfaces. The chamber was then flushed several times with prepurified argon and finally filled with argon to a pressure of about 1.5 to 2 atmospheres.

The specimen temperature, as measured by means of a calibrated optical pyrometer, was then raised to the intended temperature at which emissivity values were measured. Both black body and surface temperatures were measured to within an accuracy of 5° and again checked at the end of each emissivity run. Observed pyrometer temperatures were corrected for absorption of the calcium fluoride infrared transmitting window in the specimen chamber and incomplete reflections from the front surface mirror. Figure 22 is a plot of applied temperature corrections as a function of specimen pyrometer temperature.

Calibration of the emissometer was carried out before each run. When the specimen had attained a stable temperature it was optically aligned and brought into perfect focus. With all electronics warmed up and stable, the monochrometer slit opening was brought dynamically to a position to read emissivity at the shortest wavelength that the particular photomultiplier detector can sense; namely, 0.4μ. The radiation from the specimen black body cavity was then scanned under conditions such that the recorder readout measures energy from the black body unattenuated by the vectoral summation of plain surface emittance. If ,under these conditions, the recorder readout is not 100%, the appropriate adjustments are made. All radiation is then cut off from the slit entrance of the monochrometer by mechanically attaching a specially prepared black surface to the chopper. The recorder readout is then adjusted to zero.

The monochrometer is also periodically checked by calibrating it against known emission and absorption bands and plotting instrument drum readings against wavelength.

Additional periodic checks were made by inserting specific spectral cut on and cut-off filters in front of the emissometer slit and relating emissometer drum readings in terms of wavelength at which radiant energy was cut on and off. Also when specimen surface brightness and black body cavity temperatures are substituted in the following relationship

$$\frac{1}{T_s} - \frac{1}{T_{bb}} = \left(\frac{.65}{C_2}\right) (\ln \epsilon) \qquad (31)$$

where C_2, a constant, equals 1.4388×10^4 cm-°K, T_s is the surface brightness temperature, T_{bb} the blackbody temperature, the emissivity ϵ, at the pyrometer wavelength can be computed and compared with emissometer readings at the same wavelength. Still another check is made periodically by measuring the emissivity of a "standard" single crystal tungsten specimen.

C. Results and Discussion

1. Niobium Diboride - NbB_2

This compound is a crystalline material possessing a hexagonal structure and an x-ray theoretical density of 7.21 g/cm^3 (5). Its hardness on the Mohs scale is greater than 8 and according to Glaser(6), dissociation does not take place at temperatures below 2900°C.

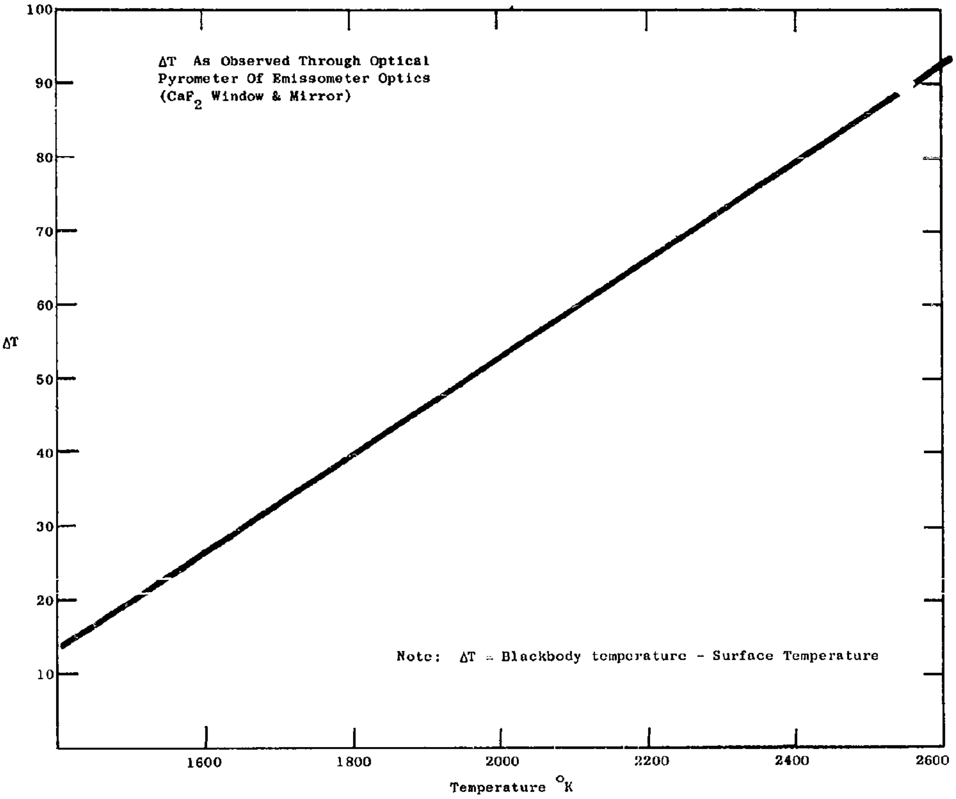

Figure 22. Temperature Correction Chart

a. Chemical Analysis - NbB_2

Table 24 gives the results of chemical analysis of the NbB_2 specimen on which emissivity measurements were made.

Table 24

CHEMICAL ANALYSIS - NbB_2

Niobium		79.07%	Molybdenum	ND	10 PPM
Boron		19.09%	Sodium		10 PPM
Silver	ND	5 PPM	Nickel		150 PPM
Aluminum		70 PPM	Lead	ND	10 PPM
Arsenic	ND	100 PPM	Antimony	ND	50 PPM
Barium	ND	10 PPM	Silicon		30 PPM
Beryllium	ND	10 PPM	Tin	ND	10 PPM
Bismuth	ND	10 PPM	Strontium	ND	10 PPM
Calcium		100 PPM	Tantalum		700 PPM
Cadmium	ND	10 PPM	Tellurium	ND	100 PPM
Cobalt	ND	10 PPM	Thallium	ND	10 PPM
Chromium		150 PPM	Titanium		50 PPM
Copper	ND	10 PPM	Vanadium		30 PPM
Iron		2600 PPM	Tungsten	ND	500 PPM
Germanium	ND	10 PPM	Zinc	ND	50 PPM
Hafnium	ND	100 PPM	Zirconium	ND	50 PPM
Indium	ND	10 PPM	Potassium		10 PPM
Lithium	ND	10 PPM			
Magnesium	ND	5 PPM			
Manganese		30 PPM			

NOTE: ND = not detected, less than
PPM = parts per million

The theoretical composition of NbB_2 is 81.11% niobium and 18.89% boron. Actual specimen composition is close to theoretical. being 79.07% and 19.09% respectively. The presence of .26% iron is believed to have very little effect on emissivity at high temperatures. Iron possesses a vapor pressure of 10^{-6} Torr at 1273°K and most likely evaporates from the surface at temperatures in excess of 1600°K. In fact all trace elements in the specimen except hafnium,molybdenum, titanium, tantalum, tungsten, and zirconium possess vapor pressures greater than 10^{-6} Torr below 1473°K.

b. Surface Characterization of NbB_2

Figure 23 shows the polished surface of the specimen and Figure 24 is the structure of the etched surface at 300 x magnification, before emissivity measurements were made. The procedure for etching consisted of swabbing the polished surface with 48% hydrofluoric acid, followed by immersing in concentrated orthophosphoric acid at 100°C for 30 minutes. The surfaces shown in Figures 23 and 24 indicate no well defined crystal structure and are typical of refractory materials consolidated by sintering from micronized powders. Figure 25 is a view of the surface structure after heating to 2415°K during emissivity measurement. It can be seen that an evaporation polishing has taken place.

Figure 26 is an electron micrographic view of the etched surface of NbB_2 at 56,700x magnification before emissivity measurement and indicates the presence of crystals about 3 microns in size. These crystals were not clearly visible under the light microscope. Figure 27 is an electron microscope view after heating the NbB_2 specimen to 2415°F. Comparison with Figure 26 leads to the conclusion that virtually no crystal growth took place and that thermal polishing does occur. From emissivity data presented in Figure 28, Curve 1, it appears from the displacement of the curve that thermal polishing may have taken place during initial heating at 1594°K after which the surface remains relatively stable during measurement at higher temperatures.

c. X-Ray Diffraction Studies - NbB_2

X-ray diffraction measurements provide an opportunity to examine crystal character such as phase changes, orientation, and composition. The x-ray data for NbB_2 are shown in Table 25 giving the relative intensities of reflected rays I/I_o "d" spacings in Ångstrom units and Miller indices, hkl.

Table 25

X-RAY DIFFRACTION PATTERN - NbB_2

I/I_o	d,Å Measured	Impurity Lines	ASTM d-values	hkl
30	3.30	NONE	3.28	001
50	2.69		2.68	100
100	2.08		2.07	101
5	1.65		1.64	002
15	1.55		1.55	110
20	1.40		1.40	111
10	1.34		1.34	100
15	1.24		1.24	201
10	1.13		1.12	112
5	1.04		1.04	202
5	1.02		1.01	210
5	.972		0.970	211
5	.896		.896	113
5	.865		.865	212
-	-		.849	203

Figure 23. Polished NbB_2 - 300X

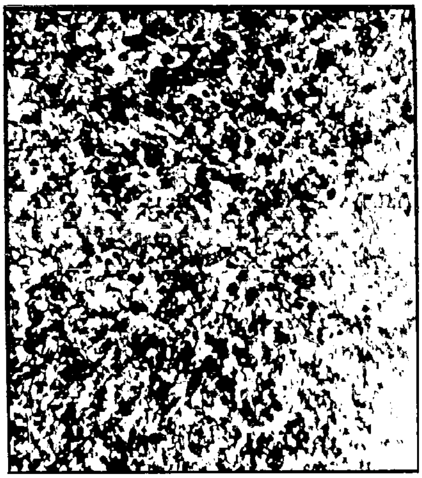

Figure 24. Etched NbB_2 - 300X

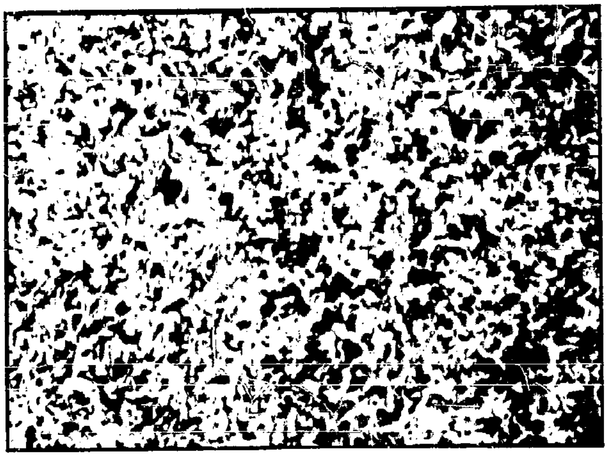

Figure 25. NbB_2 After Heating to 2415°F. - 300X

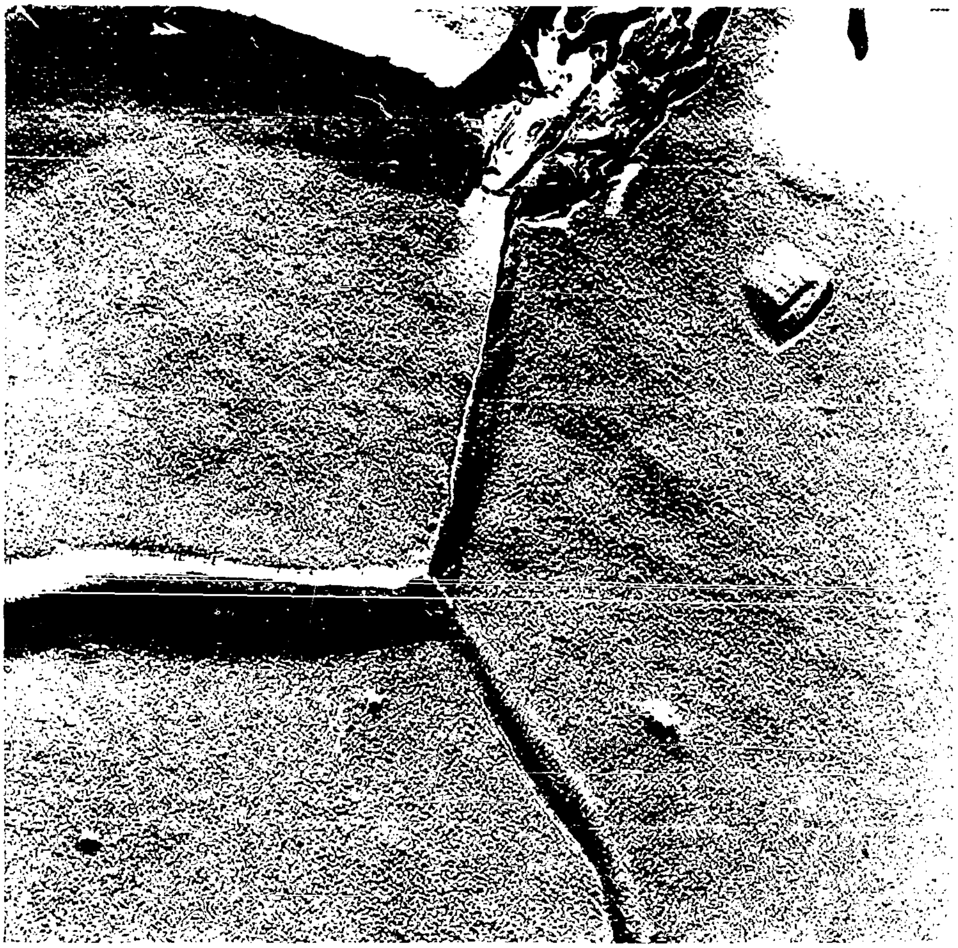

Figure 26. Etched NbB_2 Before Heating - 56700X

Figure 27. NbB_2 After Heating to 2415°K - 56700X

From the indices given in Table 25, a hexagonal structure is indicated having the following cell parameters: a = 3.1, c = 3.3, and c/a ratio = 1.06. The x-ray values, measured after the NbB_2 had been heated to 2415°K during emissivity measurement, showed no change. It therefore could be concluded that no transformation or change in composition took place in the specimen during measurement.

d. Weight and Density - NbB_2

Weight and density measurements were made before and after measuring emissivity and the results are tabulated below:

Table 26

WEIGHT AND DENSITY - NbB_2

	Before	After	Change
Weight-gms	1.5027	1.4722	-.0305
Density-g/cm^3	6.30	6.00	-.30

The Carborundum Co. reports a density of 6.40 gms/cm^3, while density values of 7.21 and 6.4 have been reported (7, 8).

The observed decrease in weight of 2% was accompanied by virtually no change in volume. Evidence of being porous or having reacted to form a lower density compound was not detected by electron microscope examination and x-ray analysis.

e. Normal Spectral Emissivity - NbB_2

Variation of normal spectral emissivity with wavelength is shown in Figures 28, and 29. Data for curves 1, 2, 3, and 6, were determined at temperatures of 1594°K, 1821°K, 2000 K, and 2415°K respectively. Figure 29 plots data obtained at 1593°K and 1819°K. Curve 6 is repeated to facilitate relating Figure 28 with Figure 29 data.

The dip shown in the 1594°K Curve 1, starting at 0.5 micron is believed to be caused by the transitional change in surface structure indicated in the electron micrographs. Emissivity data determined at 1593°K, Curve 4, was measured after the 2415°K run and is in good agreement with data initially taken at 1594°K. At 0.95 micron, emissivity shows no change with temperature.

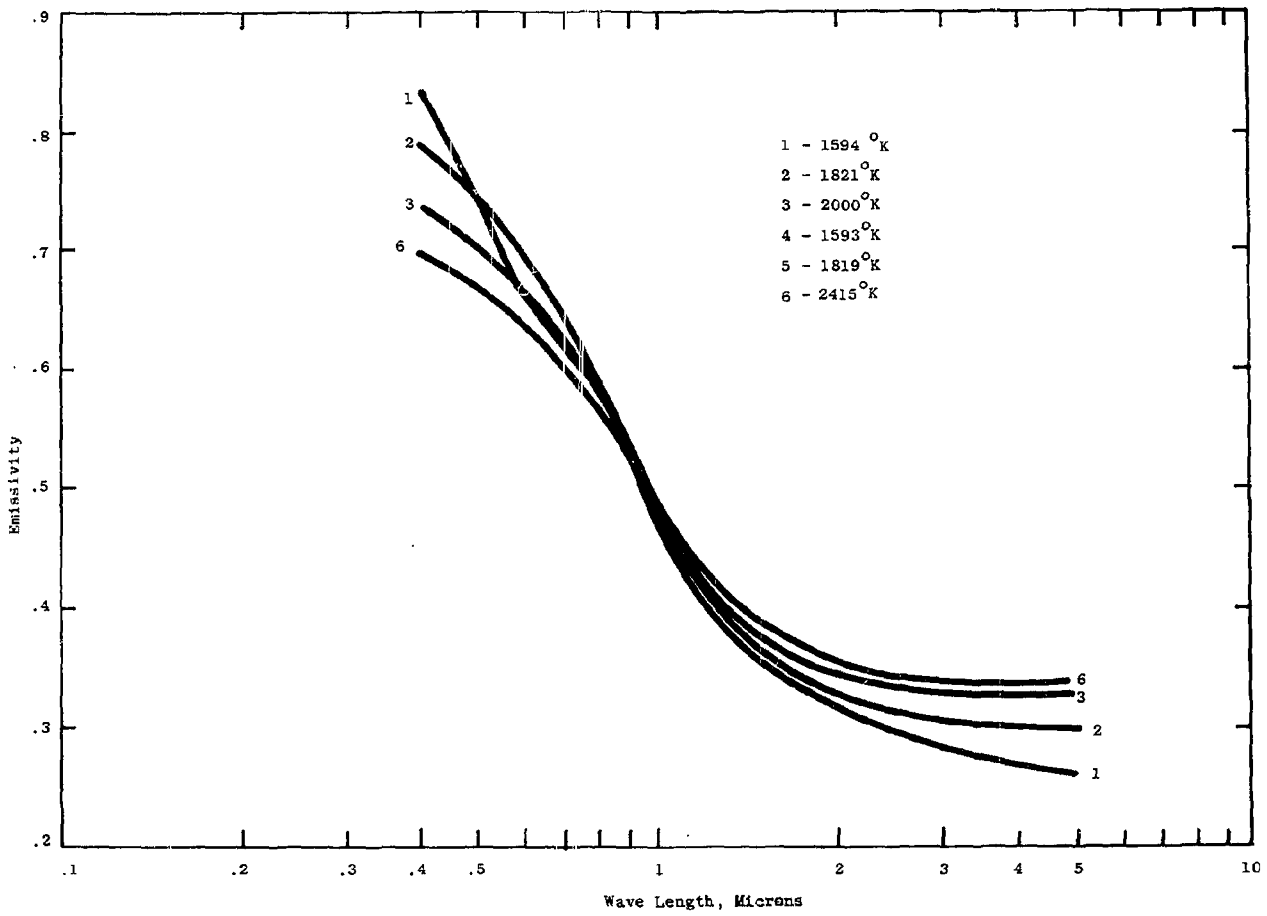

Figure 28. Normal Spectral Emissivity - NbB_2, Specimen 1

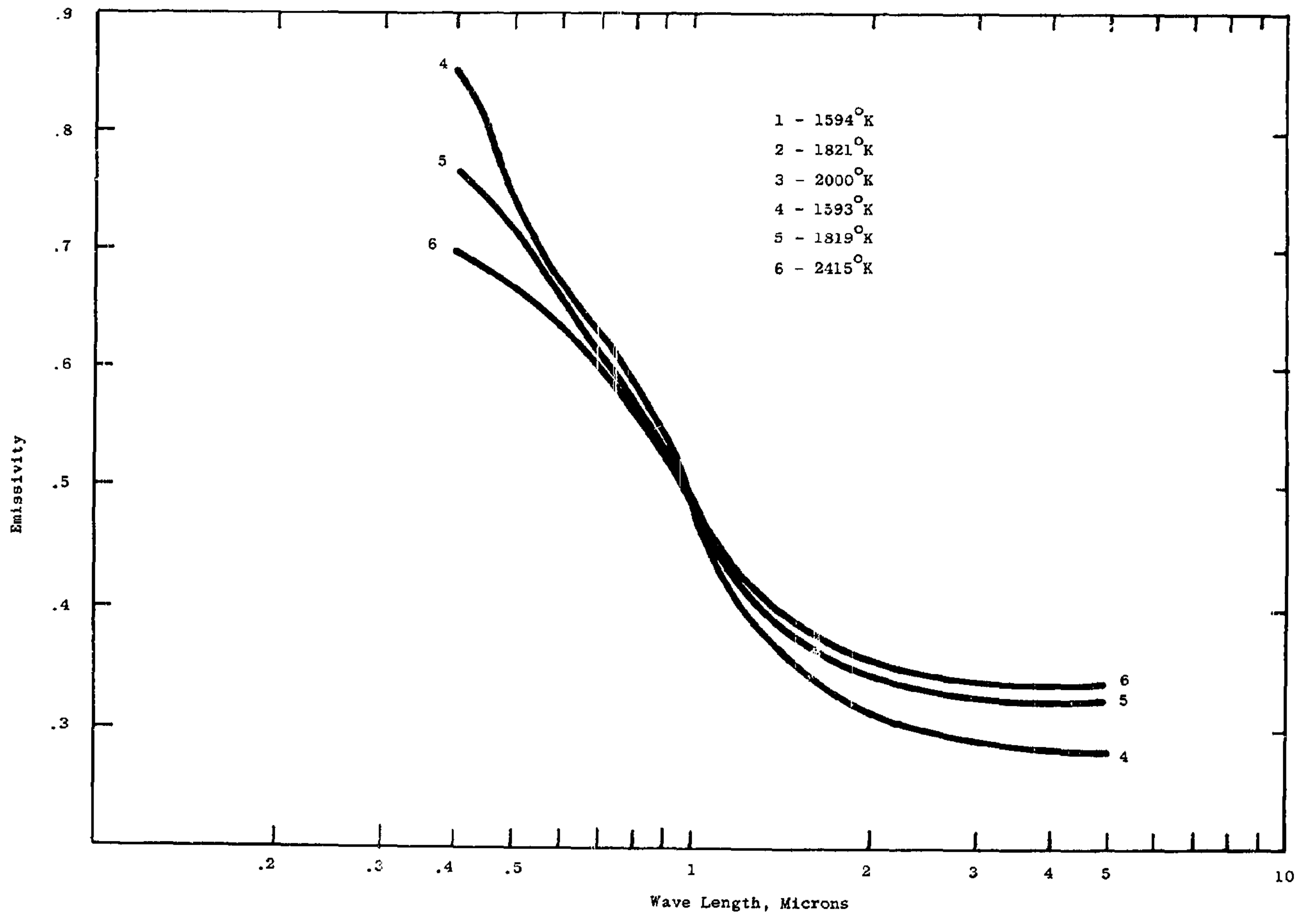

Figure 29. Normal Spectral Emissivity - NbB_2, Specimen 1

Figure 30 presents emissivity measurements on another specimen of NbB_2 selected from the same lot. Emissivity values were determined at 1540°K, 1800°K, and 2000°K. Here there is virtually no change in emissivity with temperature out to 1.1 microns. The reason for this difference between Specimens 1 and 2 is not understood.

Normal total emissivity (ϵ_{nt}) calculated from spectral data at each temperature is tabulated in Table 27.

Table 27

NORMAL TOTAL EMISSIVITY - NbB_2

Temperature, °K	ϵ_{nt}	
1594	.309	Calculated from spectral data presented in Figures 28 and 29
1593	.320	
1821	.340	
1819	.344	
2000	.347	
2415	.409	
1540	.290	Calculated from spectral data presented in Figure 30
1800	.320	
2000	.350	

These data are also plotted in Figure 31. Data previously reported (1) for the carbides of tantalum and zirconium are also shown. Included for reference are plots of total normal emissivity of the borides of zirconium and titanium.

The temperature dependence of emissivity at constant wavelength is shown in Figure 32. It is proper to extrapolate these data to higher temperatures and, by applying the appropriate black body distributions, to obtain total normal emissivity at temperatures much higher than those for which spectral emissivities have been measured. Figure 33 is a plot of the temperature coefficient of emissivity $\frac{\partial \epsilon}{\partial T}$ as a function of wavelength.

Figure 34 shows the percent summation of total radiant energy emitted from niobium diboride below a selected wavelength compared to black body radiation at the same temperature and wavelengths for two temperatures ; 2000°K and 2415°K. For example, at 2000°K, NbB_2

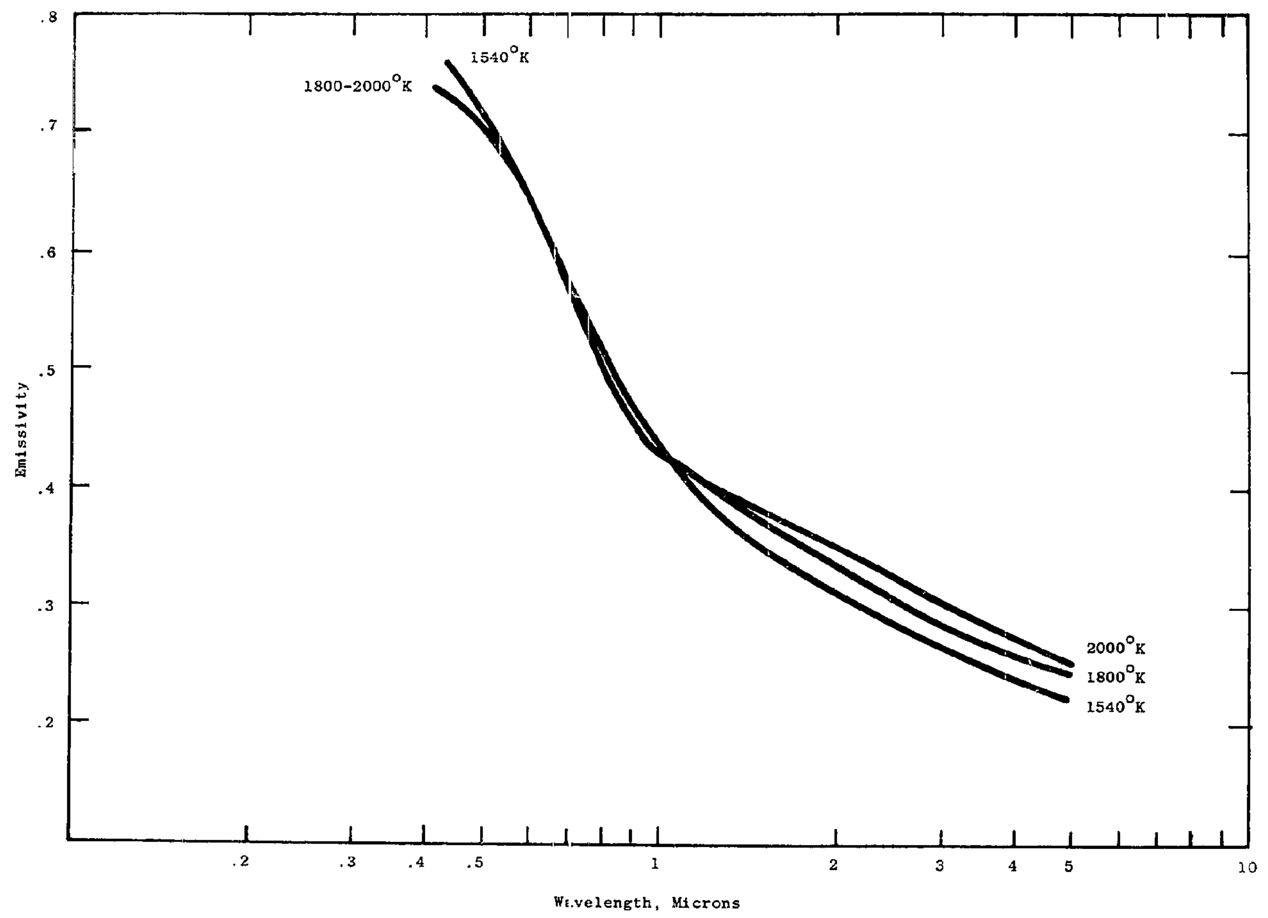

Figure 30. Normal Spectral Emissivity - NbB_2, Specimen 2

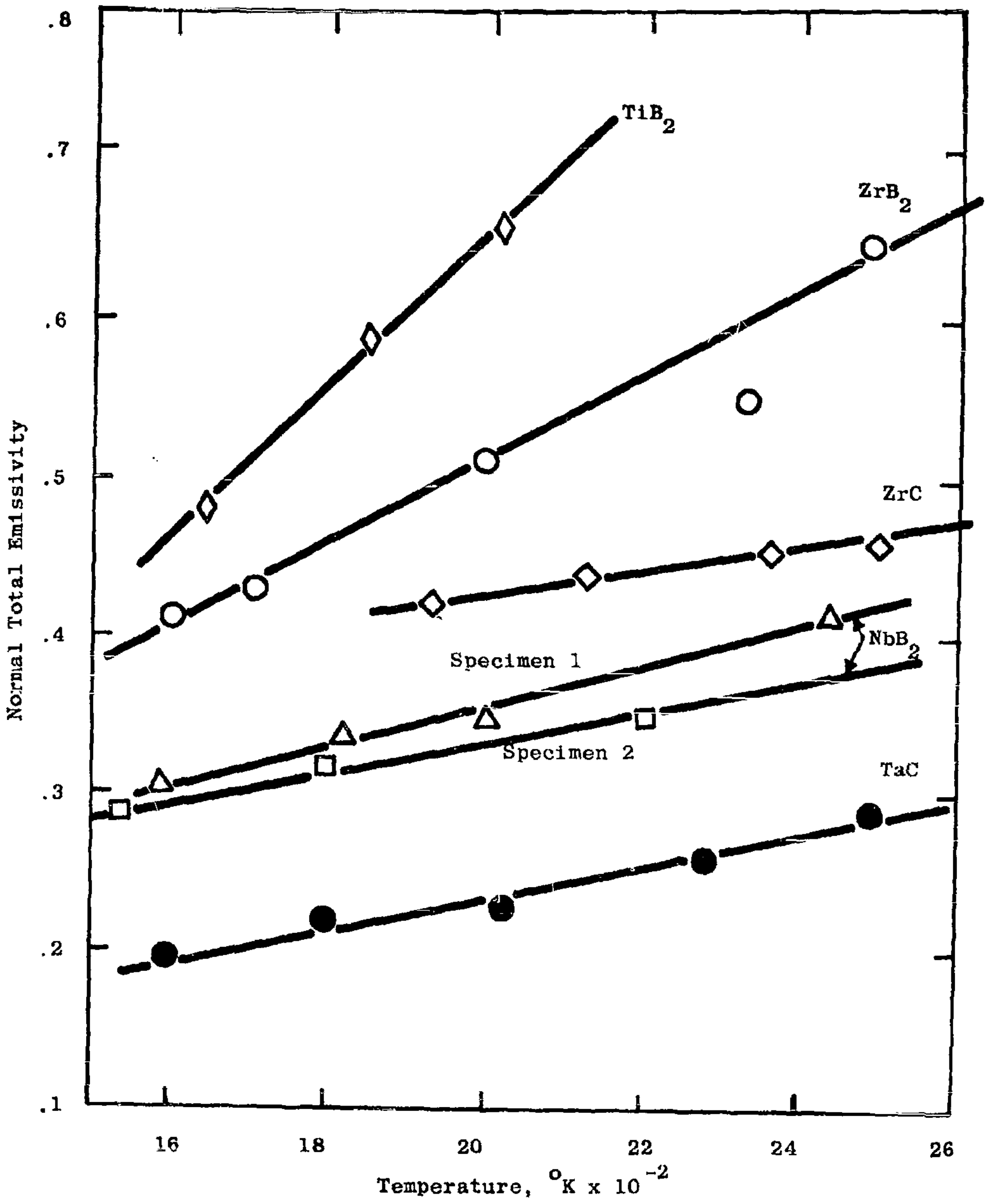

Figure 31. Normal Total Emissivity of Selected Carbides and Borides

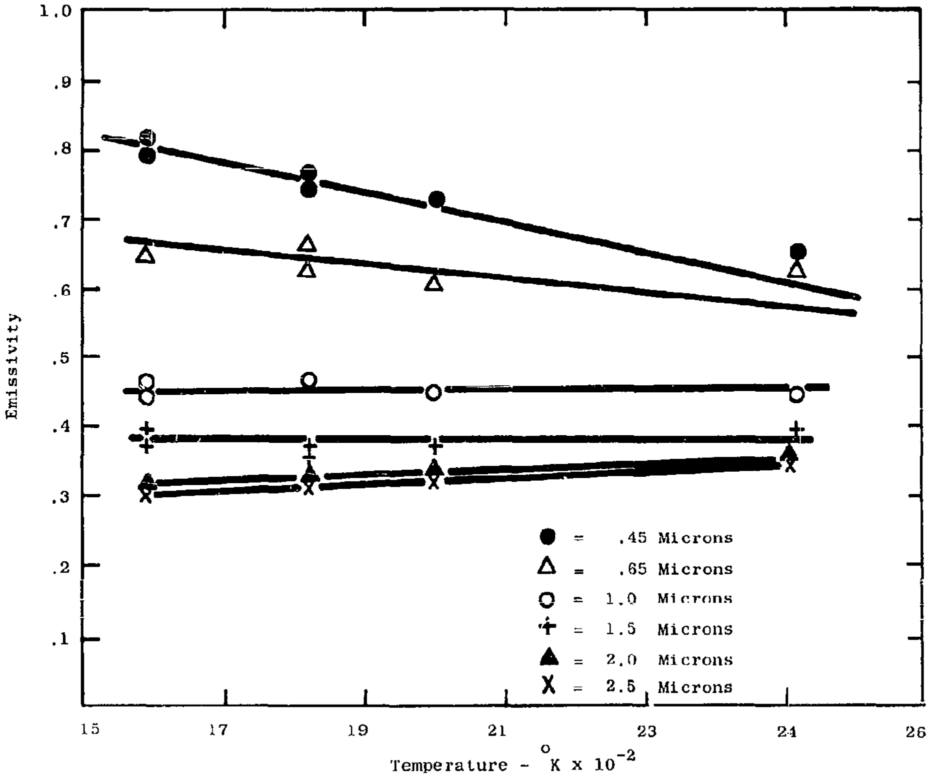

Figure 32. Temperature Dependence of Emissivity - NbB_2, Specimen 1

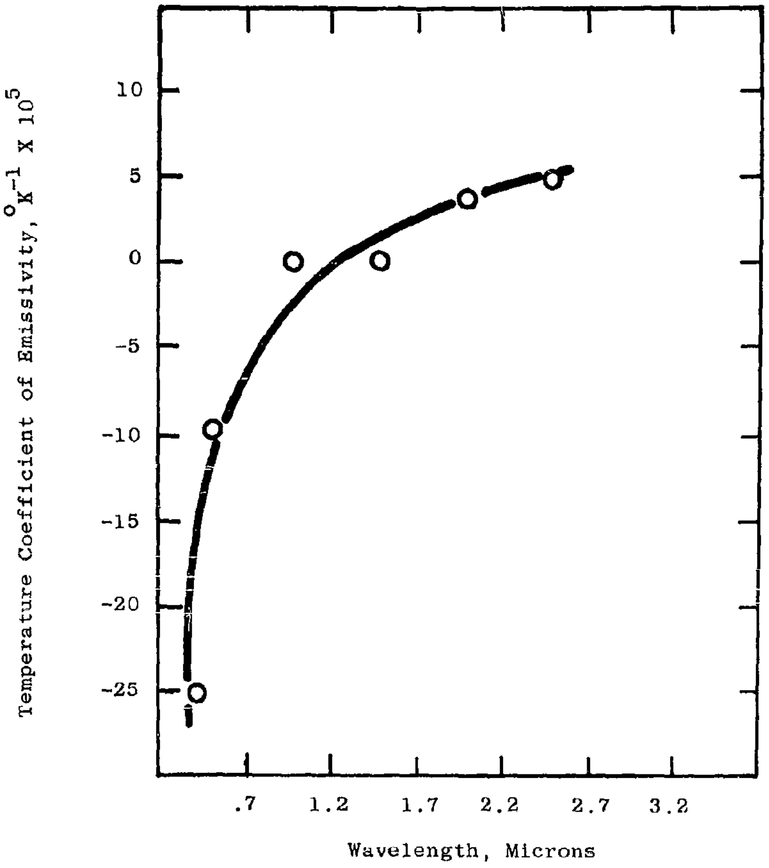

Figure 33. Temperature Coefficient of Emissivity-NbB_2, Specimen 1

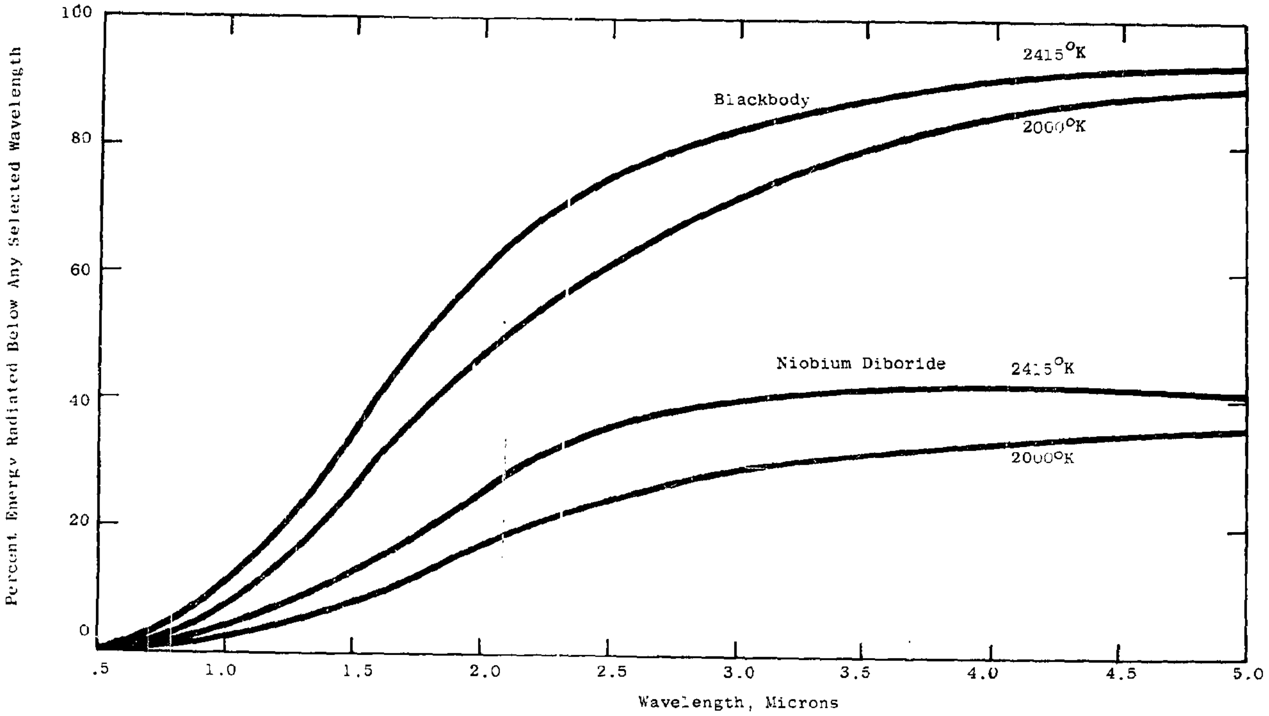

Figure 34. Relative Radiant Energy - NbB_2, Specimen 1

radiates 20% of the total energy below 2.2μ while a black body at the same temperature radiates 50% of the total energy below this wavelength.

2. Zirconium Diboride - ZrB_2

This compound is a crystalline material possessing a hexagonal structure and an x-ray theoretical density of 6.09 g/cm^3 (5). A Mohs hardness of 8 has been reported (8). Its melting point is in the region of 3000°C (5).

a. Chemical Analysis - ZrB_2

Table 28 gives the results of chemical analysis of the ZrB_2 specimen on which emissivity determinations were run.

Table 28

CHEMICAL ANALYSIS ZrB_2

Zirconium		75.03%	Lithium	ND	10 PPM
Boron		13.66%	Magnesium		30 PPM
Tungsten		3.% (estimate)	Manganese		50 PPM
Carbon		0.2% (estimate)	Molybdenum	ND	10 PPM
Oxygen		8.% (estimate)	Sodium		10 PPM
Silver	ND	5 PPM	Columbium	ND	100 PPM
Aluminum		300 PPM	Nickel		20 PPM
Arsenic	ND	100 PPM	Lead		10 PPM
Barium	ND	10 PPM	Antimony	ND	50 PPM
Beryllium	ND	10 PPM	Silicon		300 PPM
Bismuth	ND	10 PPM	Tin	ND	10 PPM
Calcium		1200 PPM	Strontium	ND	10 PPM
Cadmium	ND	10 PPM	Tantalum	ND	500 PPM
Cobalt	ND	10 PPM	Tellurium	ND	100 PPM
Chromium		50 PPM	Thallium	ND	10 PPM
Copper		10 PPM	Titanium		50 PPM
Iron		5700 PPM	Vanadium		30 PPM
Germanium	ND	10 PPM	Zinc	ND	50 PPM
Hafnium		300 PPM	Potassium		10 PPM
Indium	ND	10 PPM			

NOTE: ND = not detected, less than
PPM = parts per million

ZrB_2 has a theoretical composition of 80.82% zirconium and 19.18% boron. The above analysis indicates the presence of 8%

oxygen which confirms the x-ray findings of zirconium oxide (ZrO_2). Assuming that all of the available boron is combined with zirconium in the form of ZrB_2 the specimen then contains an excess of zirconium sufficient to combine with 75% of the available oxygen. The remaining oxygen is likely to be in combination with calcium and other trace elements.

It should be noted that this specimen contains 3% tungsten which may have influenced emissivity values. Tungsten and oxygen free specimens have since been obtained but time has not permitted running comparative emissivity measurements.

b. Surface Characterization - ZrB_2

Figure 35 shows a photomicrograph of the polished specimen 1 at 300 X magnification and Figure 36 is the same specimen after being etched. Figure 37 is a view after specimen 1 has been heated to 2389°K and Figure 38 shows the surface of specimen 2 after heating to 2480°K. There is a substantial difference in grain structure of the two specimens after thermal treatment. This is believed to be associated with a compositional change in specimen 1 that was subsequently confirmed by x-ray studies. Figure 30 at 72000X magnification, and Figure 40, at the same magnification, are electron micrographs of ZrB_2 (specimen 2) before and after running emissivity measurements to 2480°K. At this magnification a well defined grain structure possessing an average grain size of about 3 can be observed. Thermal treatment results in changes in surface structure evidenced by pitting and thermal etching. Keeping in mind that these changes are taking place during measurement of emissivity, it is believed that a coincident increase in radiation scattering takes place. This would have the effect of increasing emissivity. If however that region on the surface from which radiation is being measured becomes polished by evaporation, emissivity would decrease. The decrease in emissivity measured at constant temperature of 2000°K, Figure 42 appears to be caused by such a surface modification.

c. X-ray Diffraction Studies - ZrB_2

X-ray diffractometer measurements were run on the two ZrB_2 specimens on which emissivity measurements were made. Both specimens showed the same diffraction patterns before heating. In addition to lines characteristic of ZrB_2, very strong ZrO_2 lines were observed on the polished surfaces. The etched surfaces indexed to the same values but gave weaker ZrO_2 lines indicating that etching removes oxide from the surface where concentration appears to be higher than in the bulk material. There were also lines present of sufficient intensity to indicate existence of another impurity phase which was not identified. Because chemical analysis shows the presence of tungsten, this phase is thought to be tungsten boride. Table 29 gives the

Figure 35. Polished ZrB_2 - 300X

Figure 36. Etched ZrB_2 - 300X

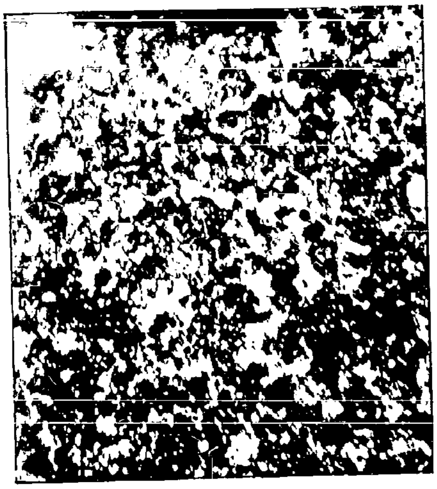

Figure 37. ZrB_2 After Heating to 2389°K - 300X

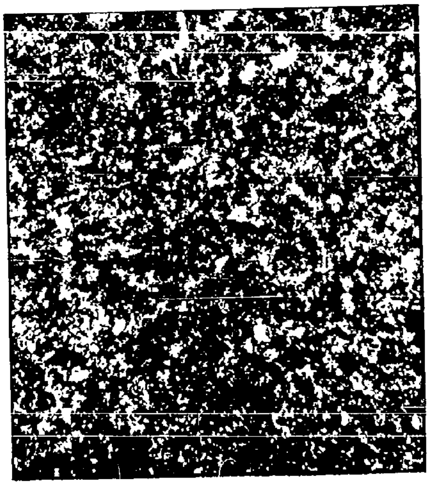

Figure 38. ZrB_2 After Heating to 2480°K - 300X

Figure 39. Etched ZrB_2 - 72000X

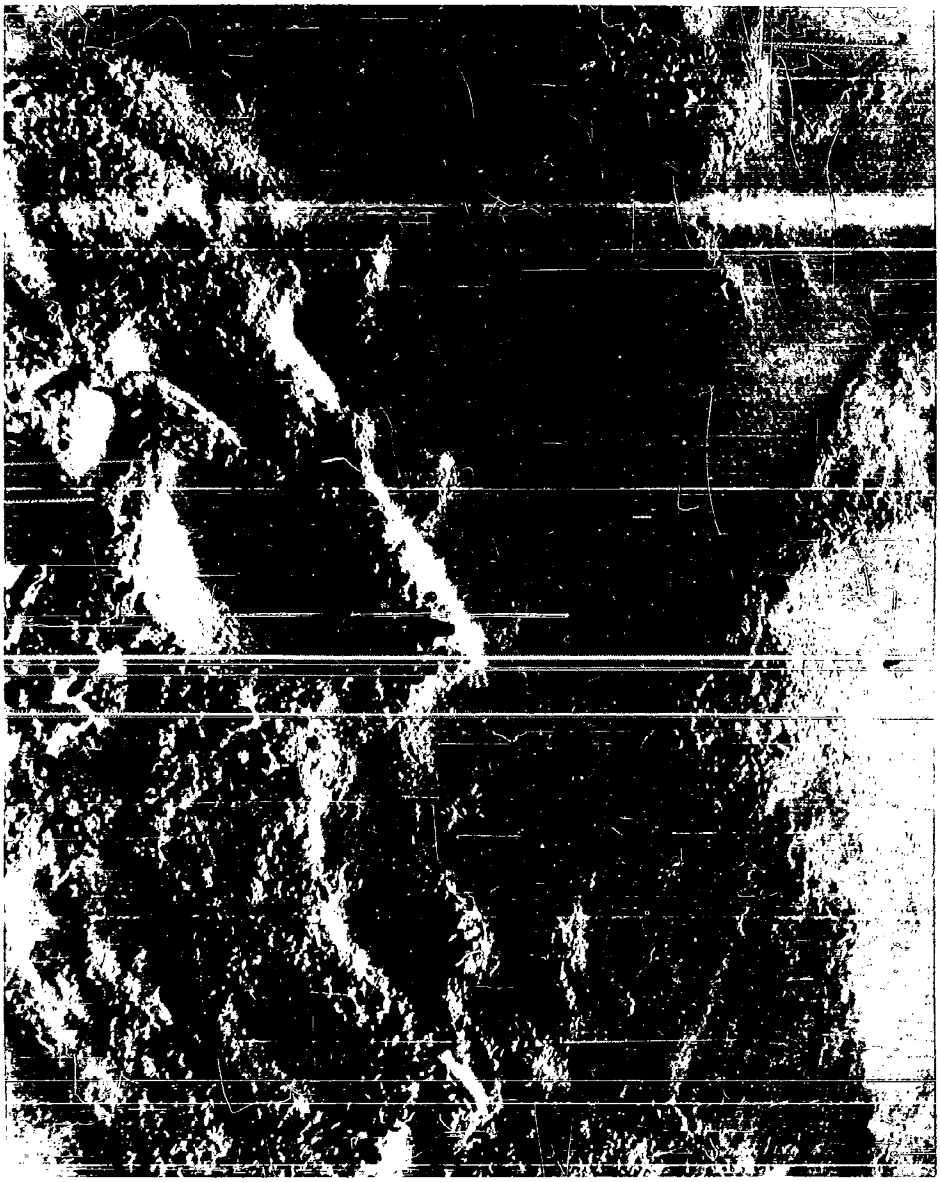

Figure 40. ZrB_2 After Heating to 2480°K - 72000X

intensities, I/I_o, (peak height ratios), "d" spacings, and Miller indices hkl, as measured. Table 30 gives the indexed pattern for specimen 1 after completion of emissivity measurements to 2389°K for which emissivity data are plotted in Figure 41. It was found that the "d" spacings were characteristic of zirconium nitride indicating that the specimen surface had nitrided during measurement. This was believed to have been caused by air becoming mixed with the argon atmosphere, the oxygen being extracted by the hot titanium purifier leaving nitrogen available to react. Also Table 30 gives additional "d" spacings detected in the nitrided surface. These are characteristic of ZrO_2 which appears to be slightly higher in concentration than was observed in the specimen before emissivity measurements were made.

Upon grinding of the nitrided surface and taking off successive layers, the concentration of ZrN was found to decrease to zero after the removal of about 5 mils of thickness and the x-ray pattern reverted to the lattice spacings characteristic of ZrB_2 and ZrO_2 as originally observed and listed in Table 29.

Table 29

X-RAY DIFFRACTION PATTERN

ZrB_2 Specimen 1 - Before Heating

I/I_o	d,Å Measured	Impurity Lines	ASTM d-values	hkl
30	3.53	NONE	3.53	001
60	2.74		2.74	100
100	2.16		2.16	101
10	1.76		1.76	002
20	1.58		1.58	110
25	1.48		1.48	102
15	1.44		1.44	111
5	1.37		1.37	200
5	1.28		1.28	201
5	1.18		1.18	112
5	1.07		1.08	103
7	.995		.994	211
10	3.15	ZrO_2	3.16	111
7	2.84	ZrO_2	2.84	111
5	1.81	ZrO_2	1.81	220

Table 30

X-RAY DIFFRACTION PATTERN

ZrB_2 Specimen 1 - After Heating

I/I_o	d,Å Measured	Impurity Lines	ASTM d-Values	hkl
100	2.64	ZrN	2.64	111
70	2.29	ZrN	2.29	200
40	1.62	ZrN	1.62	220
30	1.38	ZrN	1.38	311
10	1.32	ZrN	1.32	222
5	1.15	ZrN	1.14	400
10	1.05	ZrN	1.05	331
10	1.02	ZrN	1.02	420
10	3.16	ZrO_2	3.16	111
5	2.84	ZrO_2	2.84	111
5	2.55	ZrO_2	2.54	200
3	1.81	ZrO_2	1.81	220
2	1.79	ZrO_2	1.78	221
2	1.54	ZrO_2	1.54	131

X-ray patterns for specimen 2 showed no change after emissivity determinations up to 2480°K.

d. Weight and Density - ZrB_2

Weight and density measurements, made before and after emissivity measurements, are tabulated below for specimens 1 and 2.

Table 31

WEIGHT AND DENSITY - ZrB_2

	Before	After	Change
Weight - gms.			
Specimen 1	1.8374	1.8104	-.0270
Specimen 2	2.0637	2.0296	-.0341
Density - gms/cc			
Specimen 1	5.03	4.65	-.38
Specimen 2	5.03	5.20	+.17

Carborundum Company reports a density of 5.50 gms/cm^3 for this material and the Literature reports 6.09 gms/cm^3 (7) and 6.08 to 6.17 gms/cm^3 (8).

The weight loss of 2.2% and 1.2% in specimen 1 and 2 respectively is difficult to interpret since the following factors are involved: 1)conversion of the surface of specimen 1 from boride to nitride, 2) difference in temperature, specimen 2 being heated 90° higher than specimen 1, 3) time at temperature (specimen 1 was at temperature about 6 hours longer than specimen 2), 4) specimen 2 showed slight reaction with the ZrO_2 holder. Specimen 2 shows an increase in density coincident with a slight decrease in weight. This is believed to result from further consolidation by sintering at the test temperatures.

e. Normal Spectral Emissivity - ZrB_2

Figure 41 shows a plot of emissivity of ZrB_2, specimen 1, at temperatures of 1704°K, 2030°K and 2389°K. Emissivity at 0.48 micron is the same for the two lower temperatures, and follows a characteristic decrease with wavelength. Curve 3 at 2389°K shows a substantial change in emissivity from what would have been predicted on the basis of lower temperature curves. Upon removal of the specimen from the emissometer, x-ray diffraction patterns, as previously described, indicated conversion of the surface to ZrN, undoubtedly due to an air leak in the system. This accounts for the emissivity change shown in curve 3 of Figure 41.

Figure 42 shows emissivity data run on specimen 2. Here the temperature was rapidly increased to 2000°K, allowed to stabilize, and a series of curves run in the order given. As mentioned, x-ray diffraction showed no change in composition during emissivity measurement. Thus specimen 2 did not nitride. About one hour was required for each determination. Curve 1, Figure 42, shows that polished ZrB_2 possessed a high emissivity, above 0.8 between 0.4μ and 2μ at which point the emissivity begins to decrease at a rapid rate to 0.55 at 5 microns. This is believed to be caused by surface modifications taking place during the first hour of heating. Curves 2, 3, 4 and 5 shows only a small emissivity change of about 0.03 between 0.4μ and 0.7μ and a 0.05 change between 0.7μ and 5μ while standing at 2000°C for a total of 8 hours.

Figure 43 shows the wavelength dependence of emissivity for specimen 2 after the 2000°K stabilization period. Measurements were made at 1604°K, 1702°K, 2000°K, 2330°K and 2480°K. Here the 2000°K determination is in good agreement with data presented in Figure 42.

Normal total emissivity (ϵnt) was calculated for ZrB_2 from spectral data presented in Figure 43. It is tabulated in Table 32 and shown plotted in Figure 31, Curve 3 and Figure 44. ZrB_2 radiation increases more rapidly with temperature than does NbB_2 indicating that as operating temperatures increase, its ability to dissipate heat by radiation is greater than NbB_2.

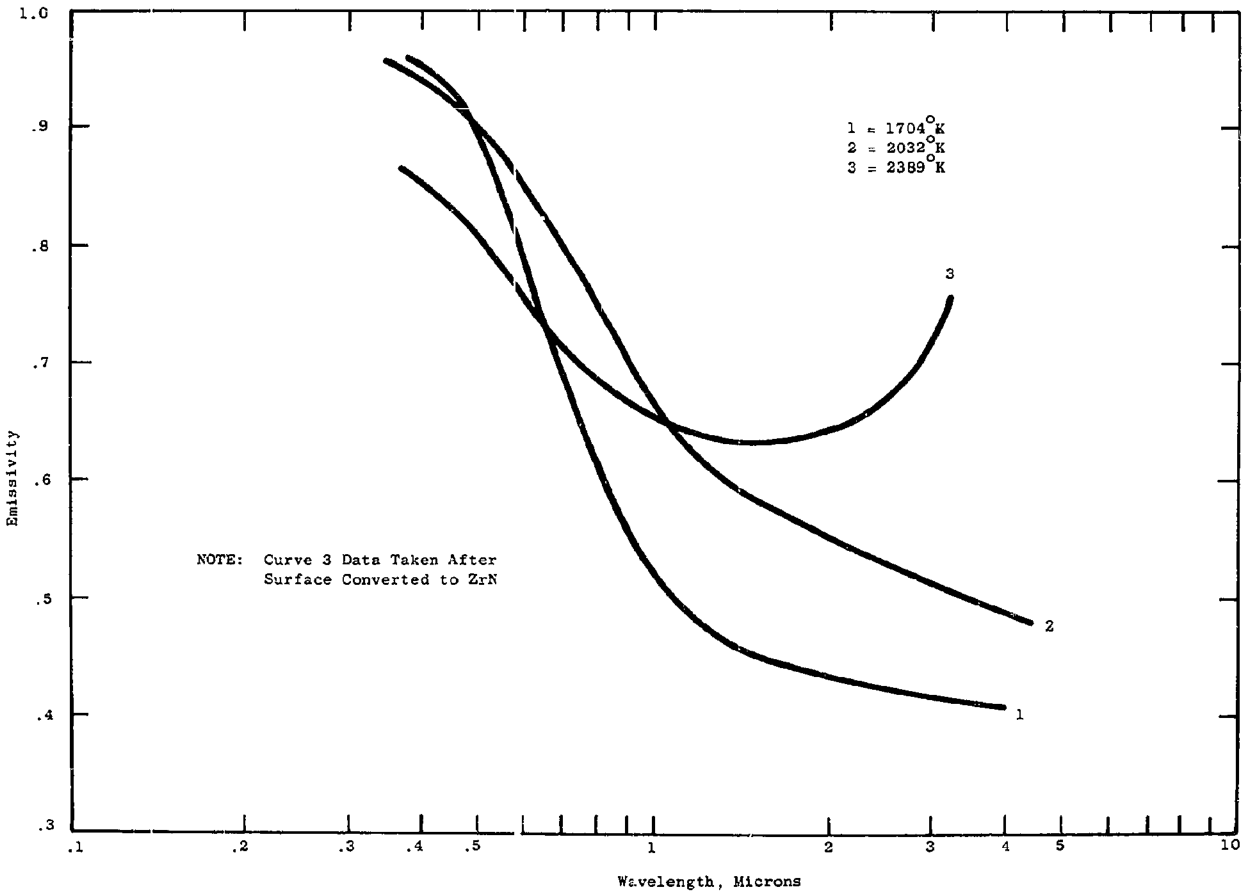

Figure 41. Normal Spectral Emissivity - ZrB_2 (Specimen 1)

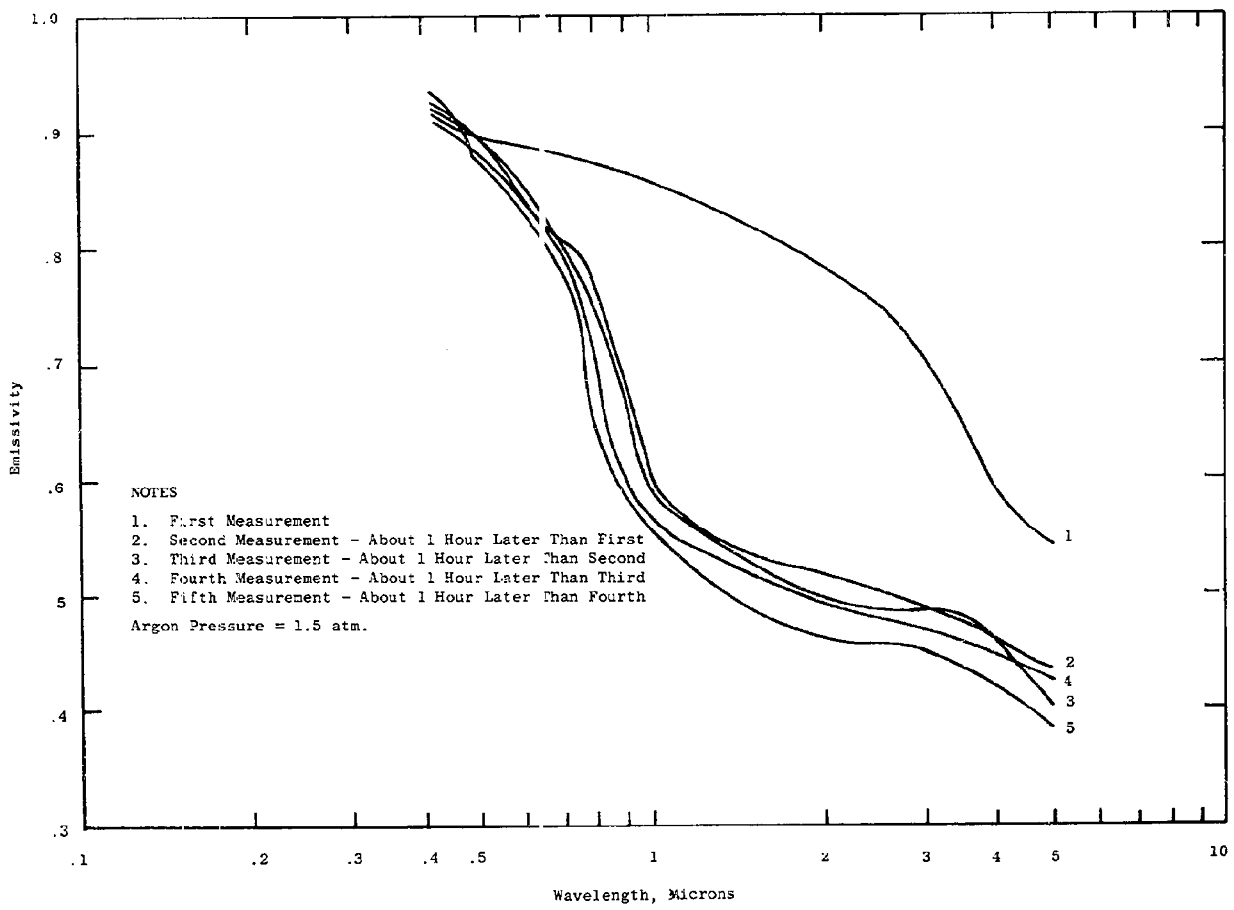

Figure 42. Normal Spectral Emissivity - ZrB_2 (Specimen 2) at 2000°K in Argon

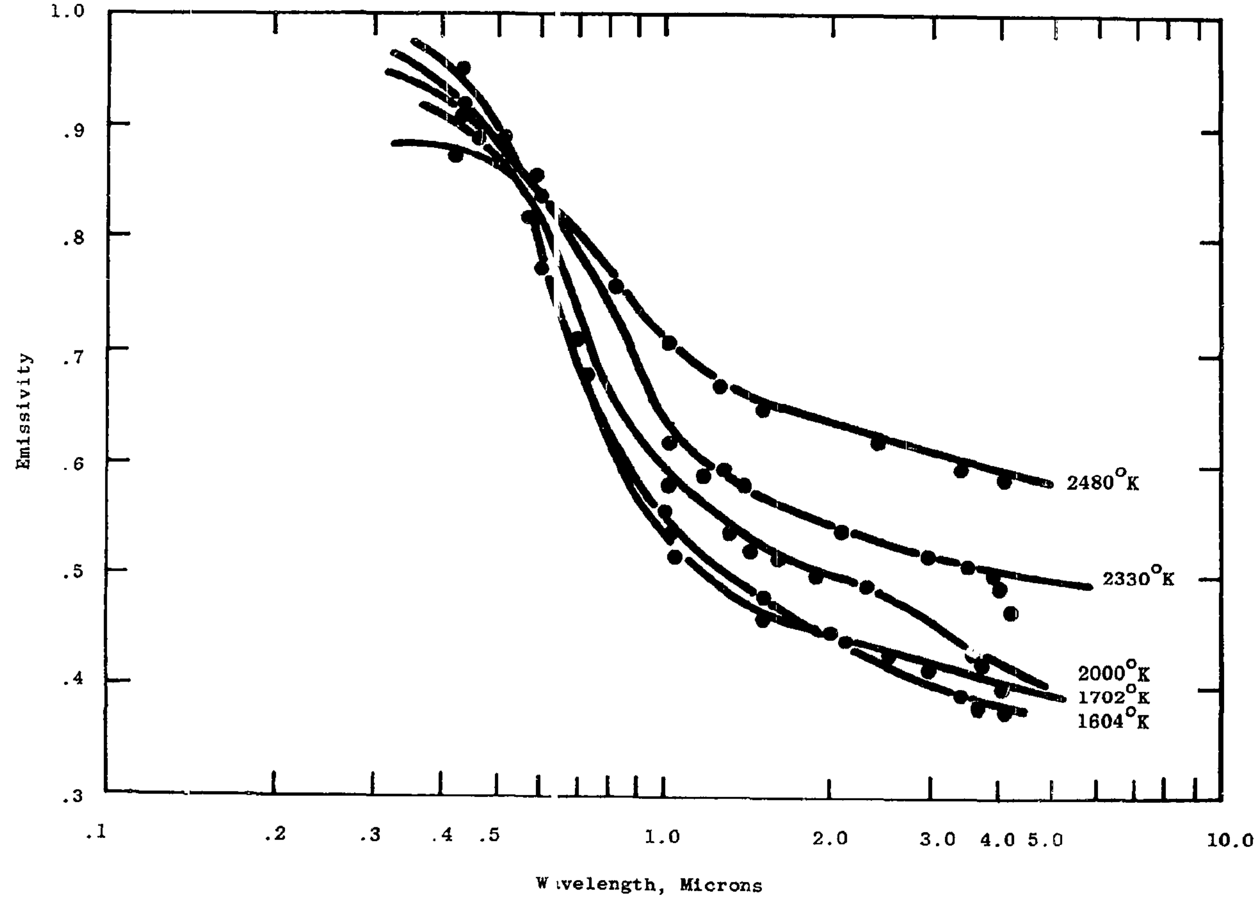

Figure 43. Normal Spectral Emissivity - ZrB_2 (Specimen 2) at Various Temperatures

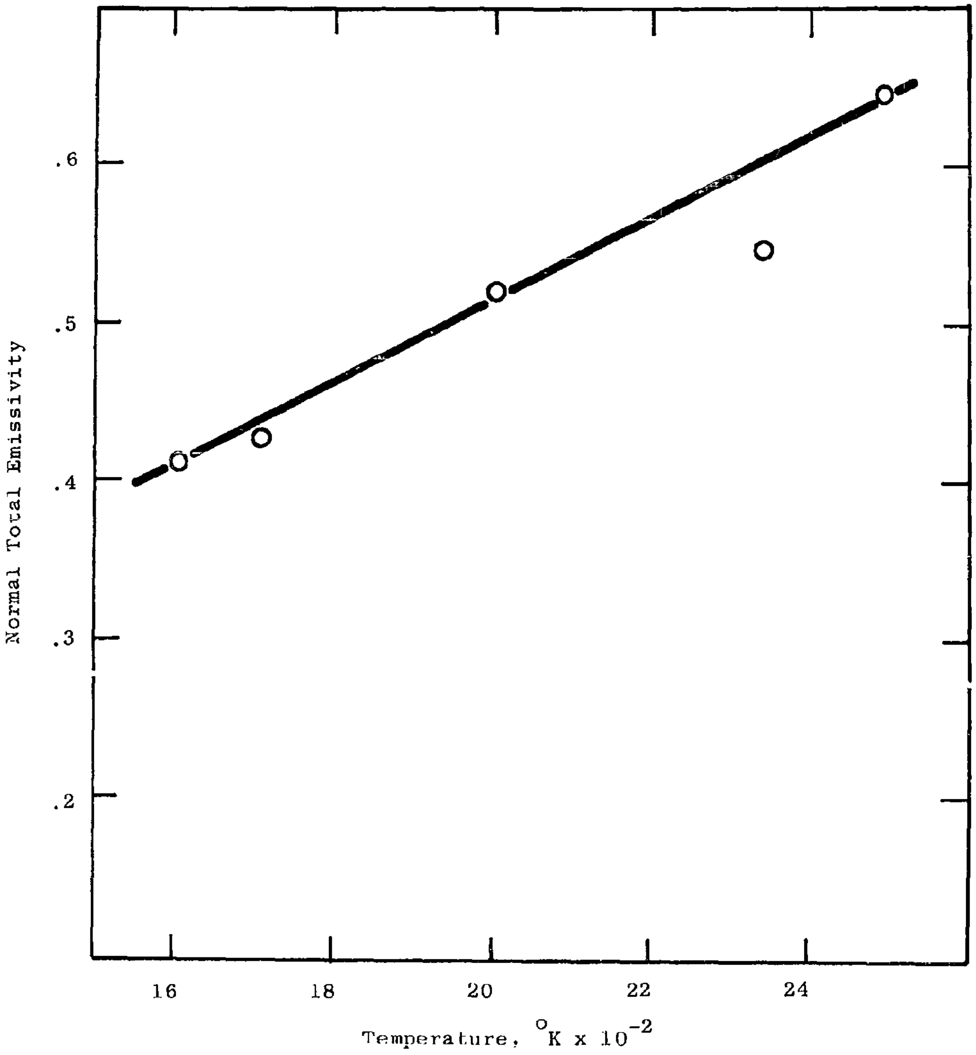

Figure 44. Normal Total Emissivity - ZrB_2, Specimen 2

Table 32

NORMAL TOTAL EMISSIVITY - ZrB_2 SPECIMEN 2

Temperature ^oK	ε_{nt}
1604	.44
1702	.46
2000	.52
2330	.54
2480	.65

Figure 45 shows the temperature dependence of emissivity at constant wavelength. At 0.8 micron, the rate of change of emissivity with temperature is zero. Figure 46 is a plot of the temperature coefficient of emissivity ($\frac{\partial \varepsilon}{\partial T}$) as a function of wavelength and Figure 47 shows the percent energy radiated from ZrB_2 at 2000°K and 2330°K compared to that radiated from a black body at the same temperature. These curves were calculated from normal spectral emissivity measurements on specimen 2. Because of nitriding of specimen 1, data on that specimen were discarded.

3 Titanium Diboride - TiB_2

Titanium diboride possesses a hexagonal crystal structure and a theoretical x-ray density of 4.54 gms/cm^3. It has a Mohs reported (5) hardness greater than 9 and a melting point at 2980°C (5). In cutting and polishing the TiB_2 specimens their hardness was found to be greater than the other materials studied in this work.

a. Chemical Analysis - TiB_2

Table 33 gives the chemical analysis of titanium diboride on which emissivity measurements were made. The theoretical composition is 68.89% titanium and 31.11% boron. From analytical results, it can be seen that the specimen contains an excess of boron over that which is required to form TiB_2. This excess is probably in combination with the trace refractory metals in the specimen.

Evaporation of the more volatile trace elements from samples of the indicated composition, during high temperature emissivity measurements, is most probable.

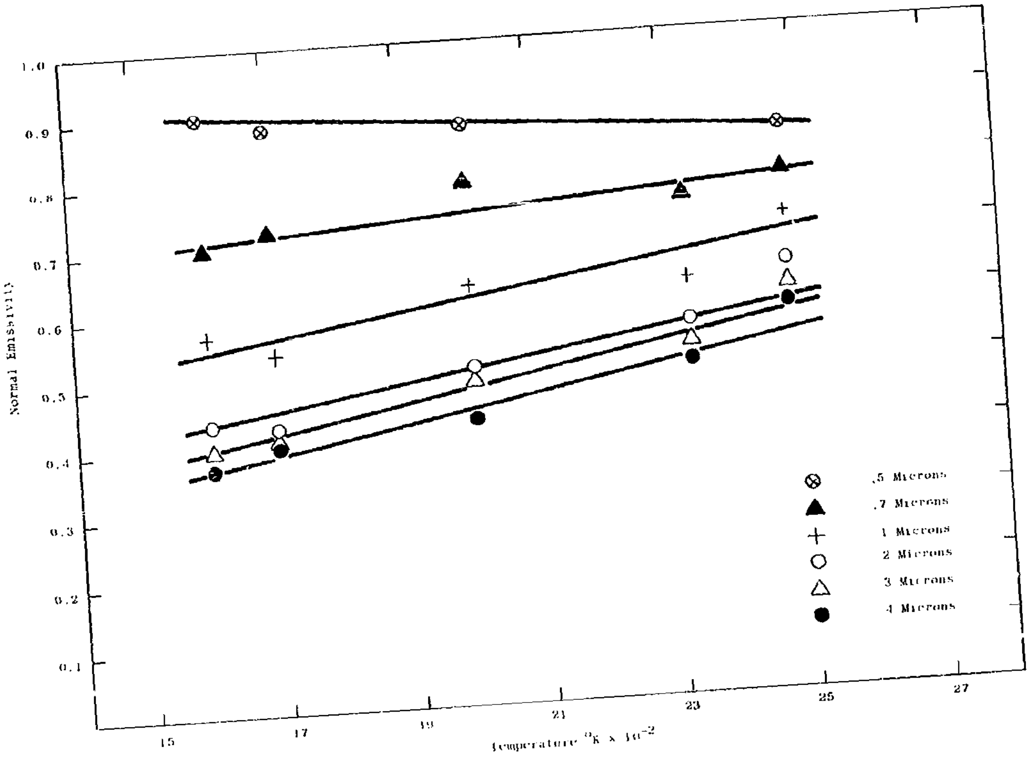

Figure 45. Temperature Dependence of Emissivity - ZrB_2, Specimen 2

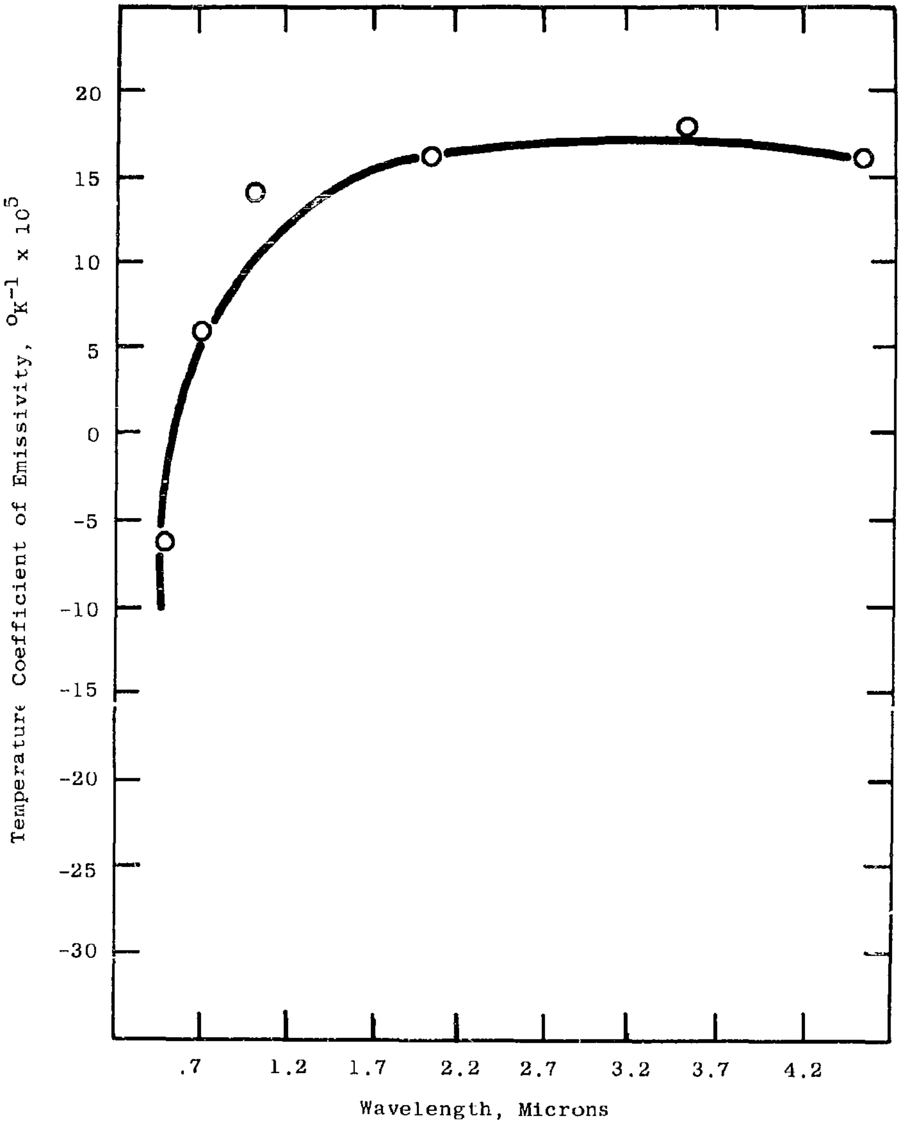

Figure 46. Temperature Coefficient of Emissivity - ZrB_2, Specimen 2

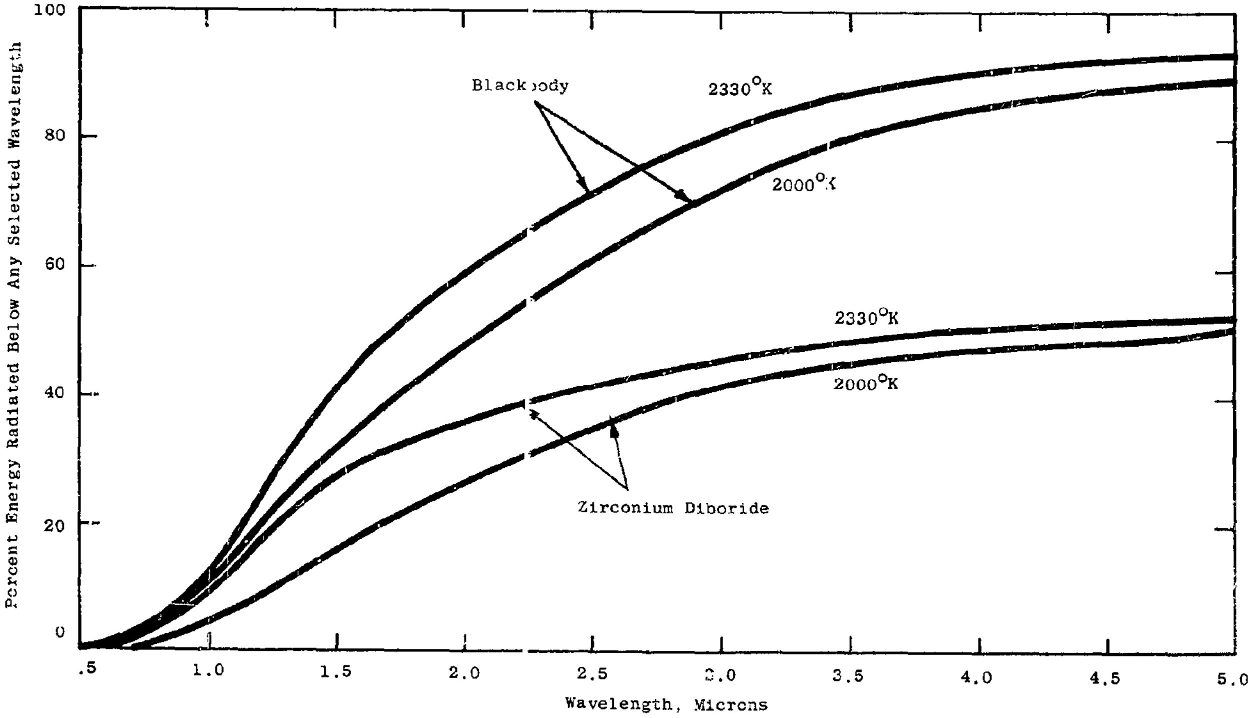

Figure 47. Relative Radiant Energy - ZrB_2, Specimen 2

Table 33

CHEMICAL ANALYSIS - TiB_2

Titanium		65.78%	Magnesium		5 PPM
Boron		31.07%	Manganese		10 PPM
Silver	ND	5 PPM	Molybdenum	ND	10 PPM
Aluminum		200 PPM	Sodium		20 PPM
Arsenic	ND	10 PPM	Columbium		300 PPM
Barium	ND	10 PPM	Nickel		20 PPM
Beryllium	ND	10 PPM	Lead	ND	10 PPM
Bismuth	ND	10 PPM	Antimony	ND	50 PPM
Calcium		10 PPM	Silicon		70 PPM
Cadmium	ND	10 PPM	Tin	ND	10 PPM
Cobalt	ND	10 PPM	Strontium	ND	10 PPM
Chromium		20 PPM	Tantalum	ND	500 PPM
Copper	ND	10 PPM	Tellurium	ND	100 PPM
Iron		2100 PPM	Thallium	ND	10 PPM
Germanium	ND	10 PPM	Vanadium		40 PPM
Hafnium	ND	100 PPM	Tungsten	ND	500 PPM
Indium	ND	10 PPM	Zinc	ND	500 PPM
Lithium	ND	10 PPM	Zirconium		1100 PPM
			Potassium		10 PPM

NOTE: ND = not detected, less than
PPM = parts per million

Oxygen -- Not determined and not detected by x-ray diffraction

b. Surface Characterization - TiB_2

Photomicrographs of titanium diboride specimen 2 were taken before and after measurement of emissivity. Figure 48 is a view of the polished surface at 300X. The dark areas are not voids but a contrasting reflectivity characteristic of various crystal planes. Figure 49 is the surface that has been etched by the same technique applied to NbB_2. It shows a structure characteristic of materials consolidated by sintering at high temperature. Figure 50 shows the same surface after having been heated in an argon atmosphere to 2022°K. Here the grain boundaries become well defined and the crystals have taken on a granular structure. Figure 52 is an electron micrograph of this same surface at 20600X after heating to 2022°K. Here the crystal shows well defined boundaries and a structure indicative of thermal polishing having taken place. Contrasted with this is the electron micrograph of the etched structure before heating shown in Figure 51. Emissivity data for this specimen are presented in Figures 54 and 55, and are discussed later. Figure 53 presents emissivity data for specimen 1.

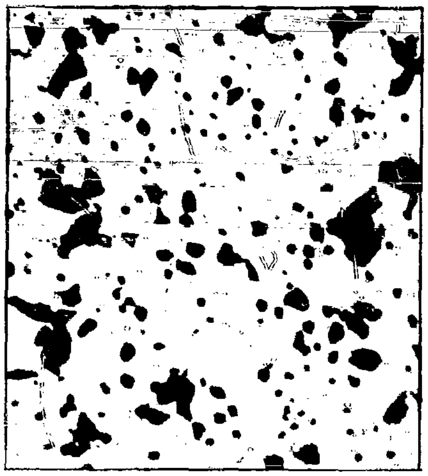

Figure 48. Polished TiB_2 - 300X

Figure 49. Etched TiB_2 - 300X

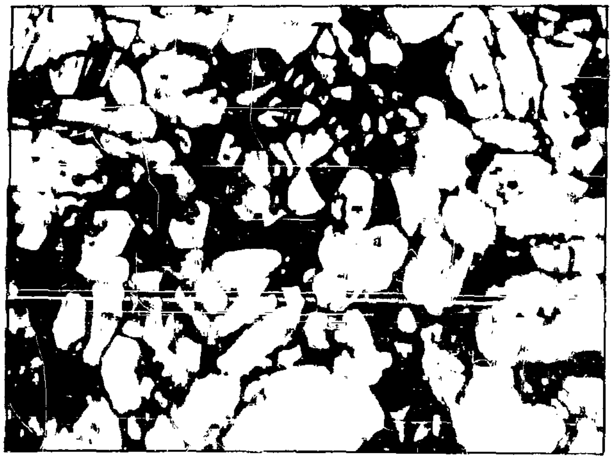

Figure 50. TiB_2 After Heating to 2022°K - 300X

Figure 51. Etched TiB_2 Before Heating - 16200X

Figure 52. TiB_2 After Heating - 20600X

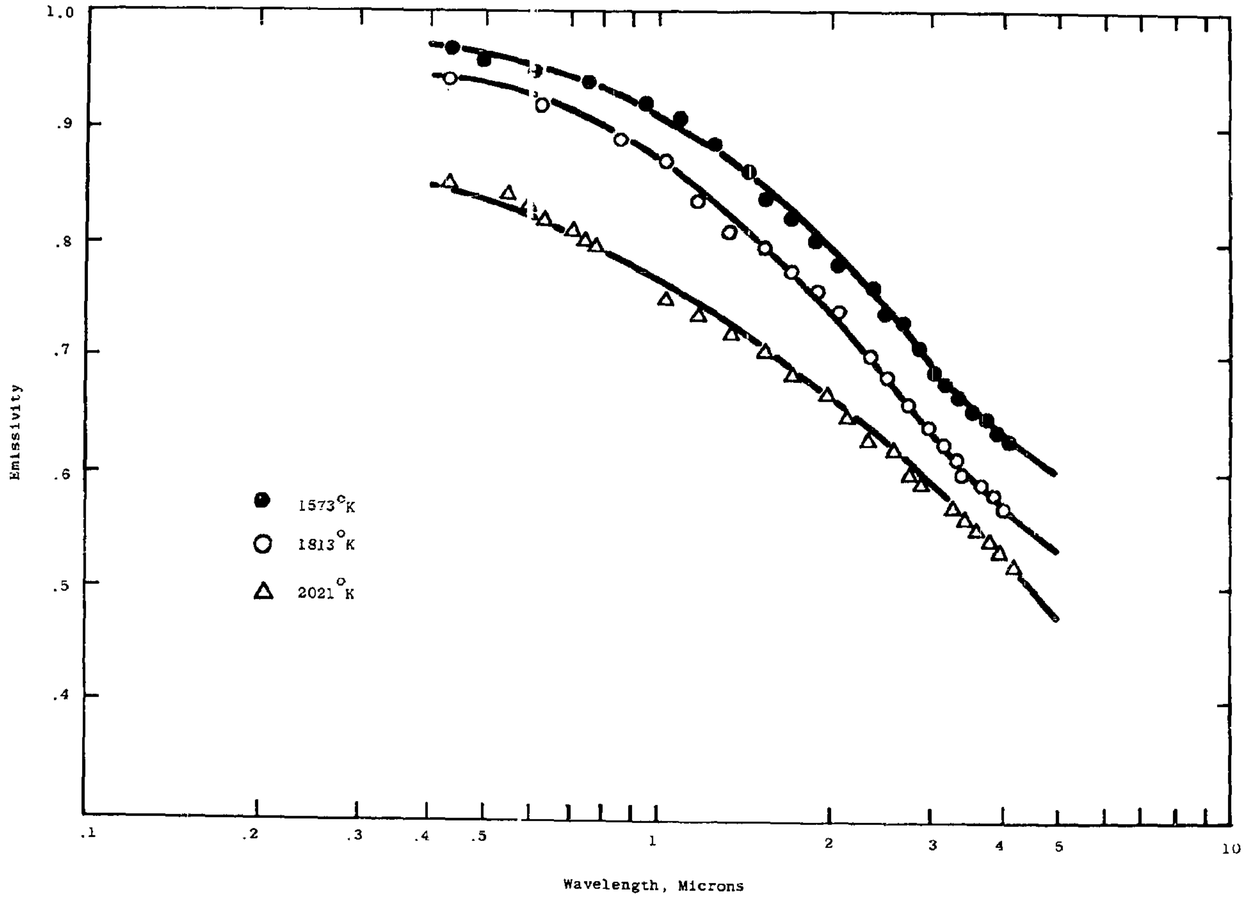

Figure 53. Normal Spectral Emissivity - TiB_2 Specimen 1

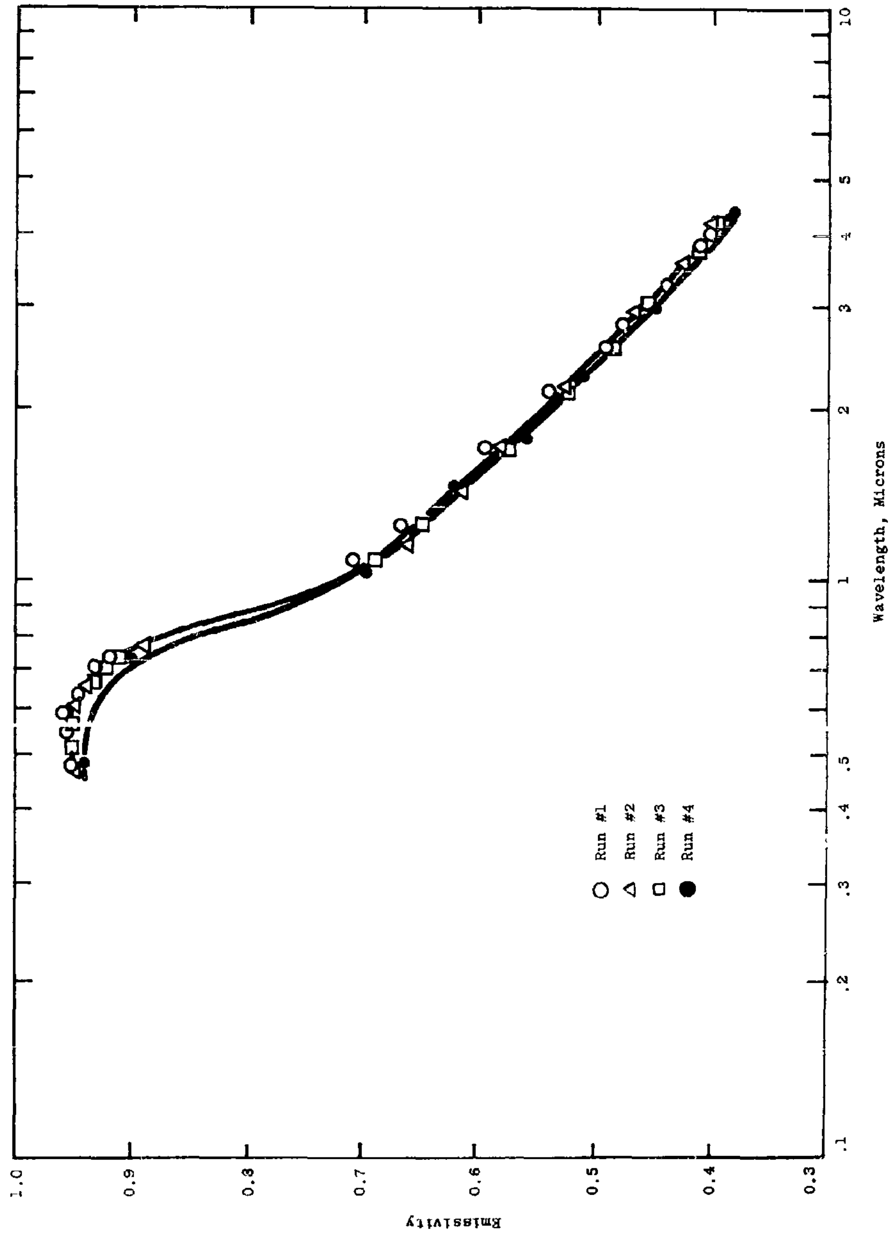

Figure 54. Normal Spectral Emissivity - TiB_2 (Specimen 2) at 1648°K

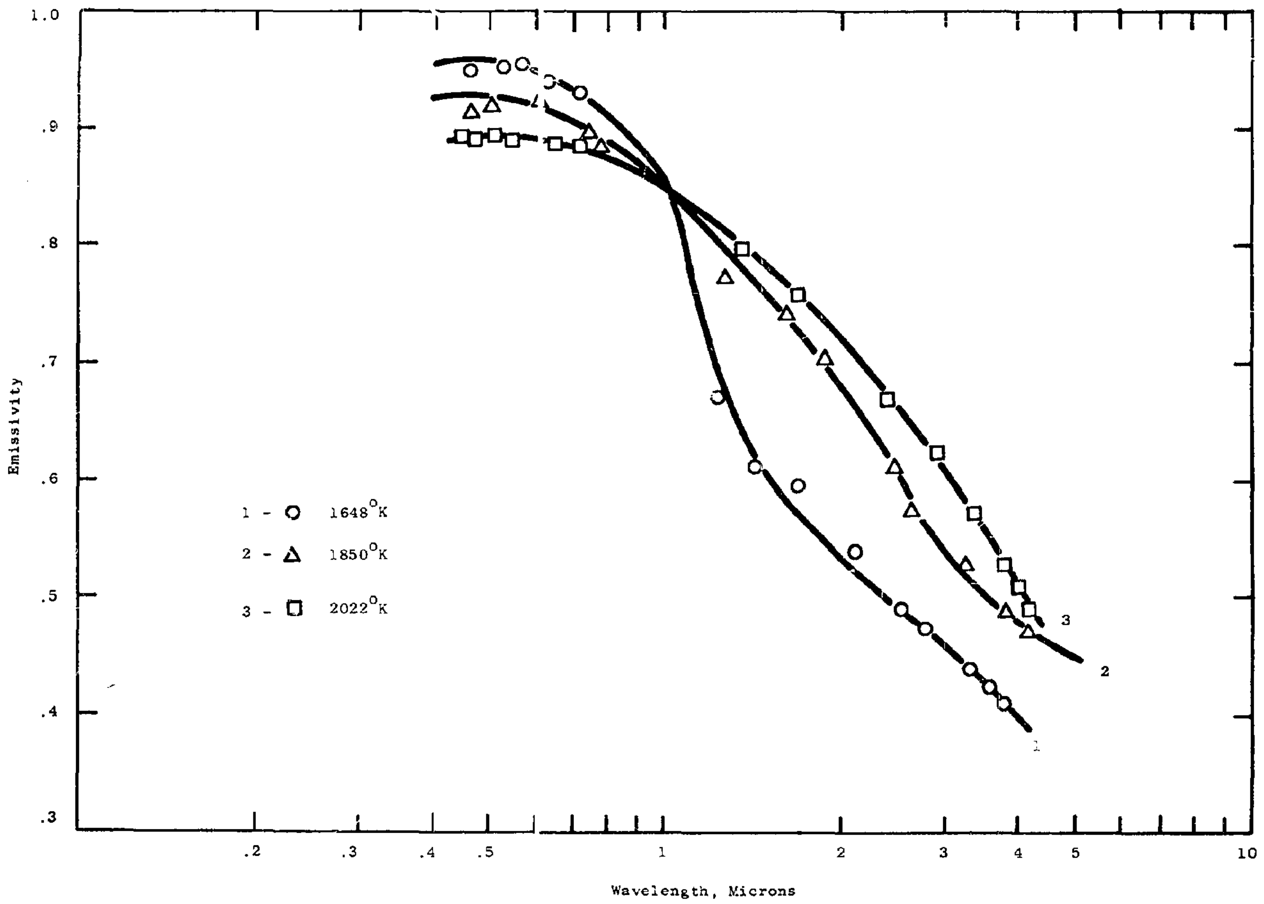

Figure 55. Normal Spectral Emissivity - TiB_2 (Specimen 2)

c. X-ray Diffraction Studies - TiB_2

X-ray measurements were made on the two specimens on TiB_2 used for emissivity determinations. Table 34 gives the x-ray pattern of the surface of specimen 1 before and after heating in the argon atmosphere to 2022°K.

Table 34

X-RAY DIFFRACTION PATTERN TiB_2

Specimen 1 - Before Heating

I/I_o	d,Å Measured	Impurity Lines	ASTM d-Values	hkl
60	3.23	NONE	3.22	001
50	2.63		2.62	100
100	2.03		2.03	101
5	1.62		1.61	002
5	1.51		1.51	110
30	1.38		1.37	102
20	1.21		1.21	201
10	1.10		1.10	112
10	.996		.995	103
5	.948		.948	211
5	.845		.845	212

Specimen 1 - After Heating

I/I_o	d,Å Measured	Impurity Lines	ASTM d-Values	hkl
100	3.26	TiO_2	3.25	110
20	2.49	TiO_2	2.49	101
5	2.30	TiO_2	2.30	200
10	2.19	TiO_2	2.19	111
20	2.04	TiO_2	2.05	210
30	1.69	TiO_2	1.69	211
5	1.63	TiO_2	1.62	220
2	1.48	TiO_2	1.48	002
3	1.45	TiO_2	1.45	310
5	1.36	TiO_2	1.36	301
3	1.34	TiO_2	1.35	112

The lattice "d" spacings measured on this specimen were characteristic of TiB_2 before heating and TiO_2 after heating, indicating that oxidation (through leakage) of the specimen took place while the specimen was at elevated temperature. This was not observable when viewing the specimen with an optical pyrometer during temperature measurement up to 1800°K but at 2000°K a change in surface structure became apparent. X-ray patterns of Specimen #2 gave "d" spacing characteristic.

of TiB_2 before and after measuring emissivity indicating that the specimen remained compositionally stable up to 2022°K.

d. Weight and Density - TiB_2

Weight and density are given in Table 35 for TiB_2. No final measurements were made on Specimen 1 after emissivity measurement because of specimen oxidation.

Table 35

WEIGHT AND DENSITY - TiB_2

Weight - gms.	Before	After	Change
Specimen 1	.8472	oxidized	---
Specimen 2	1.7389	1.7344	-.0045
Density - gms/cc			
Specimen 1	4.3	oxidized	---
Specimen 2	4.3	4.5	+.2

Carborundum Company reports a density of 4.20-4.29. Literature reports 4.5 and 4.2 (5,7).

A loss of weight of 0.2% coincident with a gain of 4% in density indicates that additional densification of TiB_2 takes place during prolonged heating. Inspection of the electron micrographs, Figures 51 and 52 showing the structure before and after heating, would support this theory.

e. Normal Spectral Emissivity - TiB_2

Emissivity measurements were made on TiB_2 specimen 1 at 1573°K, 1813°K and 2021°K, and Figure 53 shows plots of emissivity as a function of wavelength. At 1573°K emissivity starts at a high value of 0.97 at 0.4μ and drops to 0.6 at 4μ. At 1813°K the rate of change of emissivity with increasing wavelength is about the same as that obtained for 1573°K and 2021°K. While emissivity decreases with increasing temperature at the short wavelength, no typical crossover point, where emissivity is independent of temperature, is indicated. This is believed to be the result of surface oxidation taking place during measurement as was confirmed by the x-ray analysis, given in Table 34. Emissivity measurements were then run on TiB_2 specimen 2, after the cause of oxidation in the specimen chamber was corrected. Only data on specimen 2 is subsequently discussed. Figure 54 is a plot of four determinations of emissivity vs. wavelength at 1648°K. At wavelengths between 0.45μ and 0.75μ emissivity is above 0.9. It then decreases rapidly and drops to 0.38 at 4.5μ. Figure 55 shows curves for emissivity at 1648°K, 1850°K and 2022°K. The difference in slope at the two higher temperatures relative to the 1648°K curve is believed to be due to dynamic changes in surface structure as indicated in the before and after electron micrographs, Figure 51 and 52 respectively.

Table 36 gives values of normal total emissivity for TiB_2 calculated from spectral data plotted in Figure 55.

Table 36

NORMAL TOTAL EMISSIVITY - TiB_2 (SPECIMEN 2)

Temperature °K	ε_{nt}
1648	.48
1850	.59
2022	.66

Figure 31 and Figure 56 are plots of the above data showing the rate of change of normal emissivity to be positive with respect to temperature and equal to 0.60 x 10^{-3} per °K respectively. Figure 57 shows the variation of normal spectral emissivity, with temperature at constant wavelength and Figure 58 shows the temperature coefficient of emissivity $\frac{\partial \varepsilon}{\partial T}$ as a function of wavelength. It changes from negative to positive at 1 micron.

4. Zirconium Nitride - ZrN

This compound is a crystalline material possessing a cubic structure and an x-ray theoretical density of 7.349 gms/cm^3. Its hardness is +8(5). Dissociation appears to take place at temperatures in excess of 1700°K forming lower nitrogen containing compounds. The melting point is reported to be 2930°C (5).

a. Chemical Analysis - ZrN

The theoretical composition of ZrN is 13.3% nitrogen and 86.7% zirconium. Table 37 given the results of composition determination of the specimens on which emissivity measurements were made. There is 2% oxygen in the specimen but x-ray diffraction analysis did not disclose the presence of a ZrO_2 phase before heating. Generally the overall composition shows enough deviation from pure ZrN to render the measured spectral emittance properties as being specific to specimen composition and not conclusively the essential radiation characteristic of ZrN.

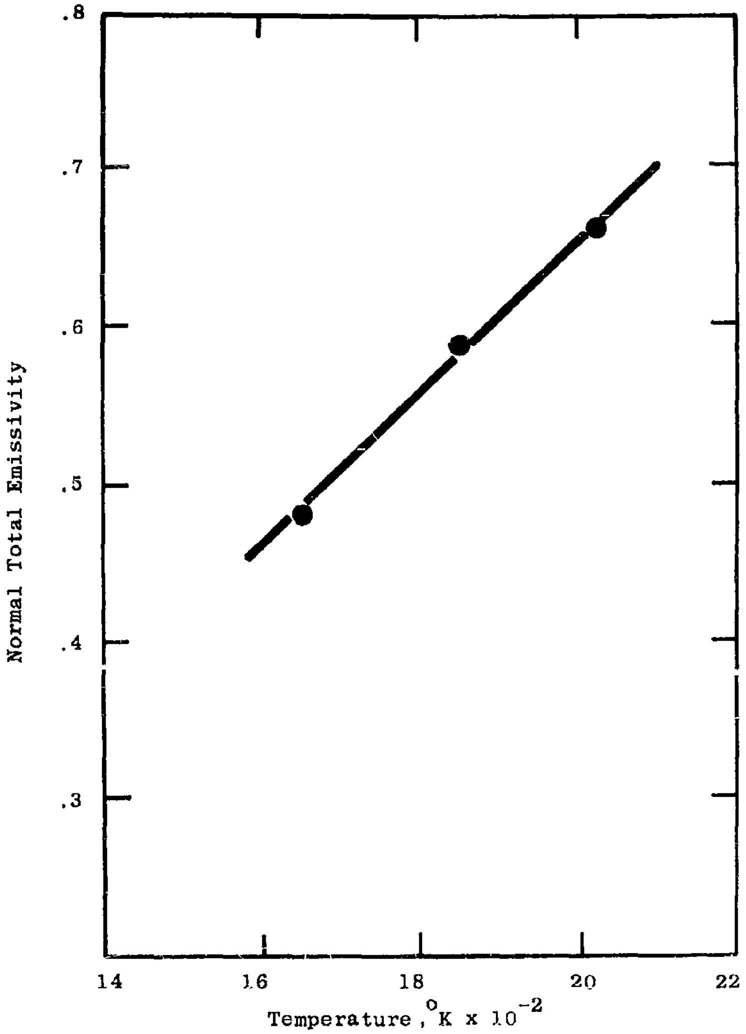

Figure 56. Normal Total Emissivity-TiB_2, Specimen 2

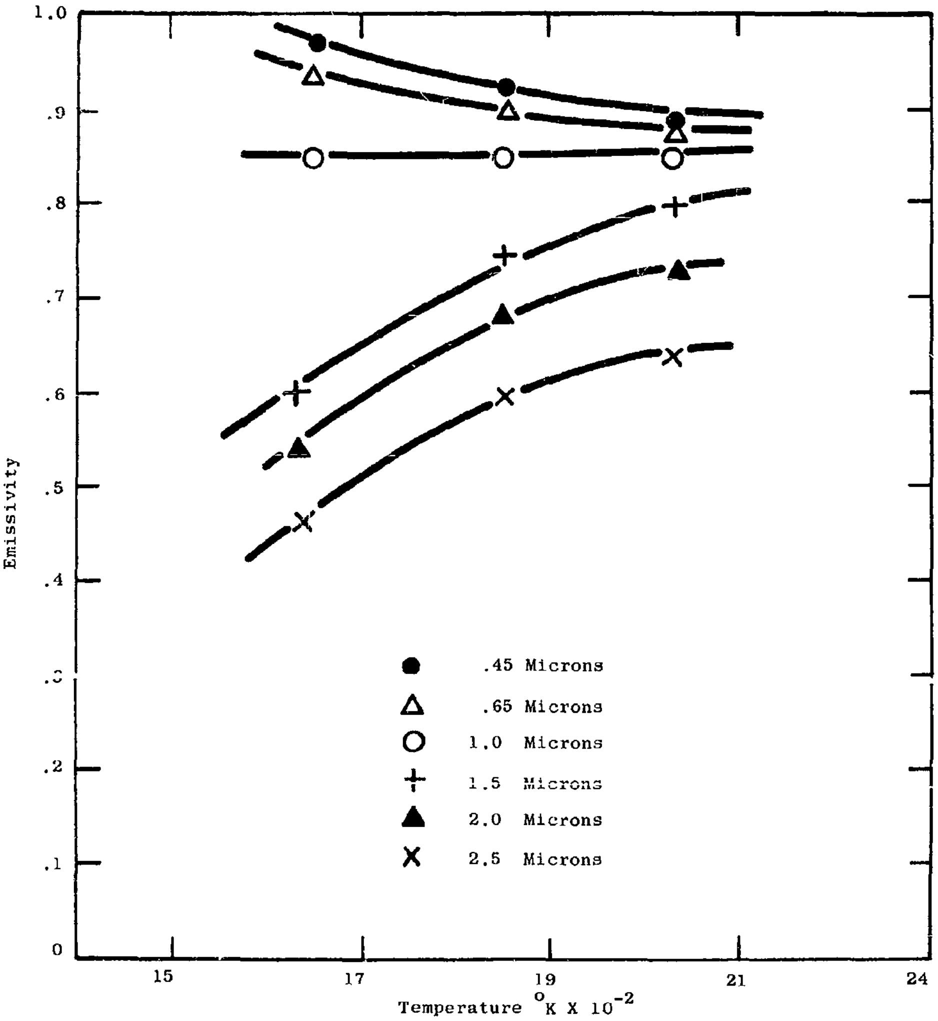

Figure 57. Temperature Dependence of Emissivity - TiB_2, Specimen 2

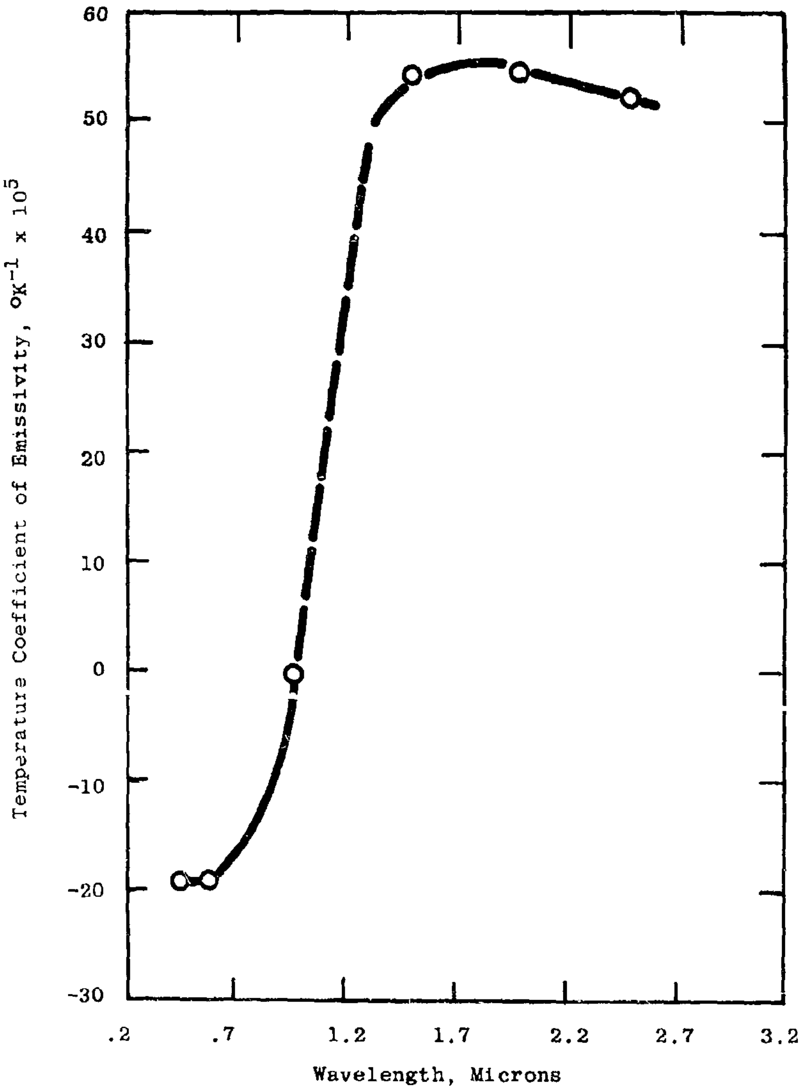

Figure 58. Temperature Coefficient of Emissivity-TiB_2, Specimen 2

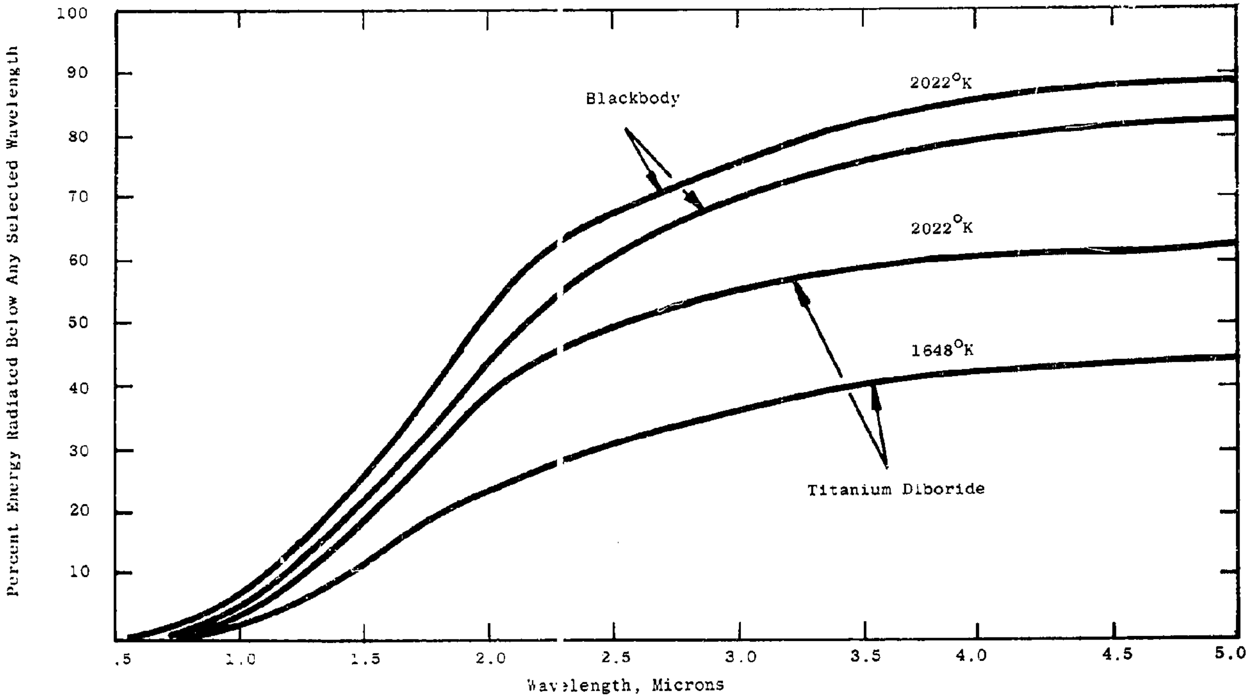

Figure 59. Relative Radiant Energy - TiB_2, Specimen 2

Table 37

CHEMICAL ANALYSIS - ZIRCONIUM NITRIDE

Zirconium		85.42%	Magnesium	ND	5 PPM
Nitrogen		11.08%	Manganese		5 PPM
Hafnium		2.5% (estimated)	Molybdenum	ND	10 PPM
Oxygen		2%	Sodium		30 PPM
Silver	ND	5 PPM	Columbium	ND	100 PPM
Aluminum		300 PPM	Nickel		10 PPM
Arsenic	ND	100 PPM	Lead	ND	10 PPM
Boron	ND	10 PPM	Antimony	ND	50 PPM
Barium	ND	10 PPM	Silicon		10 PPM
Beryllium	ND	10 PPM	Tin	ND	10 PPM
Bismuth	ND	10 PPM	Strontium	ND	10 PPM
Calcium		600 PPM	Tantalum	ND	500 PPM
Cadmium	ND	10 PPM	Tellurium	ND	100 PPM
Cobalt	ND	10 PPM	Thallium	ND	10 PPM
Chromium		100 PPM	Titanium		40 PPM
Copper	ND	10 PPM	Vanadium	ND	10 PPM
Iron		1300 PPM	Tungsten	ND	500 PPM
Germanium	ND	10 PPM	Zinc	ND	50 PPM
Indium	ND	10 PPM	Potassium		40 PPM
Lithium	ND	10 PPM			

NOTE:

ND = not detected, less than

PPM = parts per million

b. Surface Characteristics - ZrN

Figure 60 is a photomicrograph at 300x of the polished surface of the zirconium nitride specimen showing a somewhat granular structure. Etching the specimen brings out the same structure with greater contrast as is shown in Figure 61. After heating to 2287°K the surface shown in Figure 62 appears to have developed fine cracks with the grains breaking up into smaller crystallites. Figure 63 is an electron micrograph at 72,000x magnification of etched ZrN surface before making emissivity measurements up to 2287°K. Some ill-defined grain boundaries are distinguishable but in general, it appears to contain a multiplicity of dislocation etch pits. Figure 64 is a view of the surface after heating to 2287°K showing typical thermal etching and well defined grain boundaries. Slip planes are visible on some crystal surfaces. From this dynamic transition in surface structure, it is felt that a random attenuation of emissivity in the direction of higher values would be induced. Figure 65, showing values of emissivity plotted as a function of wavelength and temperature, appears to substantiate this conclusion.

c. X-ray Diffraction Studies - ZrN

X-ray diffraction patterns were measured on the ZrN specimen for which emissivity data are presented. When the specimen was removed from the specimen chamber a change in color from a greyish yellow to a metallic color was observed. This was interpreted as a possible change in surface composition. However, the specimen indexed to be ZrN when x-rayed, with lines of ZrO_2 showing up. No ZrO_2 lines were observed in the specimen before making emissivity measurements. Table 38 gives the "d" spacings in Ångstroms, relative intensity, and Miller indices before and after measurement. Only the lines given for ZrN were present before heating the specimen.

Table 38

X-RAY DIFFRACTION PATTERN - ZrN SPECIMEN, BEFORE AND AFTER HEATING

I/I_o	d,Å Measured	Impurity Lines	ASTM d-Values	hkl
80	2.64		2.64	111
100	2.29		2.29	200
90	1.62		1.62	220
40	1.38		1.38	311
5	1.14		1.14	400
10	1.05		1.05	301
10	1.02		1.02	420
30	.935		.935	422
30	.882		-	-
100	2.92	*ZrO_2 (cubic)	2.92	111
60	2.53	"	2.53	200
100	1.80	"	1.80	220
100	1.53	"	1.53	311

---

* ZrO_2 lines present only after heating; strong ZrN pattern present both before and after heating.

Figure 60. Polished ZrN - 300X

Figure 61. Etched ZrN - 300X

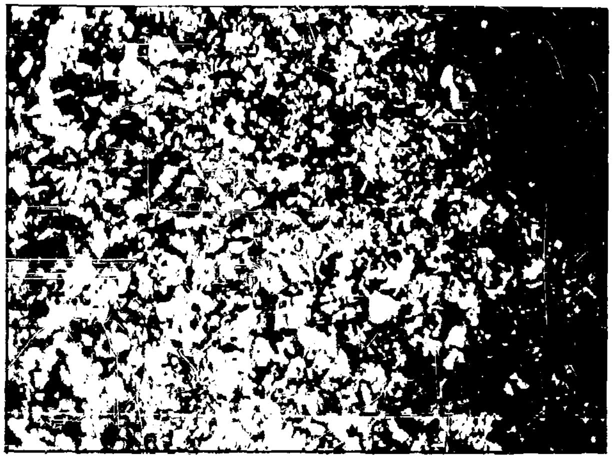

Figure 62. ZrN After Heating to 2287°K - 300X

Figure 63. ZrN Before Heating - 72000X

Figure 64. ZrN After Heating to 2287°K - 72000X

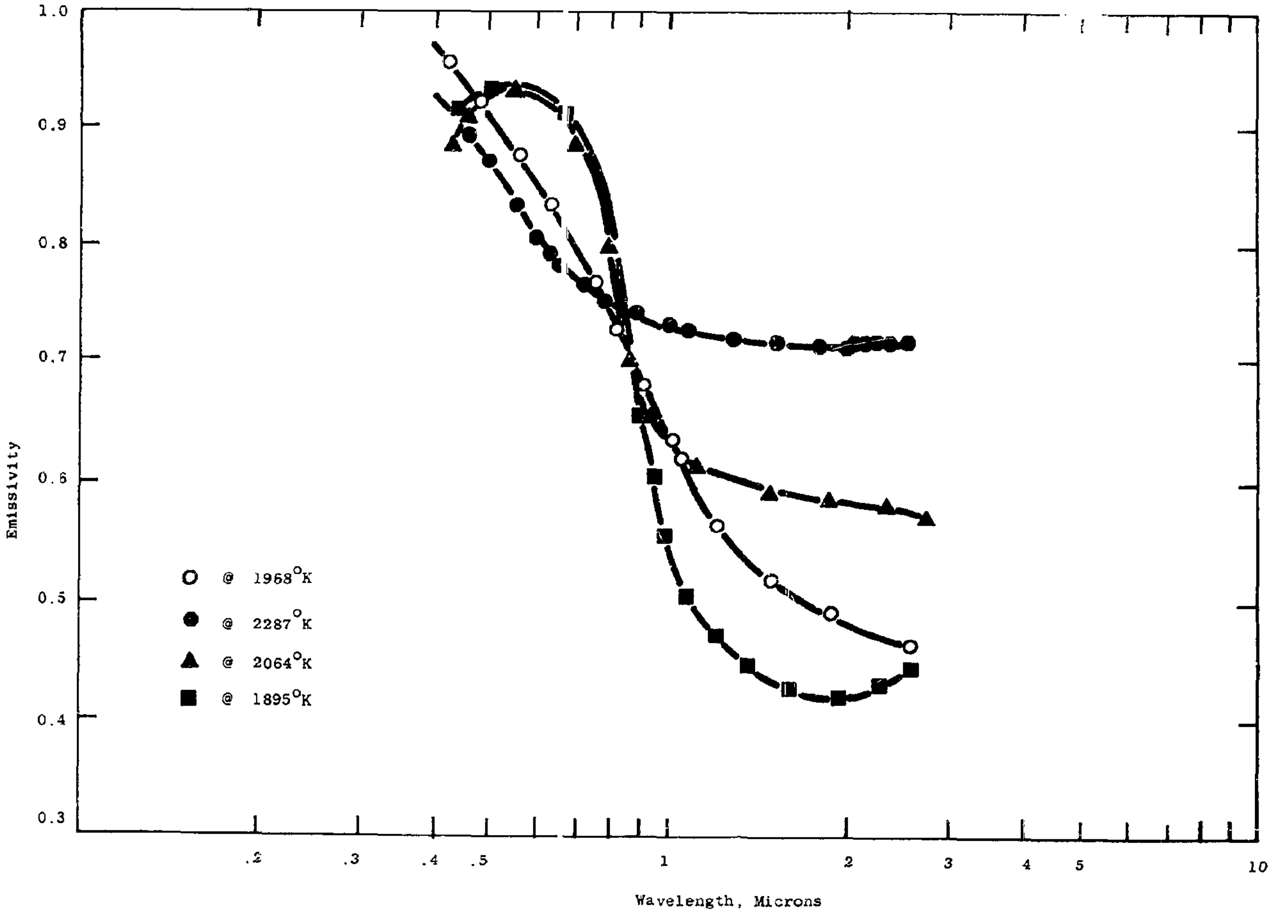

Figure 65. Normal Spectral Emissivity - ZrN Specimen

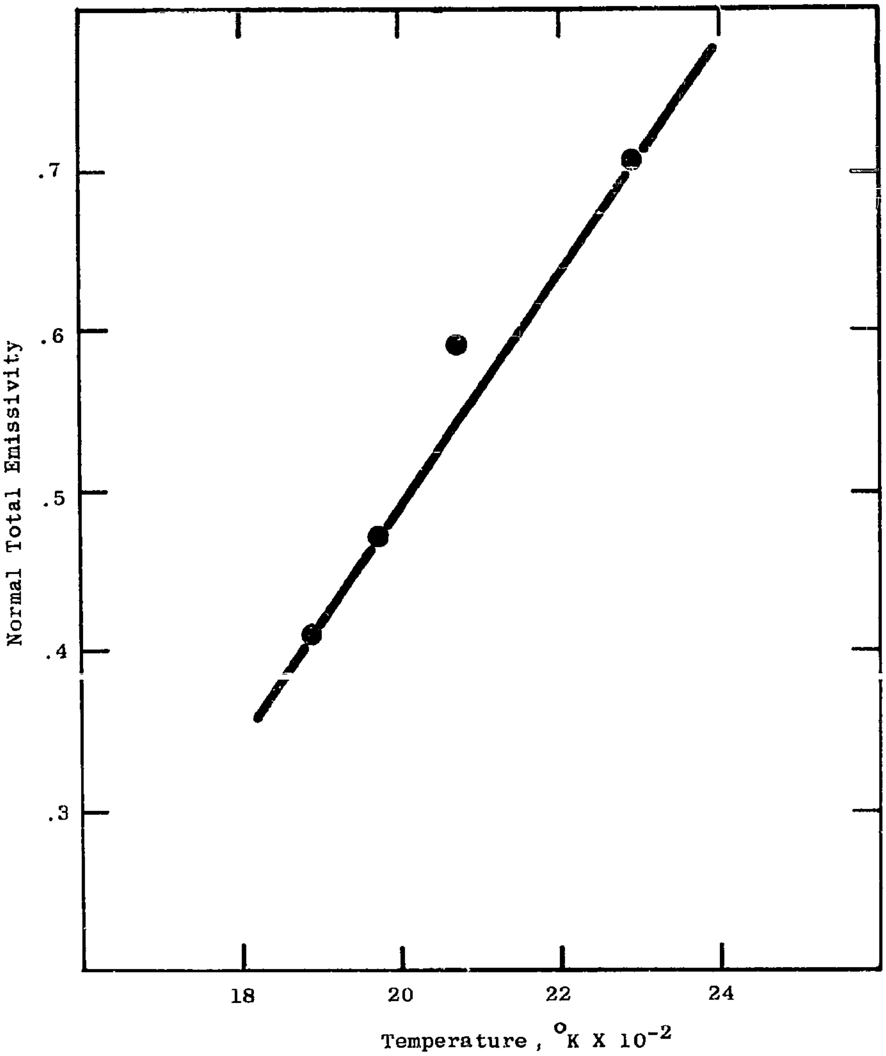

Figure 66. Normal Total Emissivity - ZrN Specimen

d. Weight and Density - ZrN

Weight and density measurements were run before and after measuring emissivity up to 2287°K. Table 39 gives values.

Table 39

WEIGHT AND DENSITY - ZrN

	Before	After	Change
Weight-gms.			
	2.8063	2.8096	+.0073
Density-gms/cc			
	6.904	6.450	-.454

Carborundum reports a density of 6.95. Literature reports 7.35 and 7.32 references (5) and (7) respectively.

The increase in weight confirms the x-ray finding that slight oxidation of the specimen took place during measurement. The decrease in density is attributed to an increase of specimen volume coincident with oxidation.

e. Normal Spectral Emissivity - ZrN

Emissivity measurements were made on the ZrN specimen, the composition of which appears in Table 38, in an argon atmosphere at 1895°K, 1968°K, 2064°K and 2287°K. Figure 65 gives the wavelength dependence of emissivity out to 3 microns. Attempts were made to make measurements at lower temperatures but difficulty was encountered in that the radiant energy output signal strength was low in the infrared and at maximum amplifier gain the noise to signal ratio was high. Low values of emissivity beyond 1 micron can be seen by referring to the 1895°K and 1965°K curves in Figure 65. The rapid increase in emissivity with temperature, in the infrared, is believed to be caused by changes in surface structure and oxide contamination rather than being essential to ZrN. This is shown in Figure 67 which relates the temperature dependence of emissivity at constant wavelength. This family of curves also indicates that an emissivity of about 0.78 is independent of temperature, in the wavelength region of 0.7 micron.

Table 40 lists values of normal total emissivity, calculated from spectral data presented in Figure 65 and is shown plotted in Figure 66. The rate of change of normal total emissivity with respect to temperature calculates to be 0.7×10^{-3} units per degree K which is higher than for the borides previously described. Temperature coefficient of emissivity as a function of wavelength is shown in Figure 68 as calculated from data presented in Figure 67.

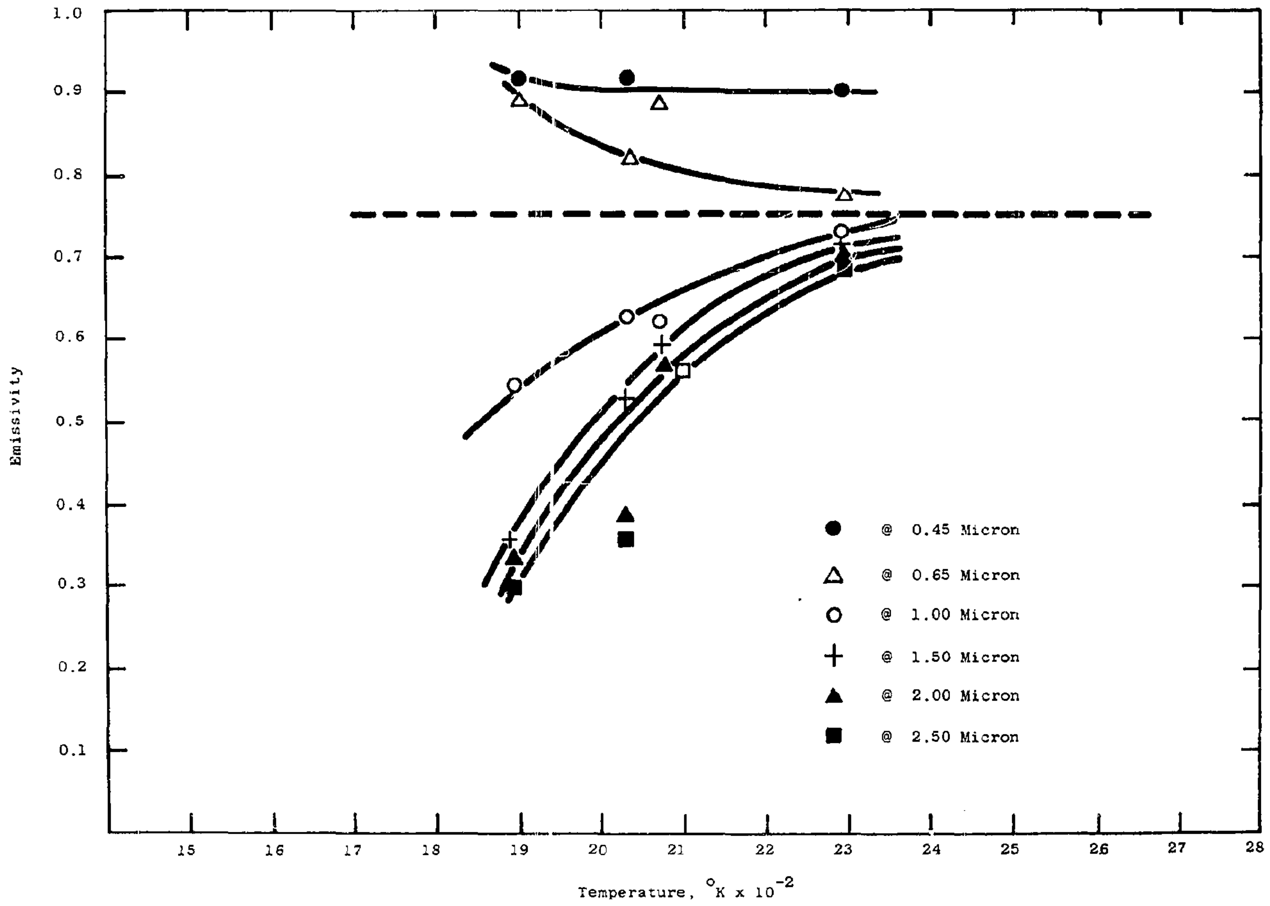

Figure 67. Temperature Dependence of Emissivity - ZrN Specimen

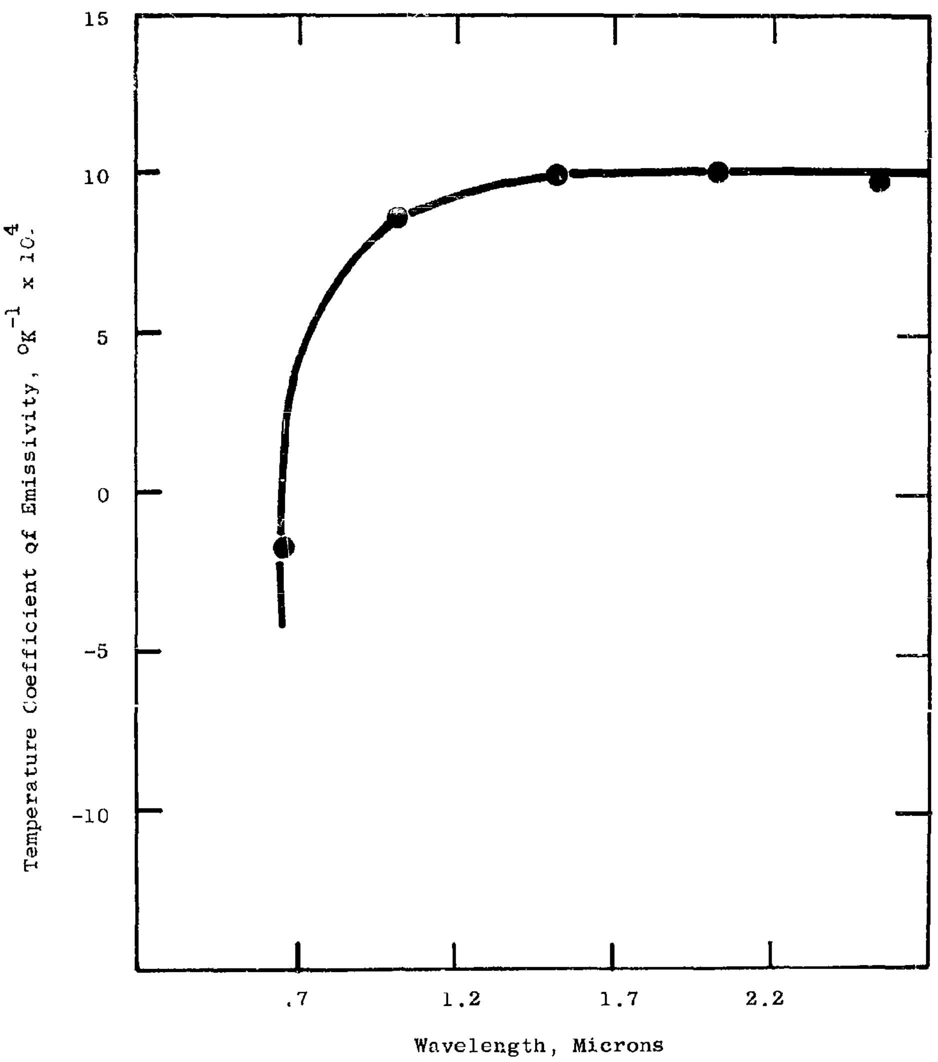

Figure 68. Temperature Coefficient of Emissivity-ZrN Specimen

Table 40

NORMAL TOTAL EMISSIVITY - ZrN SPECIMEN

Temperature °K	Total Normal Emissivity
1895	.43
1968	.47
2064	.59
2287	.71

Figure 69 shows the plot of the summation of percent energy radiated from ZrN below a selected wavelength for the two temperatures of 1895°K and 2287°K compared to a black body at the same temperature.

5. Tantalum Nitride - TaN

Tantalum nitride is a crystalline material possessing a hexagonal structure that is close-packed and has a reported Mohs hardness of + 8. There has been presented experimental evidence indicating that the composition of tantalum nitride is actually Ta_2N (9). Tantalum nitride has a reported melting point of 2890°C.

a. Chemical Analysis - TaN

Table 41 gives results of chemical analysis of the specimen on which emissivity measurements were made. The theoretical composition is 92.3% tantalum while analysis gives a specimen composition of 95.84% tantalum and 3.53% nitrogen. The presence of 0.19% iron, 0.2% molybdenum and 0.12% vanadium is believed to have no major effect on the emissivity. However the low nitrogen content, in terms of a TaN formula (4.2% below theoretical) indicates an excess of 4.2% free tantalum and may substantially modify emissivity from that essential to the TaN composition.

b. Surface Characterization - TaN

Figures 70 and 71 are views at 300x magnification of the polished and etched surface, respectively, of the second specimen of tantalum nitride before making emissivity measurements. No photomicrographs of the first specimen are shown.

There is evidence of porosity even though density measurements indicate a compact densified structure. Figure 72 shows the surface of

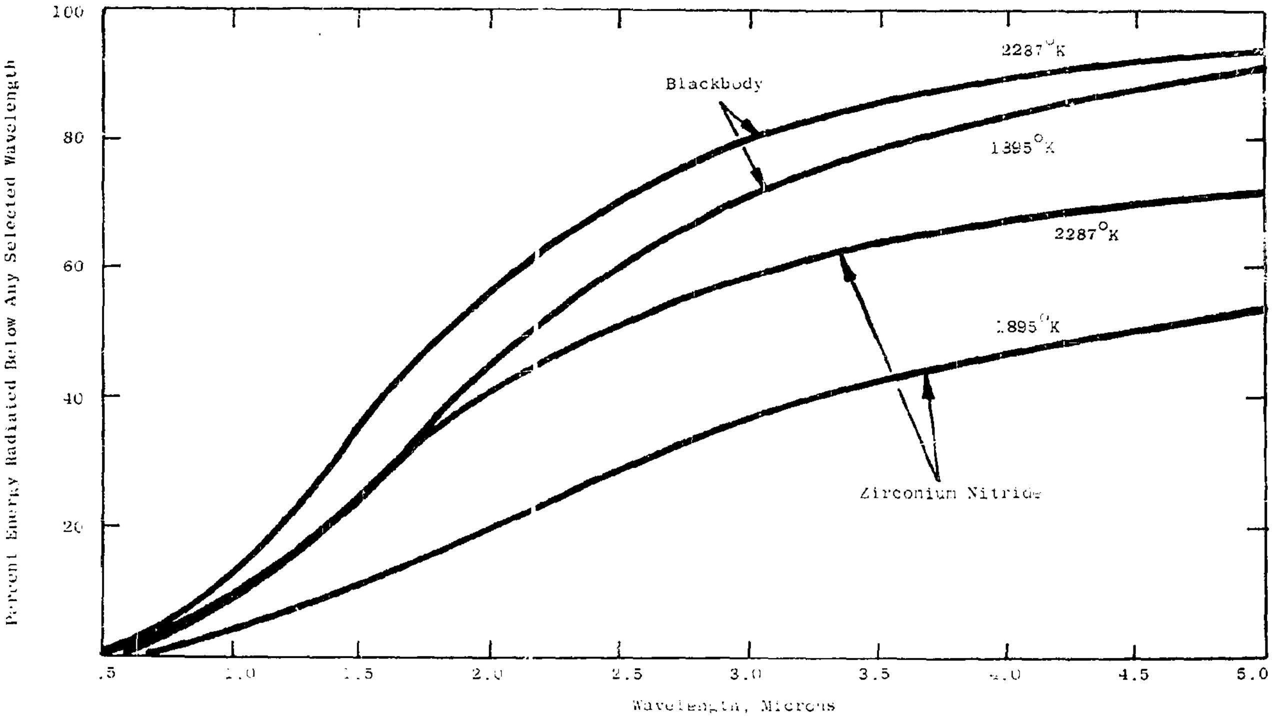

Figure 69. Relative Radiant Energy - ZrN Specimen

Figure 70. Polished TaN - 300X

Figure 71. Etched TaN - 300X

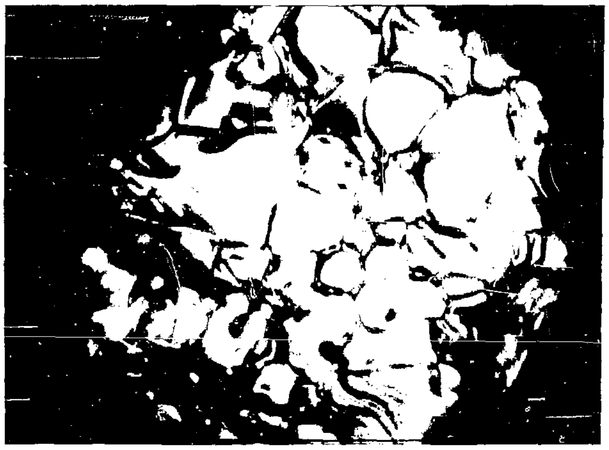

Figure 72. TaN After Heating to 2138°K - 300X

the specimen after heating to 2138°K in an atmosphere of purified nitrogen. In this case the specimen formed a polycrystalline layer wherein the inter-crystalline boundaries had disintegrated leaving a loose coating of granular crystals on the surface. It was found not possible to replicate this surface to make electron micrographic observations. Figure 73 is an electron micrograph at 72000X magnification of the etched surface before heating to 2138°K. Here can be seen a well defined crystal structure showing the hexagonal structure with grain boundaries intersecting at 120° angles. Figure 74 is an electron micrograph at 72000X magnification of the same specimen after heating to 2138°K. Before the surface could be replicated, it was necessary to wipe it with lens paper in order to remove the granular powder previously mentioned. The powder was reserved for x-ray analysis. The definite white areas are an excellent view of etch pits along grain boundaries. These intersect at an angle of 120° indicating the retention of an hexagonal structure of TaN. X-ray analyses were made of this surface confirming the TaN composition.

Table 41

CHEMICAL ANALYSIS - TaN

Tantalum		95.84%	Magnesium		50 PPM
Nitrogen		3.53%	Manganese		5 PPM
Silver	ND	5 PPM	Molybdenum		2000 PPM
Aluminum		70 PPM	Sodium		20 PPM
Arsenic	ND	100 PPM	Columbium		300 PPM
Boron	ND	10 PPM	Nickel		40 PPM
Barium	ND	10 PPM	Lead	ND	10 PPM
Beryllium	ND	10 PPM	Antimony	ND	50 PPM
Bismuth	ND	10 PPM	Silicon		20 PPM
Calcium		50 PPM	Tin	ND	10 PPM
Cadmium	ND	10 PPM	Strontium	ND	10 PPM
Cobalt	ND	10 PPM	Tellurium	ND	100 PPM
Chromium		70 PPM	Thallium	ND	10 PPM
Copper	ND	10 PPM	Titanium		600 PPM
Iron		1900 PPM	Vanadium		1200 PPM
Germanium	ND	10 PPM	Tungsten		500 PPM
Hafnium	ND	100 PPM	Zinc	ND	50 PPM
Indium	ND	10 PPM	Zirconium	ND	50 PPM
Lithium	ND	10 PPM	Potassium		20 PPM

NOTE: ND = not detected, less than

PPM = parts per million

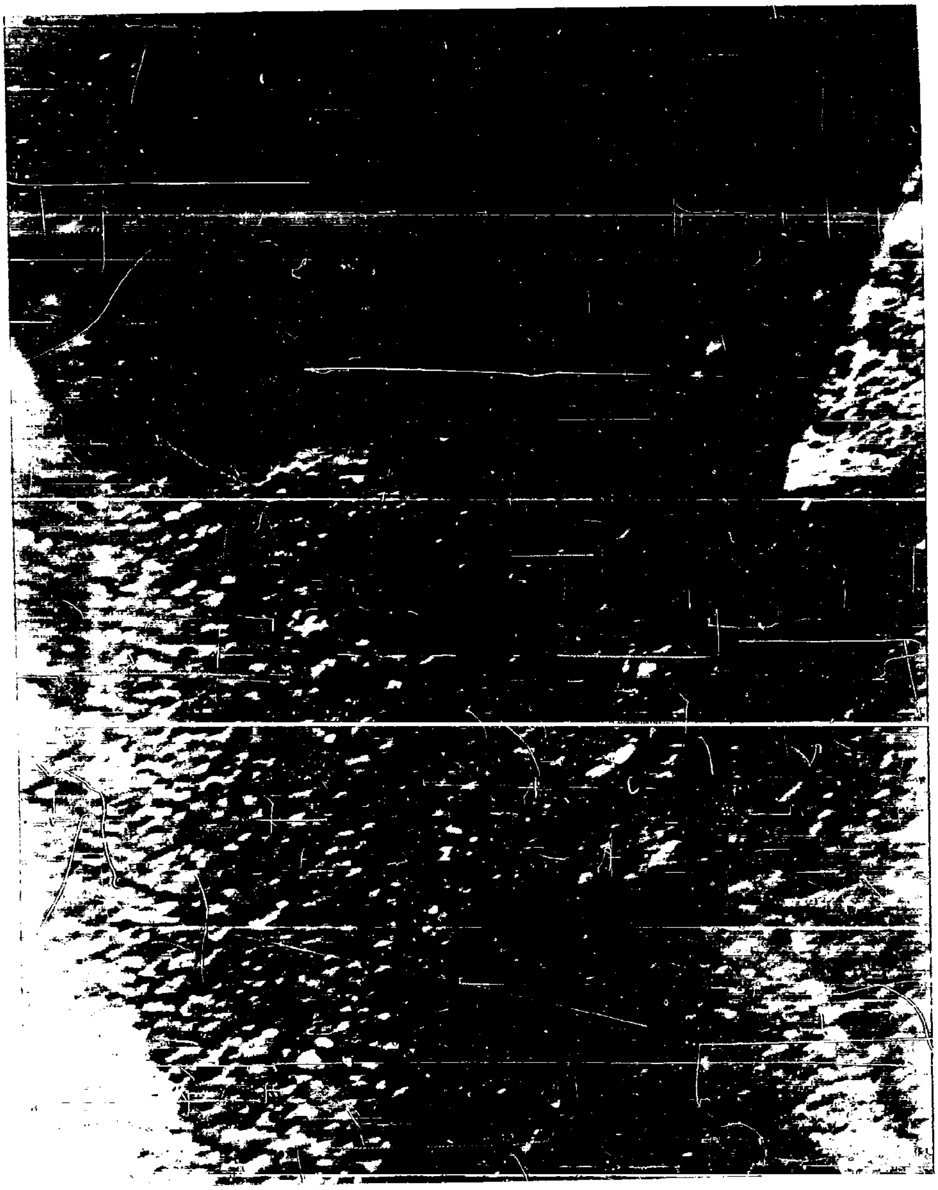

Figure 73. Etched TaN Before Heating - 72000X

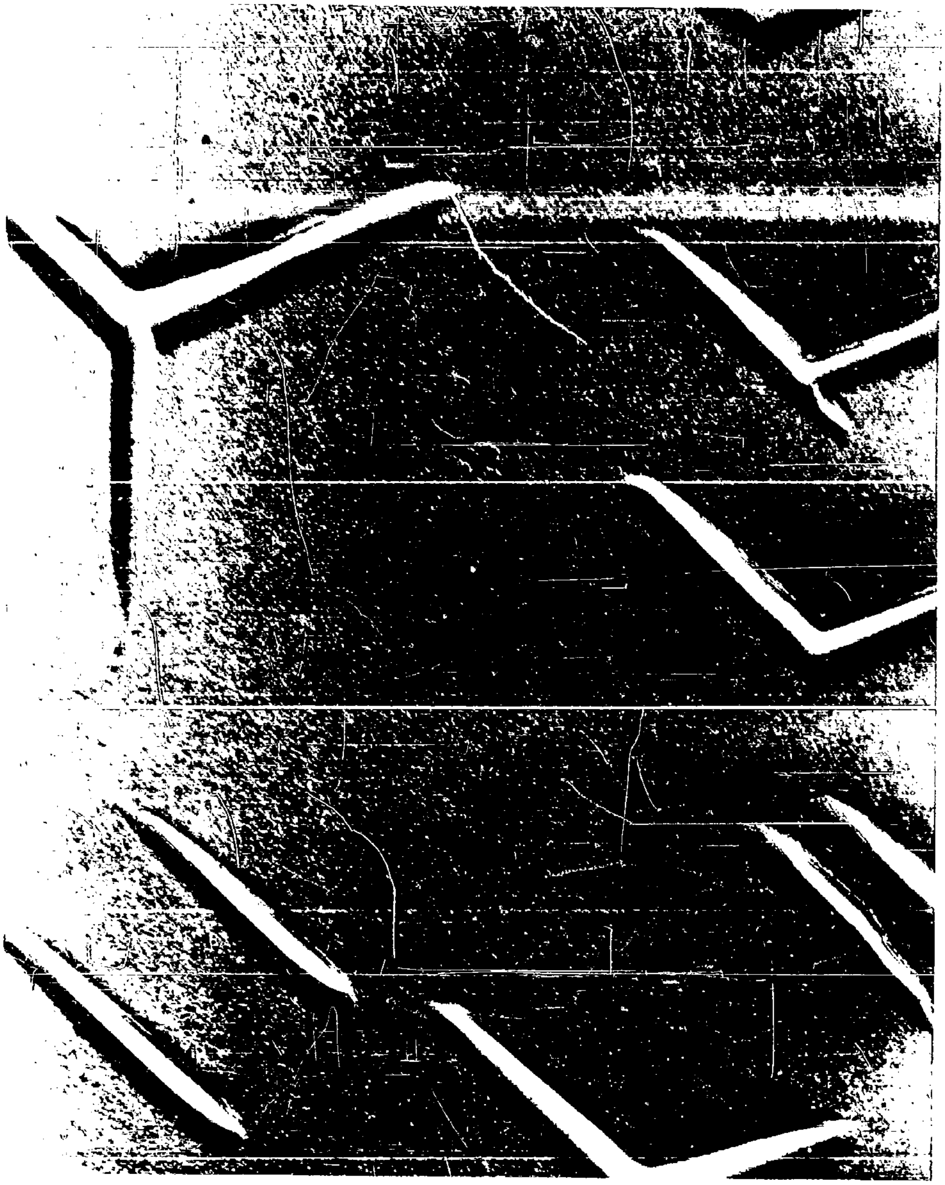

Figure 74. TaN After Heating to 2138°K - 72000X

c. X-ray Diffraction Studies - TaN

X-ray diffraction patterns were established for the two specimens on which emissivity measurements were made. Table 42 gives the relative peak height intensities (I/I_o) and "d" spacings observed for each specimen before heating. The values are characteristic to TaN.

Table 42

X-RAY DIFFRACTION PATTERN - TaN

Specimen 1 - Before Heating

I/I_o	d,Å Measured	Impurity Lines	ASTM d-Values	hkl
20	2.64	NONE	2.66	100
10	2.59*		2.57	110
15	2.47		2.47	002
5	2.44*		2.42	101
100	2.33		2.34	101
25	1.81		1.80	102
75	1.78*		1.77	201
10	1.52*		1.52	300
5	1.46		1.46	121
15	1.39		1.39	103
15	1.29		1.30	112
15	1.27		1.27	201
5	1.16		1.16	202
10	1.03		1.03	203
5	.998		.999	210
10	.978		.980	211
10	.925*		.930	141
5	.902		.907	204
20	.845		.858	213
5	.829		.824	006

* Cell parameters $a_o = 5.191$
$c_o = 2.911$

Table 43 gives the x-ray lines for Specimen 1 after heating to 2860°K in vacuum of 5×10^{-6} Torr. This pattern is characteristic of pure tantalum. It was therefore concluded that the thermal and vacuum environmental conditions under which emissivity measurements were made induced thermal dissociation of Specimen 1. Specimen 2, which was run in an atmosphere of nitrogen, formed a crystalline powder on the surface which when x-ray analyzed gave the pattern tabulated in Table 44. This is characteristic of a subnitride of tantalum and is believed to consist of TaN and Ta_2N phases. Some spacings remain unidentified.

Table 43

X-RAY DIFFRACTION PATTERN - TaN

Specimen 1 - After Heating

I/I_o	d,Å Measured	Impurity Lines	ASTM d-Values	hkl
25	2.58	TaN	2.57	110
100	2.33	Ta	2.34	110
10	1.35	Ta	1.39	211
40	1.16	Ta	1.16	220
75	.883	Ta	.883	321

Table 44

X-RAY DIFFRACTION PATTERN - TaN

Specimen 2 - After Heating

I/I_o	d,Å Measured	Impurity Lines	ASTM d-Values	hkl
10	3.30	NONE	-	-
20	2.65		2.66	100
5	2.57*		-	-
40	2.47		2.47	002
100	2.33		2.34	101
90	1.79		1.80	102
40	1.52		1.53	110
5	1.51*		-	-
5	1.46*		-	-
100	1.39		1.39	103
80	1.31		1.32	200
60	1.29		1.30	112
40	1.23		1.23	004
40	1.27		1.27	201
20	1.16		1.16	202
30	1.12		1.12	104
40	1.028		1.03	203
20	.995		.999	210
20	.976		.980	211
30	.960		.963	114
40	.928		.930	212
20	.902		.907	204
20	.879		.883	300
60	.853		.858	213
40	.828	Unidentified	-	-
5	.814	"	-	-

* Cell parameters $a_o = 5.191$
$c_o = 2.911$

X-ray diffraction pattern of the surface after removal of the polycrystalline surface powder gave lattice dimensions characteristic of TaN as listed in Table 42.

It was concluded that when tantalum nitride is taken to temperatures in excess of 2000°K in vacuum, dissociation to tantalum takes place at a slow rate. It was further concluded that when tantalum nitride, possessing a low nitrogen content, is heated at high temperature in an atmosphere of nitrogen, nitriding takes place with an associated disintegration of the surface into a polycrystalline powder.

d. Weight and Density

Measurements were made before and after emissivity determinations and Table 45 tabulates values.

Table 45

WEIGHT AND DENSITY

TaN

	Before	After	Change
Weight gms			
Specimen 1	3.7917	3.7891	-.0026
Specimen 2	6.0024	6.0259	+.0235
Density - gm/cc			
Specimen 1	14.9	14.9	.00
Specimen 2	14.36	14.17	-.19

Carborundum Company reports a density of 13.9 gms/cc. Literature reports (5) a density of 14.1 gms/cc.

Weight changes would substantiate that a loss of nitrogen was encountered in Specimen 1 and that nitriding took place in Specimen 2. Density of pure tantalum is 16.6 gms/cc.

e. Normal Spectral Emissivity - TaN

Spectral emissivity measurements were run on two specimens of TaN. The first specimen was heated in vacuum to 2000°K, for a period of 30 minutes to stabilize the surface, after which emissivity measurements were run at 2047°K, 2363°K, 2575°K and 2860°K.

Figure 75 shows the variation of emissivity with wavelength at these temperatures. Curve 5 gives the spectral emissivity of pure tantalum as reported in Ref. (2). From curves 1 and 2 it can be seen that the emissivity of tantalum nitride is 0.15 greater than pure tantalum between 0.4 micron and 0.8 micron (ref. (2)) and about 0.17 greater at 2 microns. As previously mentioned when this specimen was x-rayed the analysis showed that the specimen surface had converted to tantalum. TaN could be present up to 6% and go undetected.

Specimen 2 was placed in the emissometer in 2 atmospheres of purified nitrogen after degassing at 700°C in vacuum. Emissivity measurements were then run starting at lower temperatures of 1648°K, 1882°K, 1990°K and 2070°K, after thermal cycling to 2138°K. The emissivity is comparatively high relative to Specimen 1 being above 0.8 out to 1 micron as shown in Figure 76. After running emissivity at 1882°K the surface began to convert to a polycrystalline powder which has the effect of rendering emissivity independent of wavelength beyond 1.5 microns, i.e. the surface becomes a "grey body" at these wavelengths. Figure 77 is a plot of normal total emissivity as a function of temperature computed from spectral data presented in Figure 76. The ϵ_{nt} values are also tabulated in Table 46.

Table 46

NORMAL TOTAL EMISSIVITY - TaN SPECIMEN 2

Temperature °K	Total Normal Emissivity
1648	.72
1882	.72
1990	.74
2070	.73

Normal total emissivity for TaN is high and shows virtually no temperature dependence between 1648°K and 2070°K. Figure 78 is a plot of emissivity as a function of temperature at constant wavelength showing that within the bandwidth of from 0.45 micron to 3.5 microns only small changes are induced with changes in temperature. Figure 79 shows the percent energy radiated from TaN below any selected wavelength relative to a black body at the same temperature.

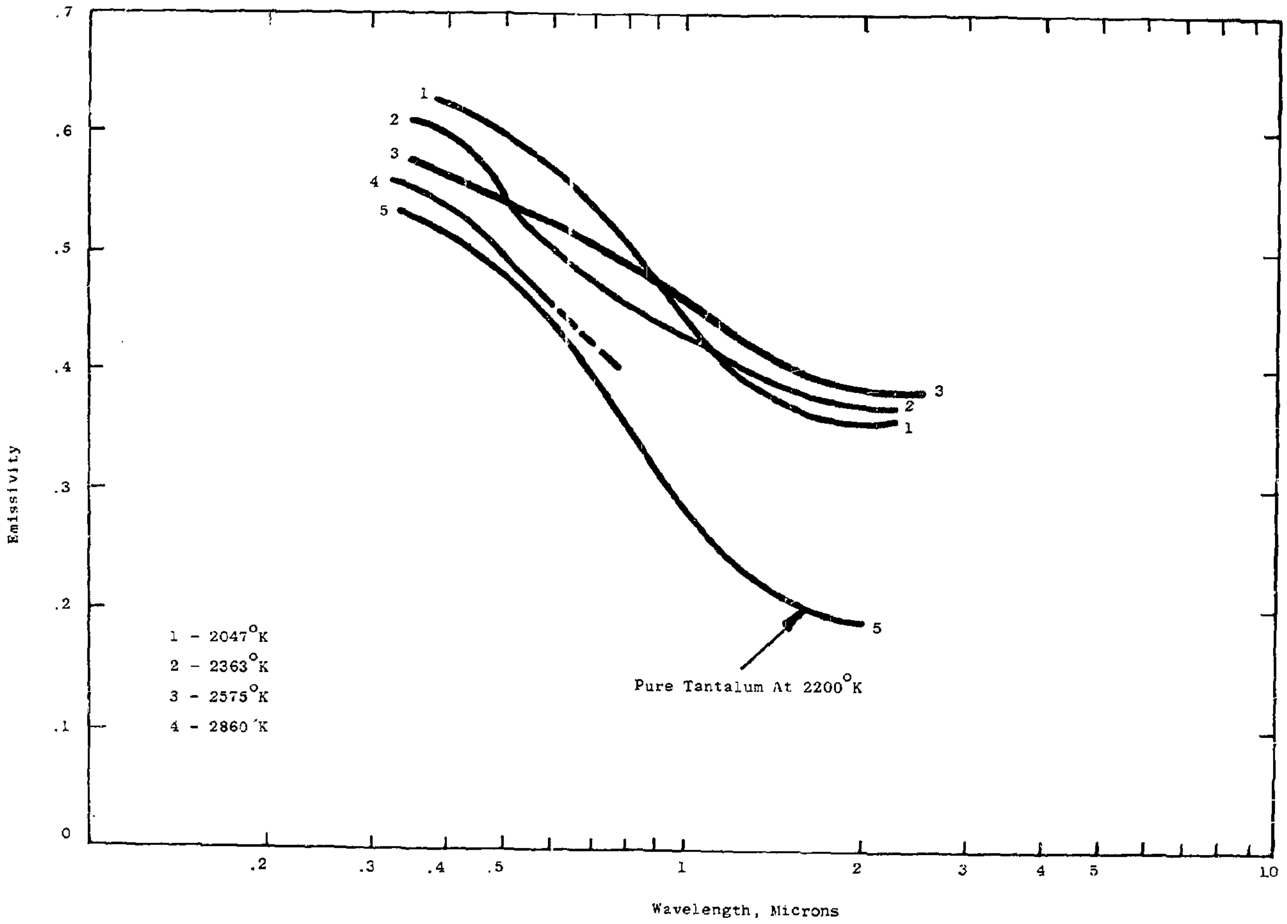

Figure 75. *Normal Spectral Emissivity - TaN (Specimen 1) in Vacuum*

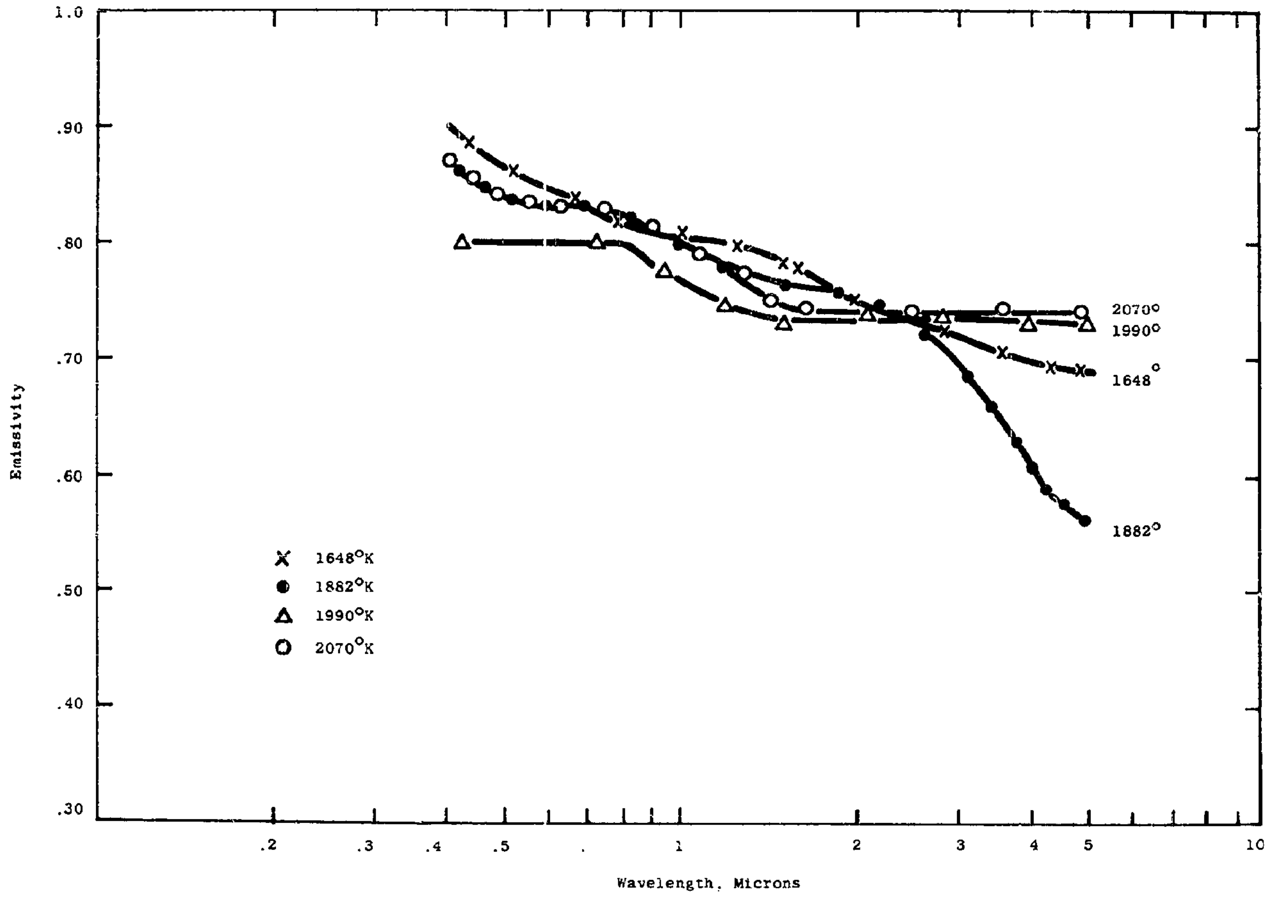

Figure 76. Normal Spectral Emissivity - TaN (Specimen 2) in Nitrogen (2 atm)

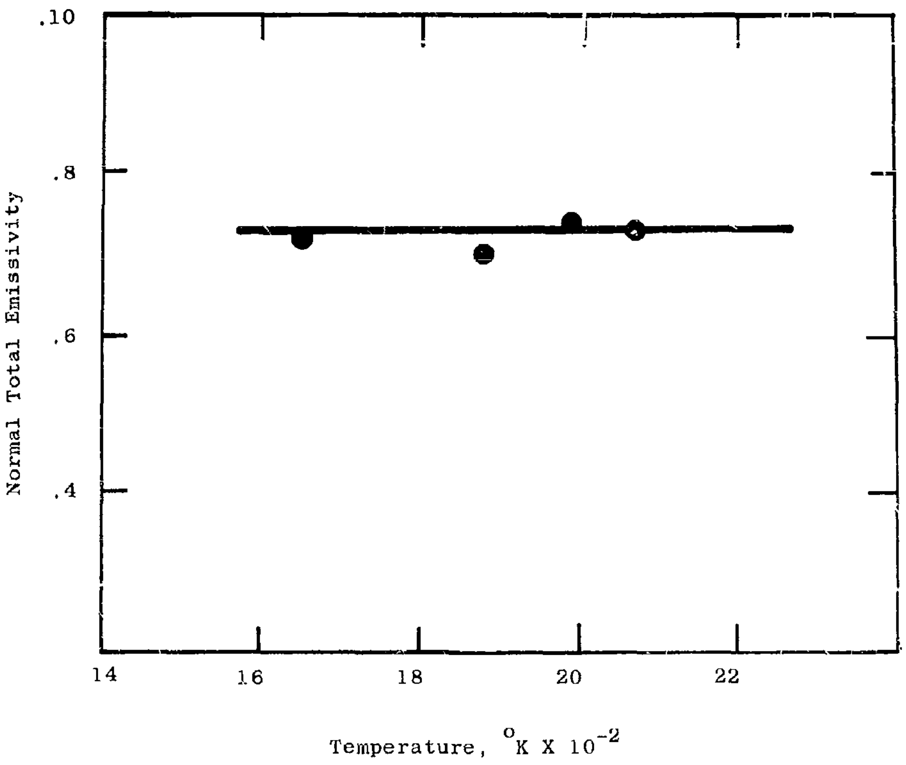

Figure 77. Normal Total Emissivity-TaN, Specimen 2

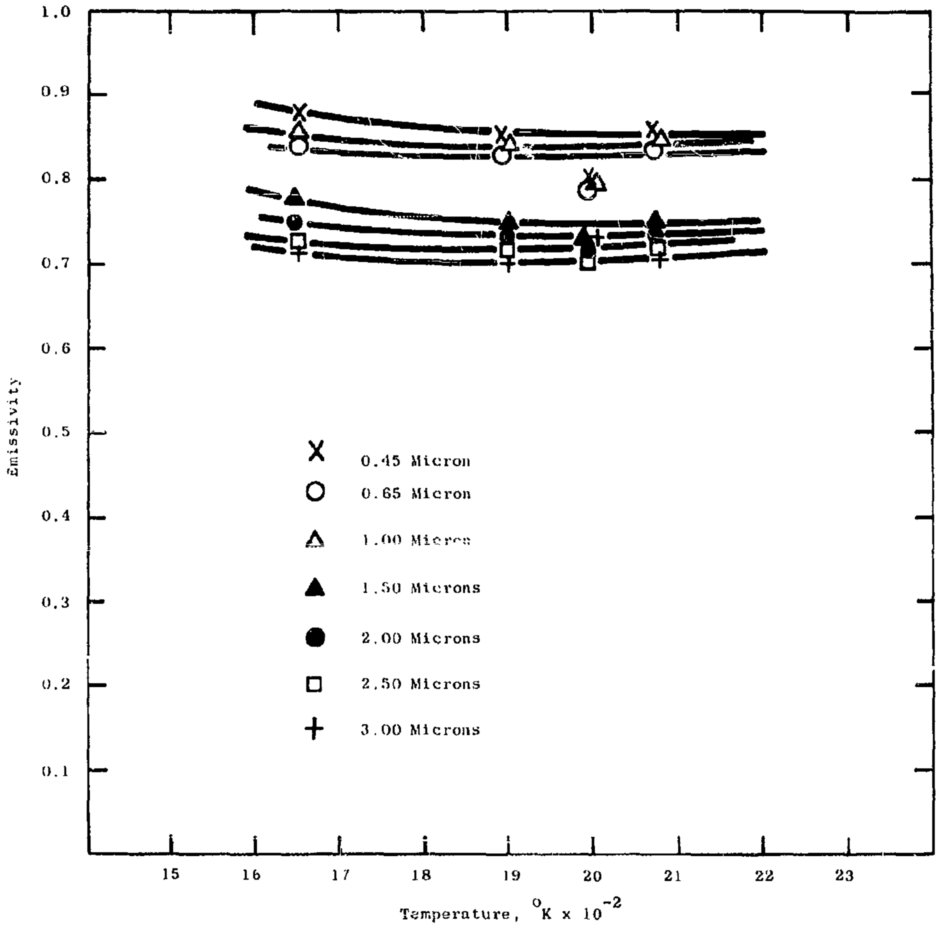

Figure 78. Temperature Dependence of Emissivity - TaN Specimen 2

6. Hafnium Nitride - HfN

Hafnium Nitride has a cubic crystalline structure and a Mohs hardness of +8 (3). Its melting point is reported to be 3310°C (3). Nitrogen is held both in molecular combination with hafnium and as an interstitial solid solution. The color is a grey-yellow similar to ZrN which changed to a metallic appearance on heating in an argon atmosphere as did ZrN.

a. Chemical Composition - HfN

Table 47 gives the chemical analysis of the hafnium nitride on which emissivity measurements were made. Theoretical composition is 92.72% hafnium and 7.28% nitrogen. Analysis shows a nitrogen content .82% less than theoretical relative to hafnium. However since the specimen also contains an estimated 2% to 4% zirconium it is assumed that part of the available nitrogen is in combination with zirconium. The specimen also contains 0.25% iron which is believed to have had no effect on spectral emittance properties. X-ray examination disclosed the presence of thorium.

b. Surface Characterization - HfN

Figures 80 and 81 show the structure of the polished and etched surface of hafnium nitride. There appears to be two phases present with localized concentration of one phase and a nucleation of crystals around it. Figure 82 is a view of the surface at 300X after heating to 2192°K. Figure 83 is an electron micrographic view at 72000X before running emissivity determinations. Here the surface shows no defined grain structure and appears to involve a multiplicity of ill-defined dislocations. Figure 84 shows an electron micrograph of the surface at 72000X after heating to 2192°K. Here the surface has become thermally etched showing a well defined cubic structure. Uniformly oriented slip planes are clearly visible on individual crystals.

c. X-ray Diffraction Studies - HfN

X-ray diffraction patterns were established on hafnium nitride before and after emissivity measurement up to 2192°K. Table 48 gives the line intensity I/I_o, and "d" spacings. Before the specimen was heated, the pattern was characteristic of HfN containing some lines indicative of the presence of thorium. After heating, there was evidence of some HfO_2 having formed. In addition lines for thorium were still present.

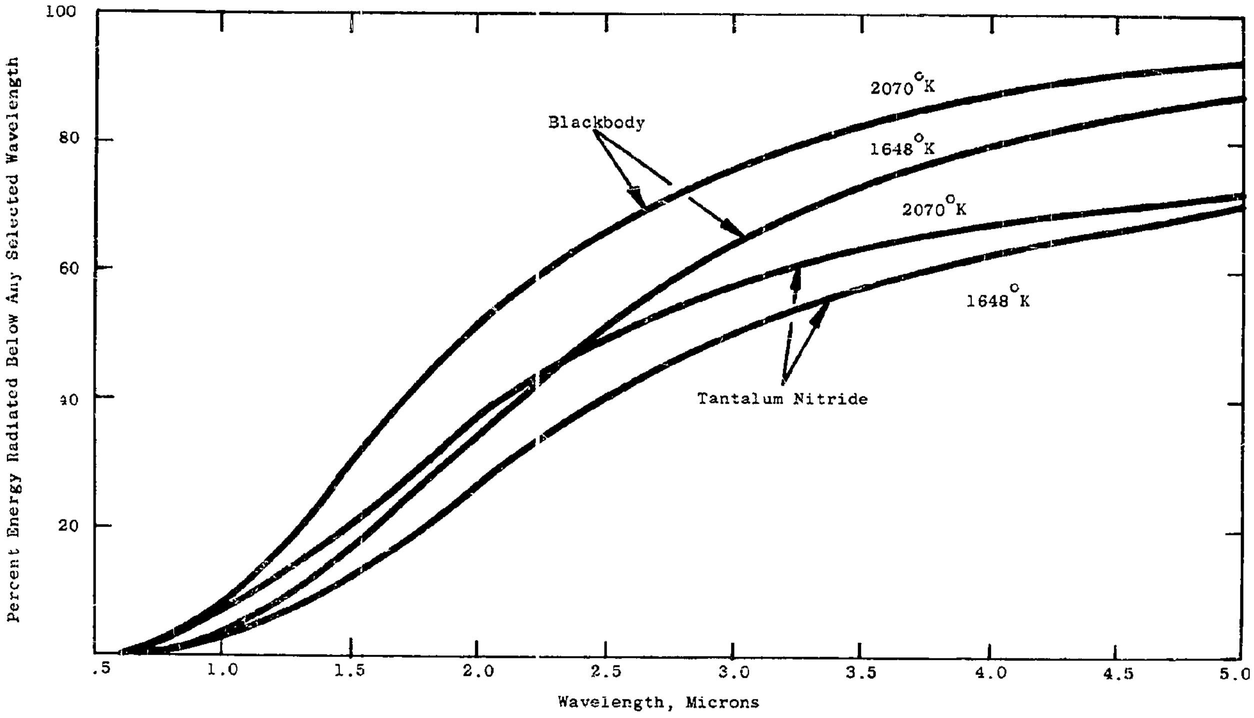

Figure 79. Relative Radiant Energy - TaN, Specimen 2

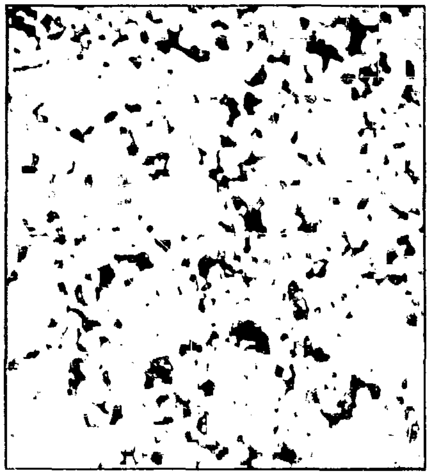

Figure 80. Polished HfN - 300X

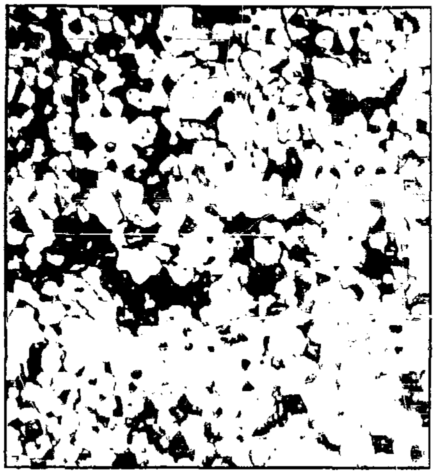

Figure 81. Etched HfN - 300X

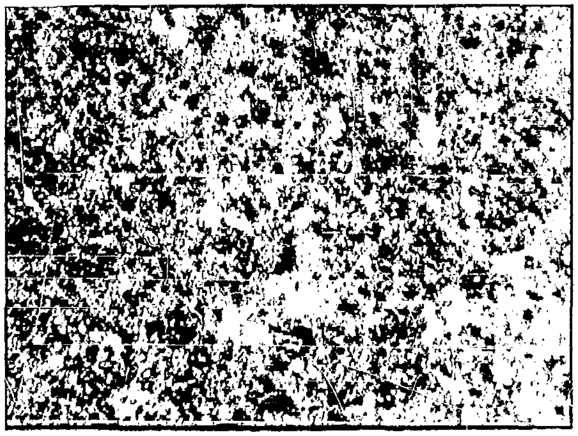

Figure 82. HfN After Heating to 2192°K - 300X

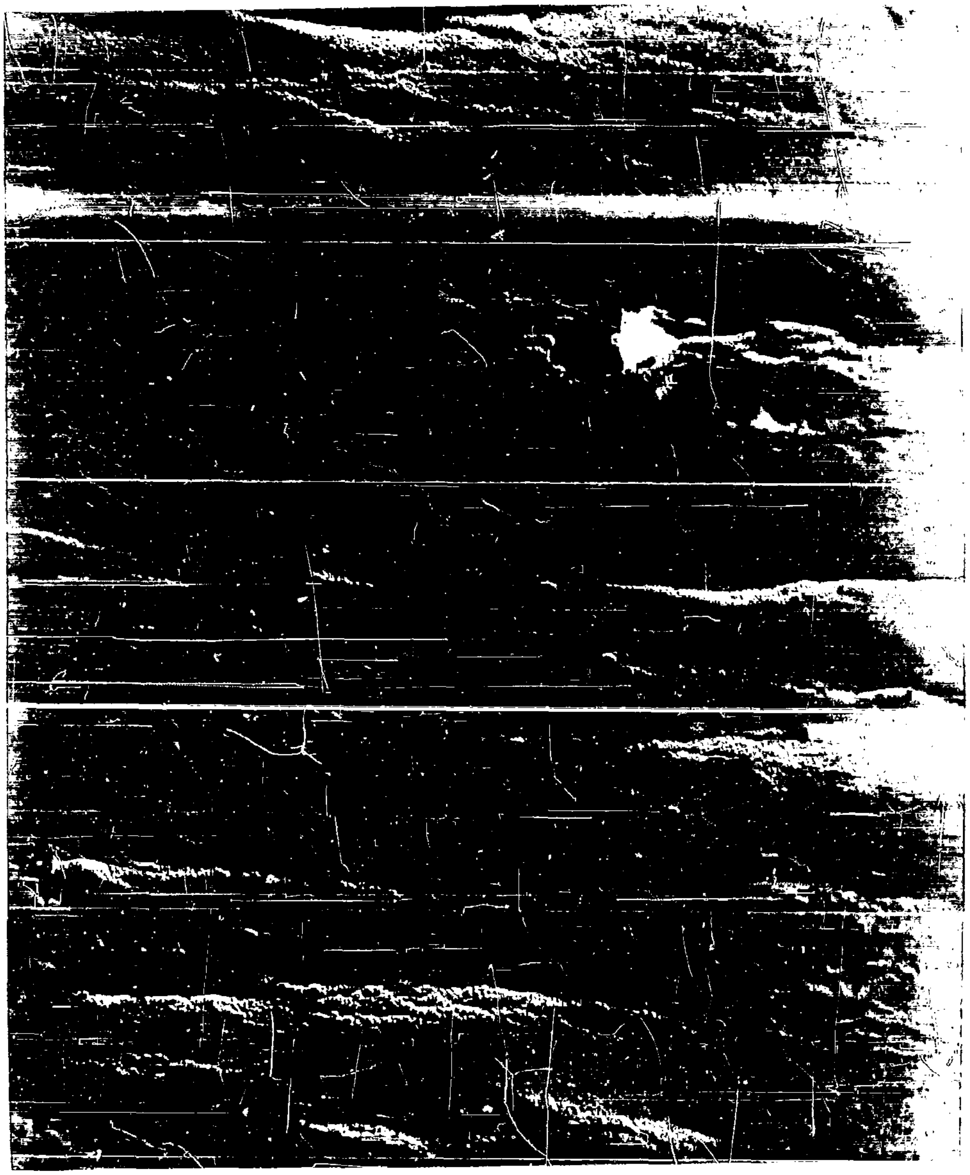

Figure 83. HfN Before Heating - 72000X

Figure 84. HfN After Heating to 2192°K - 72000X

Table 47

CHEMICAL ANALYSIS - HAFNIUM NITRIDE

Hafnium		93.22%	Antimony	ND	50 PPM
Nitrogen		6.46%	Silicon		10 PPM
Zirconium		2%-4% (Est.)	Tin	ND	10 PPM
Silver	ND	5 PPM	Strontium	ND	10 PPM
Aluminum		100 PPM	Tantalum	ND	500 PPM
Arsenic	ND	100 PPM	Tellurium	ND	100 PPM
Boron	ND	10 PPM	Thallium	ND	10 PPM
Barium	ND	10 PPM	Titanium		700 PPM
Beryllium	ND	10 PPM	Vanadium	ND	10 PPM
Bismuth	ND	10 PPM	Tungsten	ND	500 PPM
Calcium		30 PPM	Zinc	ND	50 PPM
Cadmium	ND	10 PPM	Potassium		10 PPM
Cobalt	ND	10 PPM	Indium	ND	10 PPM
Chromium		300 PPM	Lithium	ND	10 PPM
Copper	ND	10 PPM	Magnesium	ND	5 PPM
Iron		2500 PPM	Manganese	ND	5 PPM
Germanium	ND	10 PPM	Molybdenum	ND	10 PPM
Columbium	ND	100 PPM	Sodium		15 PPM
Nickel		30 PPM	Thorium	By X-ray	
Lead	ND	10 PPM			

NOTE: ND = not detected less than

PPM = parts per million

d. Weight and Density - HfN

Weight and Density measurements were run before and after heating to 2192°K. Table 49 gives results of these measurements. Carborundum Company reports a density of 12.54 gm/cc. The small gain in weight on heating supports x-ray findings of slight oxidation having taken place.

e. Normal Spectral Emissivity - HfN

Emissivity measurements were run on hafnium nitride at 1617°K, 1809°K, 2006°K and 2192°K. Figure 85 shows the wavelength dependence of emissivity out to 4 microns. The crossover point where emissivity is constant with respect to temperature occurs at about 0.47 micron. Figure 86 is a plot of normal total emissivity as a function of temperature. These data were computed from measured spectral emissivity data and are also given in Table 50. It should be noted that a trace of oxide formed

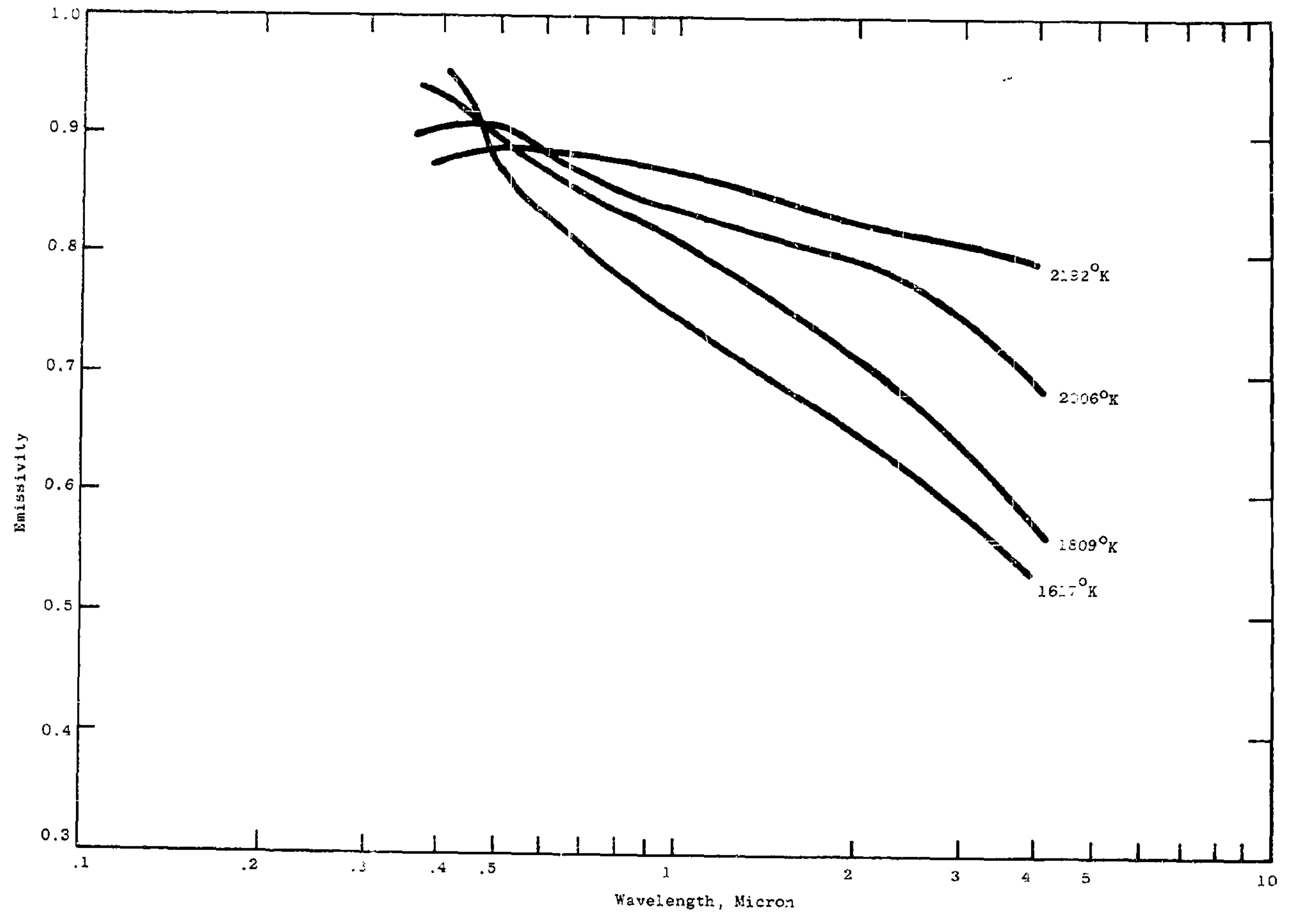

Figure 85. Normal Spectral Emissivity - HfN Specimen

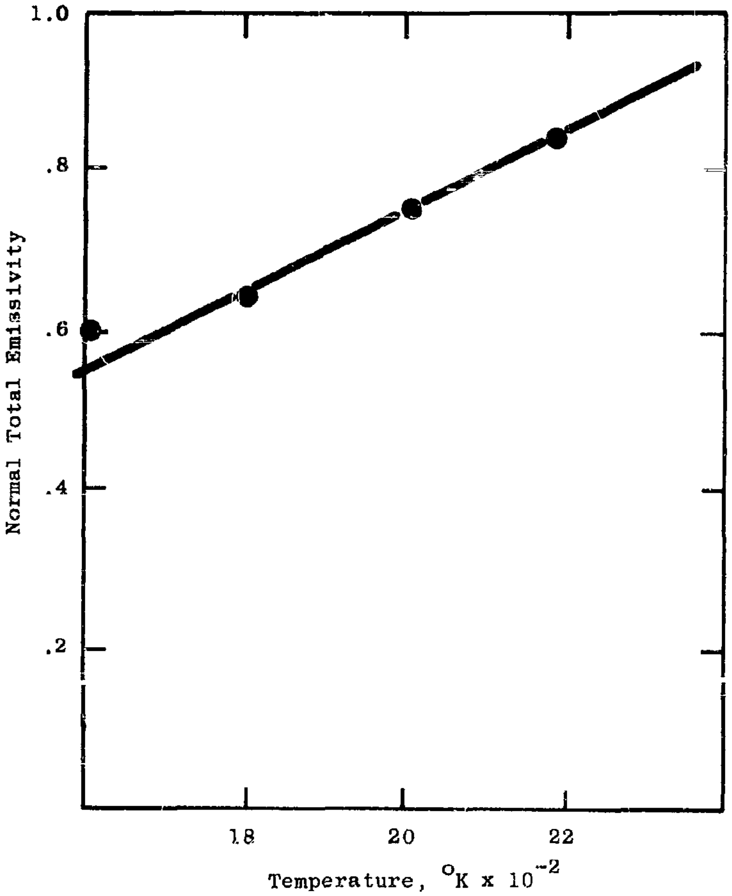

Figure 86. Normal Total Emissivity - HfN Specimen

on the surface during spectral emissivity measurements. This could cause spectral emissivity values to be slightly high beyond 1 micron wavelength. The effect on normal total emissivity values would be small due to displacement of maximum radiation toward the shorter wavelengths at the high test temperatures.

Table 48

X-RAY DIFFRACTION PATTERN - HfN SPECIMEN

I/I_o	d,A Measured	Impurity Lines	ASTM d-Values	hkl
Before Heating				
100	2.62	-	2.62	111
70	2.26	-	2.26	200
40	1.60	-	1.60	220
45	1.36	-	1.36	311
10	1.30	-	1.30	222
5	1.13	Unidentified	-	-
20	1.03	Unidentified	-	-
20	1.01	Unidentified	-	-
25	.924	Unidentified	-	-
15	.871	Unidentified	-	-
10	2.93	Thorium	2.93	111
5	2.54	Thorium	2.54	200
5	1.79	Thorium	1.79	220
After Heating*				
10	3.15	HfO_2	3.15	111
10	2.82	HfO_2	2.82	111

* In addition to the above oxide lines, those lines detected before heating were also found in the specimen after heating.

Table 49

WEIGHT AND DENSITY - HfN SPECIMEN

	Before	After	Change
Weight-gms	2.7876	2.7880	+.0014
Density-gms/cc	11.9	11.9	0

Table 50

NORMAL TOTAL EMISSIVITY - HfN SPECIMEN

Temperature °K	Total Normal Emissivity
1617	.60
1809	.64
2006	.75
2192	.85

The rate of change of normal emissivity with respect to temperature is 0.5×10^{-3} units per degree K. Figure 87 is a plot of emissivity as a function of temperature at constant wavelength. This indicates that at a wavelength of about 0.47 micron, no change in emissivity takes place with temperature. Temperature coefficient of emissivity is positive at wavelengths greater than 0.47 micron and negative at shorter wavelengths. Figure 88 is a plot of the temperature coefficient of emissivity. Figure 89 shows the total percent energy radiated by HfN below any selected wavelength at 1617°K and 2192°K relative to blackbody radiation at the same temperatures.

D. Conclusions

Spectral emittance properties of NbB_2 specimens employed in these experiments indicate it to possess fair light producing capabilities having an emissivity above 0.6 at wavelengths below 0.7 micron. Its ability to radiate heat in the infrared region is poor since emissivity is below 0.5 at wavelengths greater than 1 micron. In applications such as rocket nozzles NbB_2 would therefore attain thermal equilibrium at temperatures higher than that of materials possessing a higher emissivity at the same temperature. This coupled with relatively low thermal conductivity (about 6% that of copper) renders the application of NbB_2 selective.

Zirconium diboride appears to be less stable than NbB_2 at elevated temperatures exhibiting greater activity with traces of nitrogen, oxygen and water vapor, forming surface films that seem to act as barriers to further reaction. Its capability to radiate over the wavelength bandwidth of 0.4 μ to 5 μ, is almost twice that of NbB_2 and one half that of a blackbody.

Titanium diboride possesses a higher total thermal radiation property than the borides of niobium and zirconium. This favorable thermal property coupled with the fact that it possesses a lower density, higher thermal conductivity and is harder than niobium and zirconium diboride suggests its application at high temperature in erosive environments. Additional research on thermal properties of TiB_2 at high temperature is suggested.

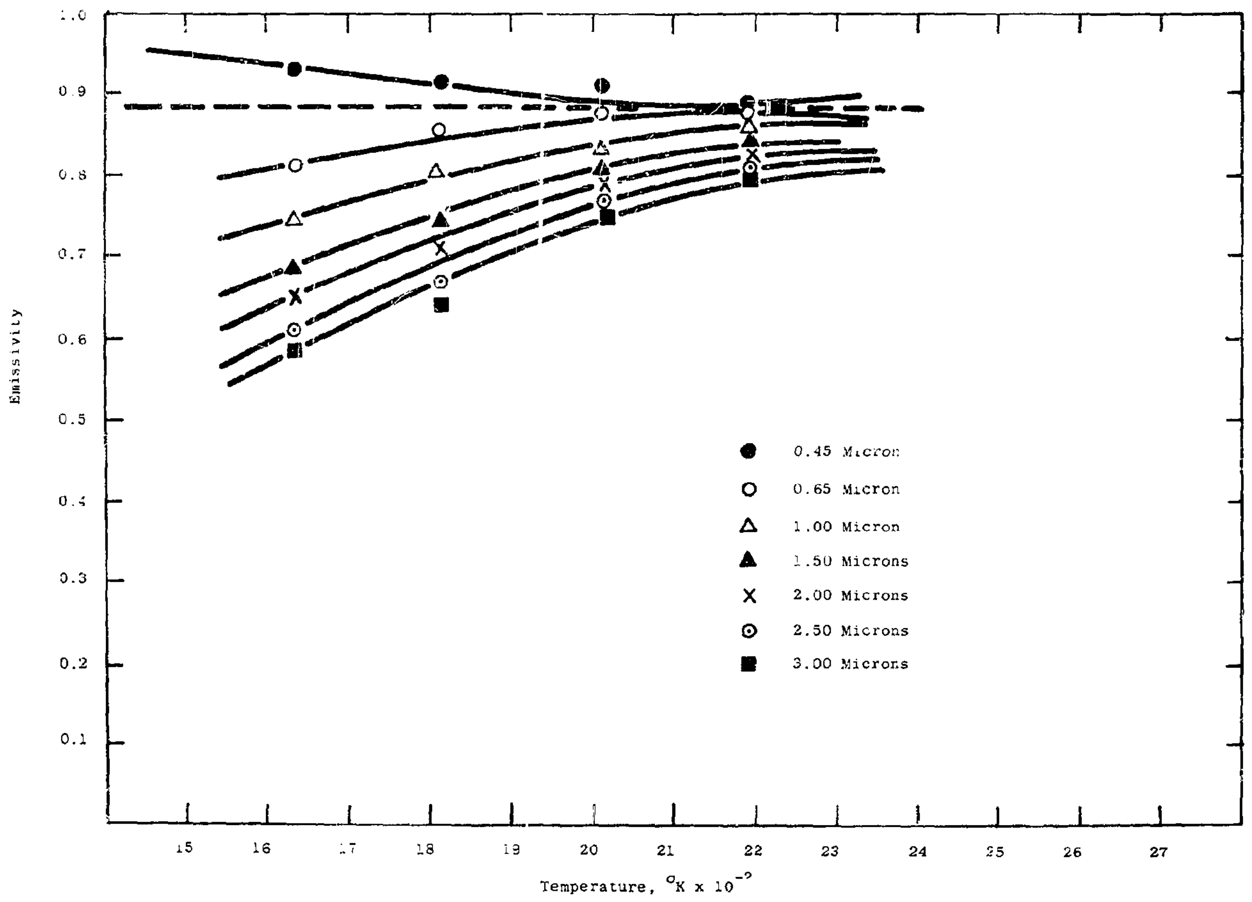

Figure 87. Temperature Dependence of Emissivity - HfN Specimen

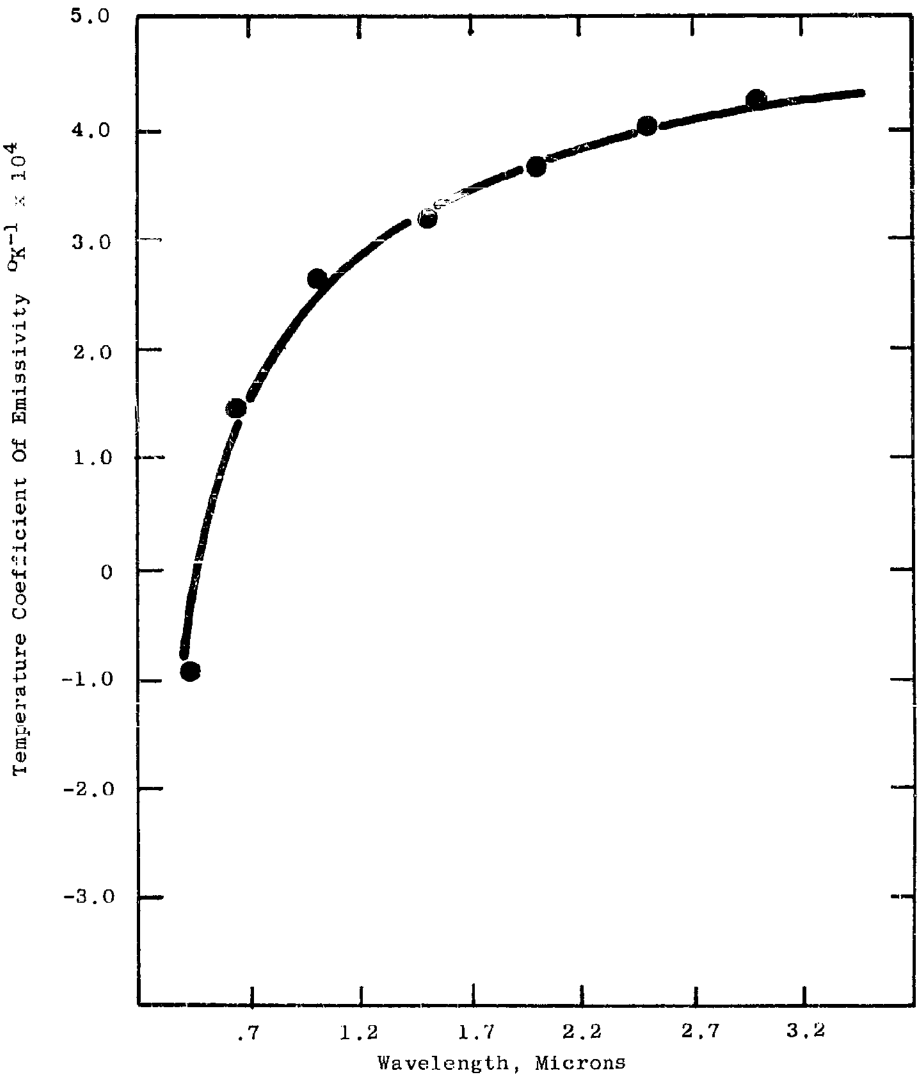

Figure 88. Temperature Coefficient of Emissivity - HfN Specimen

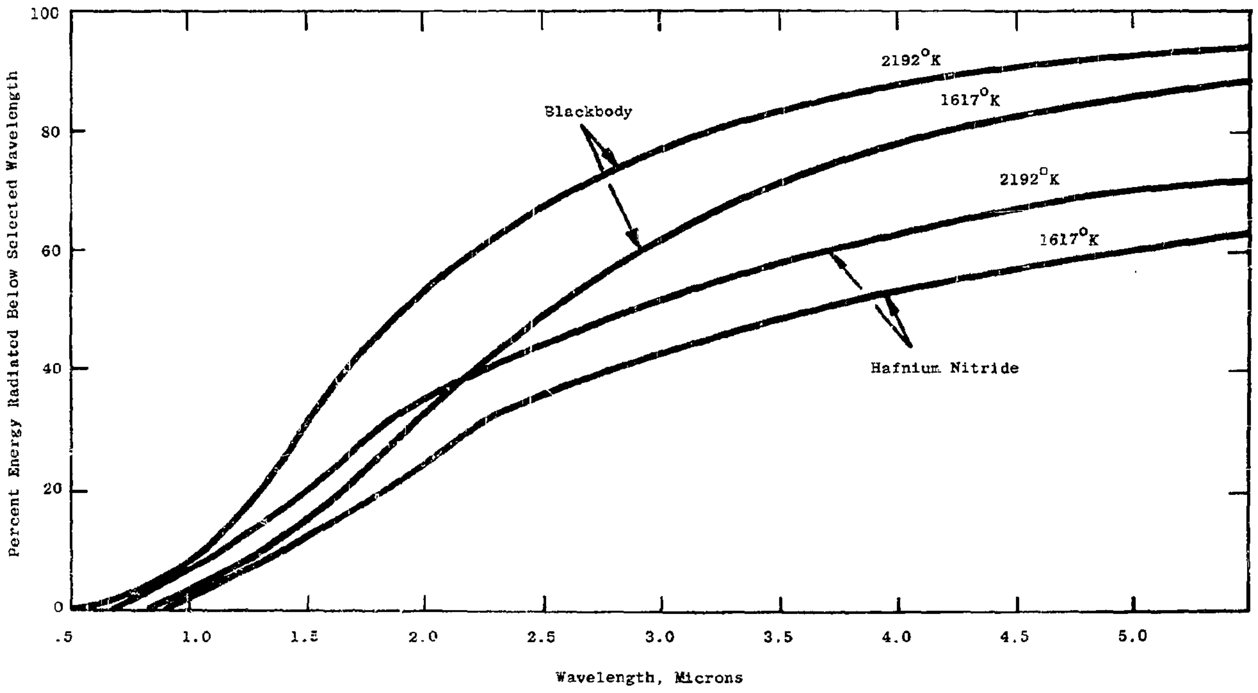

Figure 89. Relative Radiant Energy - HfN Specimen

The rate of rise of normal total emissivity of ZrN is the highest for the nitrides herein studied. It is suggested that additional measurements be made at higher temperatures in an atmosphere of nitrogen. New specimens have been obtained possessing a composition that indicates a higher purity than that reported here for the specimens studied.

Specimen composition, the dissociation of specimen 1 to tantalum and the nitriding of specimen 2 with associated disintegration of the surface into a polycrystalline powder render the values of emissivity herein reported not rigorously applicable to pure TaN. Time did not permit running determinations in an argon atmosphere. These are now under way and will be reported.

Emissivity of HfN is high in the visible indicating that at high temperature it possesses high efficiency light producing capabilities. It is also an effective thermal radiator in the infrared possessing a total emissivity greater than ZrN and TaN.

During experimental measurements of emissivity involving these highly polished specimens, it was found that surface structures continually change at a rate dependent on temperature. These changes are the result of thermal etching, evaporation, crystallization, and grain growth. These effects can be minimized by first heating the specimen for a time sufficient to stabilize surface structure at each test temperature. When test temperatures are sufficiently high to induce thermal dissociation and surface reactions with trace contaminants in the specimen chamber, coincident changes in emissivity take place. The latter can be minimized by modifying the specimen chamber to permit a controlled continuous flow of purified gas through the chamber. Thus active gases that diffuse out of the specimen and from chamber surfaces will be continually flushed out.

Results of work carried out on surface characterization suggest that a more basic study could be directed to developing knowledge relating surface attenuation of normal spectral emissivity with surface structure, at temperatures wherein structures remain unchanged. This would also provide an opportunity to more intimately relate spectral scattering with emittance and the establishment of effective absorption coefficients.

By bringing inhomogeneous effects under control it may then be possible, through relating surface composition to characteristic spectral radiance, to employ emissivity as a means of establishing thermal decomposition characteristics of refractory materials. In addition, the suggested research on surface structure would assist in developing surface design concepts leading to the control of surface emittance, absorptance, and reflectance and thus supplement dielectric film research.

E. References

1. Coffman, J.A., et al, Carbonization of Plastics and Refractory Materials Research, WADD Technical Report 60-646, Part I, (Feb. 1961).

2. Coffman, J.A., et al, Carbonization of Plastics and Refractory Materials Research, WADD Technical Report 60-646, Part II (Jan. 1963).

3. Canada, A.H., Simplified Calculation of Blackbody Radiation - General Electric Review, December 1948.

4. Worthing, A.G., Temperature Radiation Emissivities and Emittances, p. 1164 in Temperature, Its Measurement and Control in Science and Industry, New York, Reinhold, 1941.

5. Schwarzkopf, et al, Refractory Hard Metals, The MacMillan Company, 1953.

6. Glaser, J.W., Metals 4, p. 391 (1952).

7. Campbell, I.E., High Temperature Technology - John Wiley and Son, 1956.

8. Andireux, L., Review Metals 45, p. 49 (1948).

9. Chiotti, P., J. Am. Ceram Soc. 23, 123 and 334 (1952).

APPENDIX A - CURVE OF GROWTH METHOD APPLIED TO BORON

As mentioned in the text, a continuum absorption technique was used to check the vaporization of boron metal contained in a boron nitride cell. The apparatus was essentially the same as used in the resonance line absorption work with the exception of substituting a hydrogen lamp continuum for the hollow cathode source. A schematic of the apparatus is given in Figure 90. Absorption measurements were carried out at various temperatures on the boron resonance doublet, 2497.73 Å and 2496.78 Å. These lines represent transitions from the doubly degenerate ground state $^2P_{3/2,1/2}$ to the $^2S_{1/2}$ excited state. It is because of this doublet that we were able to relate the absorption to an arbitrary atom concentration and hence obtain a heat of vaporization. The atom population of the $^2P_{3/2}$ state is twice that of the $^2P_{1/2}$ state and hence the transitions, 2497.73 Å and 2496.78 Å respectively, should have an intensity ratio of 2:1. However, this is true only when the absorption is small. Nevertheless, even at high absorptions, the population ratio remains 2:1 and, therefore, an arbitrary curve of the absorption vs. concentration can be obtained. This is essentially the curve of growth method. The so-called total absorption of a continuum by an atomic line is defined as*:

$$A_G = \frac{2\,\pi \times \text{area under absorption curve}}{I_o} \qquad (32)$$

I_o : incident intensity.

Table 51 gives values of A_G for the 2497.73 Å and the 2496.78 Å resonance transitions of boron, respectively, as a function of temperature.

Table 51

CONTINUUM ABSORPTION OF BORON DOUBLET

Run #	Temperature °K	A_G 2497.73	A'_G 2496.78
1	2105	.094	.051
2	2117	.122	.065
3	2151	.145	.092
4	2181	.193	.123
5	2197	.219	.168

It is to be noted that the ratio A_G:A'_G deviates more and more from 2:1 as the temperature and hence the atomic concentration increases. The total absorption, A_G, is given by *:

---

* Mitchell and Zemansky, "Resonance Radiation & Excited Atoms", Cambridge Press (1934).

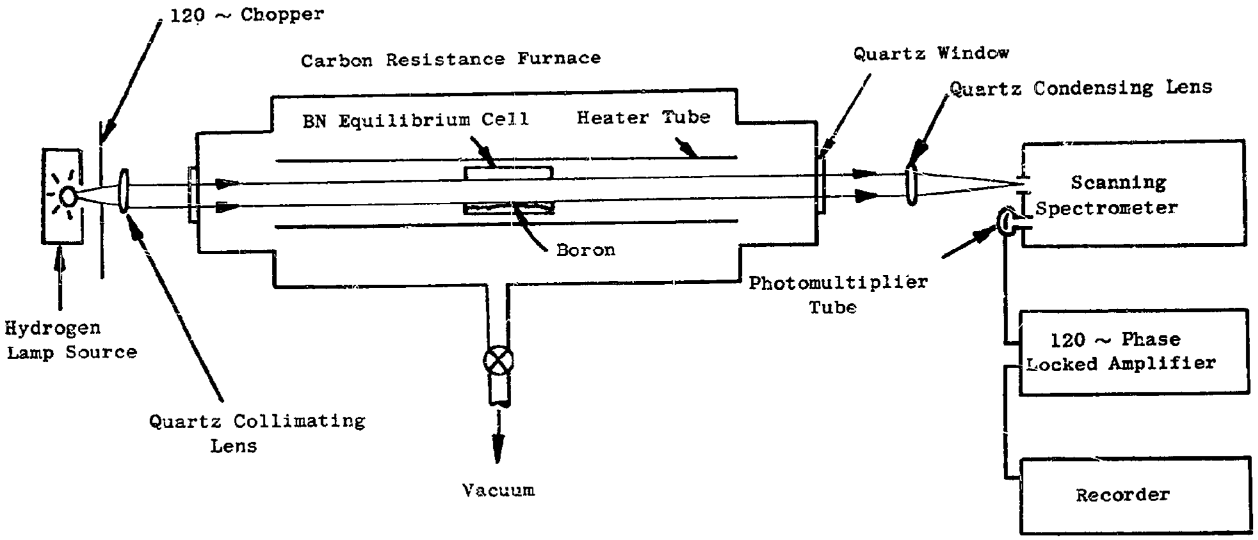

Figure 90. Schematic of Boron Continuum Study Apparatus

$$A_G = 2\pi \int_0^\infty (1 - e^{-K_\nu X})\, d\nu \qquad (33)$$

where:

K_ν = absorption coefficient at various frequencies, ν

X = length of absorbing path.

When the number of absorbers is small and hence $K_\nu X \ll 1$, equation (33) becomes:

$$A_G = 2\pi \int_0^\infty (1 - 1 + K_\nu X)\, d\nu \qquad (34)$$

$$= 2\pi \int_0^\infty K_\nu X \quad d\nu$$

However,

$$\int K\, \nu X = \frac{\pi e^2}{mc} \quad Nf \qquad (35)$$

where:

$\frac{\pi e^2}{mc}$ = are constants and

N = number of absorbers/cc.

f = oscillator strength.

Therefore, at small concentrations, the absorption A_G should be linear with atom concentration. The curve of growth shown in Figure 91 was traced out in the following fashion. From Table 51, run #1 is seen to have the ratio, A_G:A'_G close to 2:1 and, therefore, lies in the linear absorption region. On a log-log plot, the value of A_G, .094, is plotted against the arbitrary concentration value (Nf) = 4.0 (this value must be arbitrary since the oscillator strength f is not known for these transitions) and since the corresponding A'_G = .051 must be related to an Nf value half that of the A_G, namely 2.0, two points are obtained on the plot. A straight line is then drawn through these two points since they are in the linear region of absorption and the initial part of the curve is defined. Going on to run #2, it is seen that the A'_G = .065 lies on the initial straight line and an Nf value for this point is read off the curve. Since the Nf value for the corresponding A_G point must again be twice this value, the A_G point can be plotted and the curve extended. In this fashion, the curve of growth is traced out point by point. It is seen from Figure 91 that, at high absorptions, the curve begins to bend over and indeed this is quite typical of this method. The curve in Figure 91, therefore, relates the absorption to an arbitrary concentration; and since each point is at a known temperature, an arbitrary pressure of boron can be obtained as a function of temperature. The logarithm of the arbitrary pressure, log (TNf), was least squared against the corresponding 1/T values and the heat of vaporization of boron obtained. This value was:

$$\Delta H_{vap.} = 133 \text{ kcal/mole}$$

This is in excellent agreement with the literature value. It now also becomes possible, with the aid of this curve of growth, to apply continuum absorption techniques to obtain boron pressures in the diboride systems. This will be done in the forthcoming year.

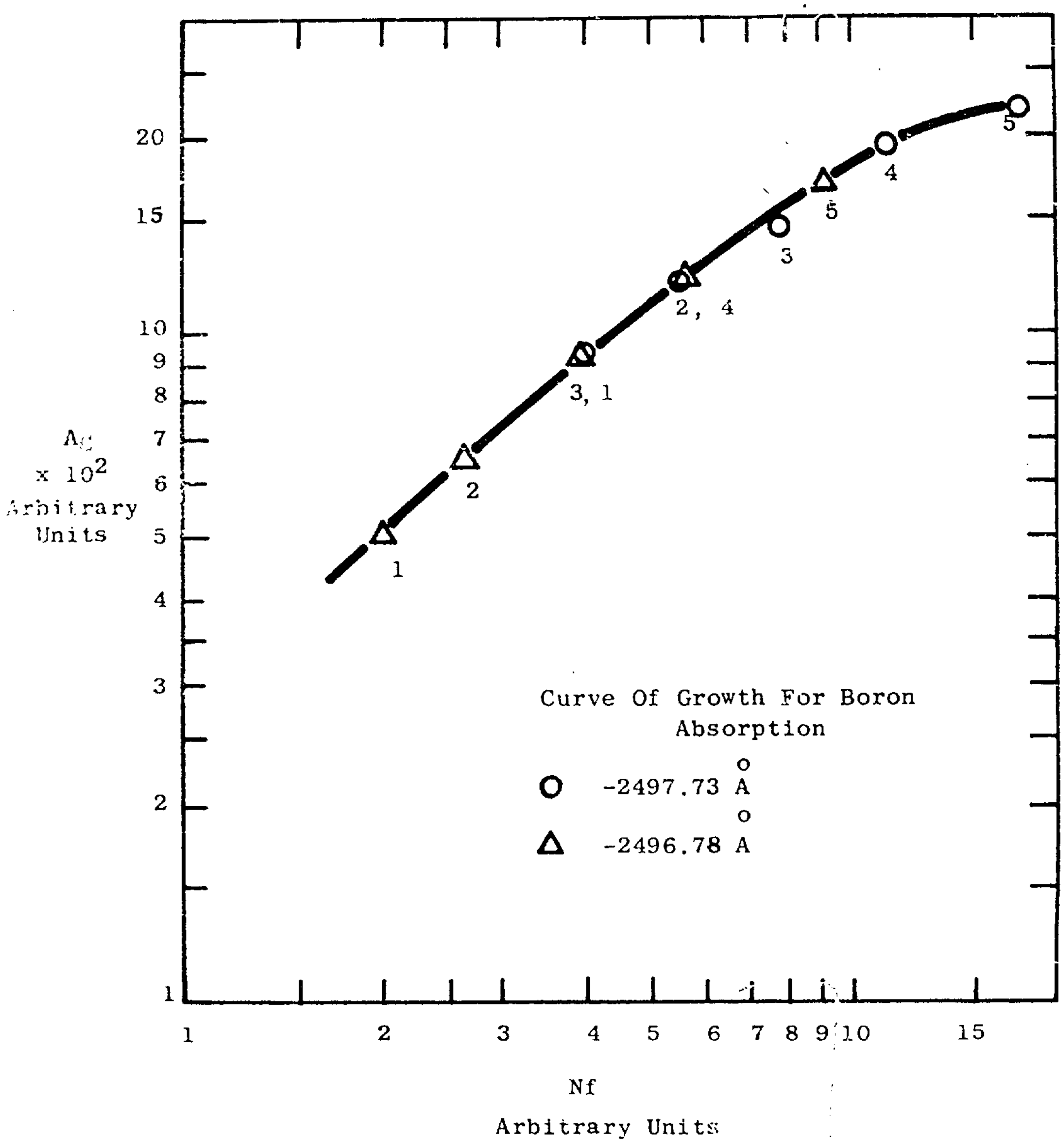

Figure 91. Curve of Growth for Boron Absorption